Continuum and Molecular Dynamics Simulations of the Growth of a Vapor Bubble on a Heating Surface: Exploring the Mechanism of Nucleate Boiling Heat Transfer

by

JINYONG BAO

A dissertation submitted to the Graduate Faculty in Engineering in partial fulfillment of the requirements for the degree of Doctor of Philosophy, The City University of New York

2011

The manuscript has been read and accepted for the Graduate Faculty in Engineering in satisfaction of the dissertation requirement for the degree of Doctor of Philosophy.

Professor David Rumschitzki

_____	_____
Date	Chair of Examing Committee

Professor Mumtaz Kassir

_____	_____
Date	Executive Officer

Prof. David Rumschitzki

Prof. Joel Koplik

Prof. Jeff Morris

Prof. Charles Maldarelli

Prof. Taehun Lee
Supervisory Committee

The City University of New York

ABSTRACT

Continuum and Molecular Dynamics Simulations of the Growth of a Vapor Bubble on a Heating Surface: Exploring the Mechanism of Nucleate Boiling Heat Transfer

By

Jinyong Bao

Adviser: Professor David Rumschitzki

Starting with a completely rewritten code for the conductively-driven quasi-static vapor bubble growth in an axisymmetric, cylindrical cell comprised of solid and liquid phase of finite thicknesses under small Reynolds, Peclet, Capillary and Bond numbers to verify L. Huang's (our prior Ph.D. student) earlier results, we couple the solution of the quasi-static problem with three simple, somewhat *ad hoc* models of contact line motion and relax the assumption of small Bond number to simulate the growth of an incipient bubble until gravity begins to slowly deform the vapor bubble and then to detach it from the solid heater surface. A simple physical theory is developed to explain that when the bubble density is not too high, the bubble volume vs time approaches a 3/2 power before gravity begins to deform its shape, independent of contact line motion models and system parameters such as the conductivity ratio of the liquid to solid and degree of wall superheat.

On the other hand, contact line motion does have a significant effect on bubble deformation and detachment. Molecular dynamics (MD) is employed to determine the contact line motion in a nano-scale version of our three-phase system because MD not only includes heat transfer, but also fluid flow, which can remove many restrictions of the earlier continuum calculation in our nano-size system. Instead of nucleating a bubble by

cavitation, we nucleate a vapor bubble by heating the bottom of the solid upon which the fluid sits at constant pressure. Under a uniform body force that, due to the scale of MD is far larger than terrestrial gravity, we then track the bubble's growth driven by heat transfer from the conducting heated solid until detachment. Its contact line motion is monitored and the effects of wettability of solid surface, temperature-slip of fluid-solid interface and the choice of the interaction between the solid and the fluid have also been discussed. Unfortunately, this temperature slip mitigates some of the effects of the contact line that the continuum modeling (without temperature slip) finds so crucial at macroscopic scales.

Acknowledgment

I would like to express my deepest appreciation to my advisor, Professor David Rumschitzki. It was a pleasant and challenging time working with him on this project. I have benefited a lot from his valuable critiques and rigorous research attitude. Without his continuous guidance and persistent help this research would not make such huge progress. I am also grateful to Professor Joel Koplik, who is a well-recognized expert in molecular dynamics, for guiding me in implementing this technique in this research. I would also like to thank Professor Jeff Morris, Professor Charles Maldarelli and Professor Taehun Lee for their valuable suggestions.

Words alone cannot convey my gratitude to my wife, Ying Rong, and my parents-in-law, Xinya Rong and Junzhen Sun for their selfless support throughout my life. This dissertation is dedicated to my dear parents, Shilai Bao and FengRong Li, who motivated me to achieve the best of me and who, sadly, both passed away in 2007; this dissertation is also dedicated to my 4-year-old daughter, Rebecca, and 2-month-old son, Bryan, who give me inner peace throughout any hardship and make me realize the importance of love and responsibility.

Finally, I am thankful to this project itself, which has led me to acquire significant knowledge in mathematics, physics and computer languages and to gain extensive experience in numerical solutions of partial differential equations and in molecular dynamics simulations.

This research was funded by grant (NNX09AK40G) from NASA

TABLE OF CONTENTS

LIST of TABLES

LIST of FIGURES

Chapter I

Introduction and Literature Review

I.1 Literature Review

It has been long known that boiling cools a hot surface very efficiently. Figure I.1 shows the standard boiling curve[1-3], a plot of the heat flux from a heating solid to a liquid versus the logarithm of the wall's superheating above the liquid's saturation temperature, T_{sat}. It grows very slowly for low wall superheat ($(T_w - T_{sat}) \leq 4°C$) and natural convection removes the hotter fluid from the metal surface, allowing cooler fluid to replace it. When superheat reaches 4°C, vapor bubbles begin to form in cavities or scratches on the heating surface, grow by the evaporation of liquid into them, and, under gravity, detach and rise through the liquid. When the wall superheat is 9°C~30°C, these bubbles interact each other to form continuous jets and columns of vapor. The single bubble sub-region and jets and columns sub-region comprise the nucleate boiling regime. In this regime, the curve becomes much steeper, growing, e.g., for water, by 1-2 orders of magnitude over ~20°C wall superheat. Beyond 30°C wall superheat, heat flux drops dramatically because vapor can temporarily dry out the hot surface. At even higher superheat, radiation heat transfer dominates and heat flux rises sharply with increasing temperature. Clearly, the nucleate boiling regime has the potential for stable, enormously efficient heat transfer at a relatively low thermal driving force[4], therefore it is the ideal for any applications that requires large heat transfer from a hot solid, such as in nuclear reactors cooling[5,6], the cooling of electronic chips[7], etc. As efficient uses of energy are required, as new technologies are employed at micro scales and as different challenging environments (such as in space or in low gravity[8]) are explored, a correct fundamental understanding of nucleate boiling heat enhancement becomes ever more crucial.

To focus on understanding in a fundamental way the processes of nucleation and growth at, and deform until departure of a vapor bubble from the heated surface, this research aims to advance the understanding of mechanism of nucleate pool boiling heat transfer which is the simplest mode of boiling but poorly understood.

Much early work focused on the practical problem of correlating[9-12] heat flux to system parameters i.e. the thermal driving force, surface properties, fluid thermodynamic properties and the density of nucleation sites. The most famous one is the power law

correlation between the heat flux and nucleation site density shown in Fig I.2[13], which yields a power of 1/3-1 for pool boiling. The consensus since the 1960s attributes nucleate boiling's heat enhancement to two mechanisms[12,14,15] shown on Fig I.3: 1) Convection theory: The departing bubble acts like a small heat pump carrying part of the superheated liquid into the bulk fluid, at the same time, cold fluid from above to convect to the heating surface. It is only the sensible heat transfer that involves in bubble-induced liquid convection; 2) Micro-layer theory: There is a thin (~micron thick) wetting layer that exists under all or portion of vapor bubble[16,17]. The growth of vapor bubble is due to evaporate this microlayer, and the heat can also travel at the top of vapor bubble. Clearly, in this theory the latent heat is involved.

Moore & Mesler[18]embedded small (.05 mm^2) thermocouples in the heater surface and measures sharp temperature drops of 20-30 ^oC in 2ms upon arrival of the vapor-liquid interface at the thermocouple's position. Some measurements[19-21] estimated the thickness of micro-layer as 200nm—5μ until Koffman & Plesset's[22] preferred 2μ by his careful analysis of the experimental details. Cooper & Lloyd [20]not only confirmed the existence of a micro-layer underneath isolated bubbles formed on glass or ceramic surfaces but also deduced the thickness of the micro-layer from the observed response of the heater surface thermocouple. Based on Cooper & Lloyd's wedge-shaped profiles, Olander & Watts[23] developed an analytic, boundary layer type theory to explain micro-layer evaporation. Wilson et al[24] used lubrication theory to extend Landau and Levichs[25] and Bretherton's[26] classic works to find shapes of long-2D vapor bubbles sandwiched between thin liquid films on parallel plates. Mitrovic[27] used their results to derive an the evolution of the wedge's interface. Mei et al[28,29] assumed almost all the heat transfer to the wedge-shaped micro-layer and solved the heat equation in both micro-layer and solid heater. Assuming uniform, time-independent solid-fluid temperature, Lee & Nydhal[30] numerically solved the momentum and energy equations from bubble inception to departure in a liquid at T_{sat}. They estimated that microlayer evaporation contributes 87% of nucleate boiling's heat enhancement for water (1 atm, 8.5K wall superheat), as opposed to 10-50% found by Plesset & coworkers[22,31], 40 % by Dhir[12] and 20% by Son et al[32,33]. Koffman & Plesset[22] pointed these calculations are very sensitive to the assumed initial micro-layer thickness.

Scriven[34] found a similarity solution for a growing vapor bubble in an infinite liquid initially at a uniform temperature above the fluid's saturation temperature. Cooper & Lloyd[20] discuss a computer model for the heat flow in both the solid and the fluid for a given initial micro-layer thickness, that calculated how the surface temperature profile changed with micro-layer evaporation. Some numerical solutions of the momentum and energy equations with phase change[35-37]focus on film boiling where the heating surface remains dry. Most of numerical work also assume a uniform, constant metal surface temperature[32,38,39], contrary to the experimental studies such as Moore & Mesler[18] (mentioned above). Kenning and coworkers[40,41] used thermo-graphic liquid crystals on very thin heating plates to visualize the temperature distribution along the heating surface and they indeed illustrated a highly non-uniform temperature does exist on the heating surface, with jumps of ~30^{o}C over a couple of millimeters. Recently, Kim's group[42-44] used a micro-heater array consisting of 96 independently controlled heaters to measure the heat transfer distribution for isolated bubbles under the constant temperature. They observed that the heat transfer on the center heaters is higher when they are rewetting by the bulk liquid and the heat transfer spikes as bubble departure, then decays with time. In addition, they calculated the ratio of the physical diameter of the bubble calculated from the high-speed images assuming the embryo shape was a truncated sphere to the diameter of a sphere of equivalent volume assuming that all the heat transferred from the selected region goes into latent heat, which is a measurement of heat transferred from the wall. They[45] found that this ratio is close to 1 for slowly growing bubbles, which indicates their growth is strongly dependent on the solid wall. Compared to the amount of heat transfer to bubble from the superheated liquid, the amount of heat transfer from the solid wall is significant. Therefore, micro-layer or 3-phase contact line is the most important region to absorb this heat from the solid wall.

Sadhal[46] was the first one to treat the contact line explicitly for solving the quasi-static heat conduction equation for an attached bubble as well as a suspended bubble in semi-infinite, 3-dimensional liquid and solid phases. His temperature-profile calculations suggested that when contact line appears, the temperature at the solid and liquid is highly non-isothermal. Stephan's group[47,48] constructed a new model in which heat could be transferred through the micro-region (including the three-phase contact line) and the

macro-region (the liquid adjacent to the micro-region and the wall) of a growing bubble. Capillary pressure and curvature effects were included in the micro-region model. Results were obtained for boiling of R-114 on a copper plate. For a single bubble of radius 0.125 mm and wall superheat of 3.5 K, the extent of the micro-region was found to be less than 1 μm, but accounted for about 38% of the total heat transfer. A peak heat flux was observed within the micro-region. However, when the superheat was increased to 4.2 K, about 60% of the heat passed through the micro-region. They argued that, "in this region, micro-scale effects such as adhesion forces and interfacial thermal resistance, in combination with a strong curvature at the top of the micro-layer where there is a change of the phase, significantly influence local heat and mass transfer". Nikolayev's group[49,50] explicitly recognizes the singularity of heat flux at CL by solving unsteady 2D heat conduction of bubble growth on a planar surface between a semi-infinite liquid and solid. They focused on showing high heat fluxes yield vapor recoil that can be the origin of the boiling crisis, but not on nucleate boiling bubble growth and detachment. L. Huang, a prior student in our group, numerically solved[51]quasi-static heat conduction equation for suspended and attached bubble in the solid and the liquid regions, both with finite thicknesses. His results suggested that the existence of the contact line is critical for huge heat enhancement in the nucleate boiling.

Molecular Dynamics

Molecular dynamics (MD) is a computer simulation where the time evolution of a set of interacting atoms or molecules is followed by integrating their equations of motion. It has become a powerful tool to investigate the physics of poorly understood, complex macro or meso scale systems by simulating the detailed interactions of a large number of individual particles. In recent years, Molecular dynamics (MD) has been widely applied to the moving contact line problem in flows[52,53], contact angle hysteresis[54]; and dewetting[55]. For boiling research employing MD, although some studies[56-59] have focused on thin liquid film evaporation from the heated surface, none have emphasized the nucleation and growth of a single vapor bubble. Other studies[60-62]have focused on heterogeneous nucleation of a liquid droplet on a solid surface by cavitation at an underpressure: Maruyama and Kimura[63] studied bubble nucleation on solid surface in a system with a fixed number of particles sandwiched between parallel solid surfaces. They

then expanded the system by displacing the top wall (which lowers the system pressure) until a bubble nucleated on the bottom solid surface. They then calculated the equilibrium shape of vapor bubble, but did not focus on the non-equilibrium vapor bubble growth. Since we are interested in understanding the mechanism of nucleate pool boiling, we are far more interested in the nucleation of a vapor bubble by heating, rather than by creating an underpressure. We would then like to in follow the growth process of the bubble, driven by heat transfer from the heating solid, until gravity begins to deform the bubble and eventually causes it to detach from the heating surface. Thus we study not only the heterogeneous birth of vapor nucleus and its achievement of stability, but also its subsequent growth, deformation and detachment.

I.2 Goal of This Dissertation

Since the pioneering investigations by Jakob and Rohsenhow, research on pool nucleate boiling has undergone a metamorphosis from purely empirical approaches to physics-based modeling and experimentation of this phenomenon. However, V.K. Dhir[15], a leader in the field, states: "After more than three decades of research, we still do not have an effective, consistent model for bubble growth on a heated surface that appropriately includes the micro-layer contribution and time-varying temperature and flow filed around the bubble." Kenning also noted "this disappointing state of affairs may indicate that some fundamental characteristic of the process has been neglected." Given the experiments that indicate that a large amount of heat transfers to very tiny region at the vapor bubble base and the fact that a three-phase-CL represents a singularity in the equations of both heat transfer and fluid mechanics, we argue that the exist and the motion of three-phase-CL is the key issue of heat enhancement in nucleate boiling. L. Huang[51], an prior student in our group, used a boundary integral technique to solve for the quasistatic temperature field, and thus the heat transfer from a solid of finite thickness that is heated from below to a vapor bubble that is a section of a sphere and that on its surface in a liquid layer also of finite thickness. In this work, they treat the three phase contact line explicitly. He then couple this quasistatic heat flux to the liquid phase change to vapor and calculate the resulting quasistatic bubble growth with time. His calculation focused on a single bubble in a cell containing solid, liquid and vapor bubble, although he considered the effects of bubble-bubble interactions and of bubble density by applying

periodic boundary conditions at the transverse boundaries of his cell. His calculations focused on the situation characterized by small Reynolds, Peclect, Capillary and Bond numbers and revealed that the existence of the CL is critical for huge heat enhancement in the nucleate boiling. The next steps in carrying Huang's work forward are to 1. Consider the deformation of the vapor bubble in question under the influence of gravity for very slow bubble growth. In this way, convective effects on bubble shape and on heat transfer can still be considered small. One can then consider how the vapor bubble deforms and detaches under these conditions and examine the effect of different models of CL motion on these processes. 2. Since the motion of a CL, even in the absence of evaporation, is not well understood, it would be very useful to use MD to investigate this phenomenon. One could then use the resulting empirical CL motion with bubble growth as an input into the above continuum model in order to again examine bubble deformation and detachment, including the calculation of detached bubble sizes as a function of system parameters, e.g., heating rate. One can follow the same program for experimental measurements of CL motion. 3. In principle MD not only includes heat transfer, but also fluid flow. As such, one can use it to remove many of the restrictions of the earlier continuum calculation, at the cos of working in a nano-scale version of our system where, among other things, true gravity is utterly negligible. That is, one can use MD simulation to physically nucleate a stable vapor bubble and trace its subsequent growth in order to advance the physical understanding of this key issue in nucleate boiling. These three goals are the main focuses of this research.

I.3 Organization of This Dissertation

The dissertation is divided into 4 chapters

In chapter 1, the literatures about nucleate pool boiling heat transfer enhancement are reviewed. The appearance and motion of contact line is suggested to explain this heat enhancement. The goals of this research are also proposed.

In chapter 2, we follow L.Huang's theoretical analysis to model the heat transport by solving the quasi-steady heat conduction equation in finite liquid and solid phase under small Reynolds, Peclet, Capillary and Bond numbers with a completely rewritten code to verify his results. Boundary integral equation method with a special treatment on singularity of CL that L.Huang developed in his work is also reviewed. Our calculations

well explain dramatic heat enhancement with the appearance of vapor bubble at superheat of ~4°C for water.

In chapter 3, we simulate the growth of an incipient bubble with different inputs of CL motion (three ad hoc models of CL motion and one experimental data of CL motion) under those assumptions above. A simple physical theory is proposed to explain our finding that when the bubble density it not too high, i.e. the radius of cell is greater than 1.5 times of the radius of bubble, the bubble radius vs time approaches to the 1/2 power independent of CL motion and system parameters. Furthermore, we relax small bond number assumption (other assumption is still valid) to study the process of vapor bubble detachment. Different CL motions lead to different detachment behaviors are found.

In chapter 4, we employ molecular dynamics simulation to examine important but poorly understood physics of contact line motion. We nucleate a vapor bubble and keep it growth by heating the bottom of the solid wall. Furthermore, we study the effect of wettability of solid surface, temperature slip on solid-liquid interface on bubble nucleation and growth. Body force is applied in this nano-size system to simulate bubble lift-off process. The time evolution of CL is obtained.

Figure I.1 Standard boiling curve of water

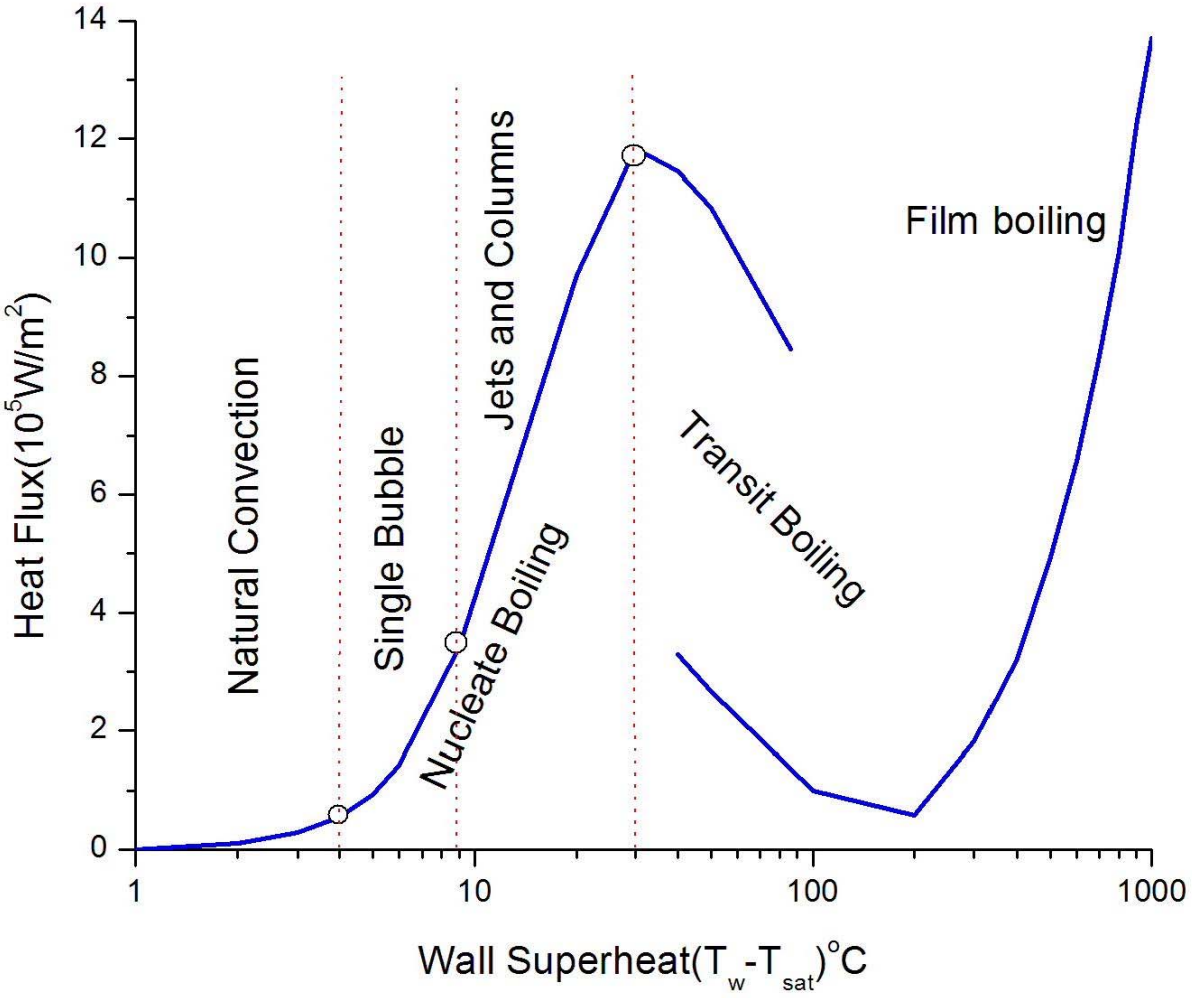

Figure I.2 Power law correlation between heat flux and bubble density

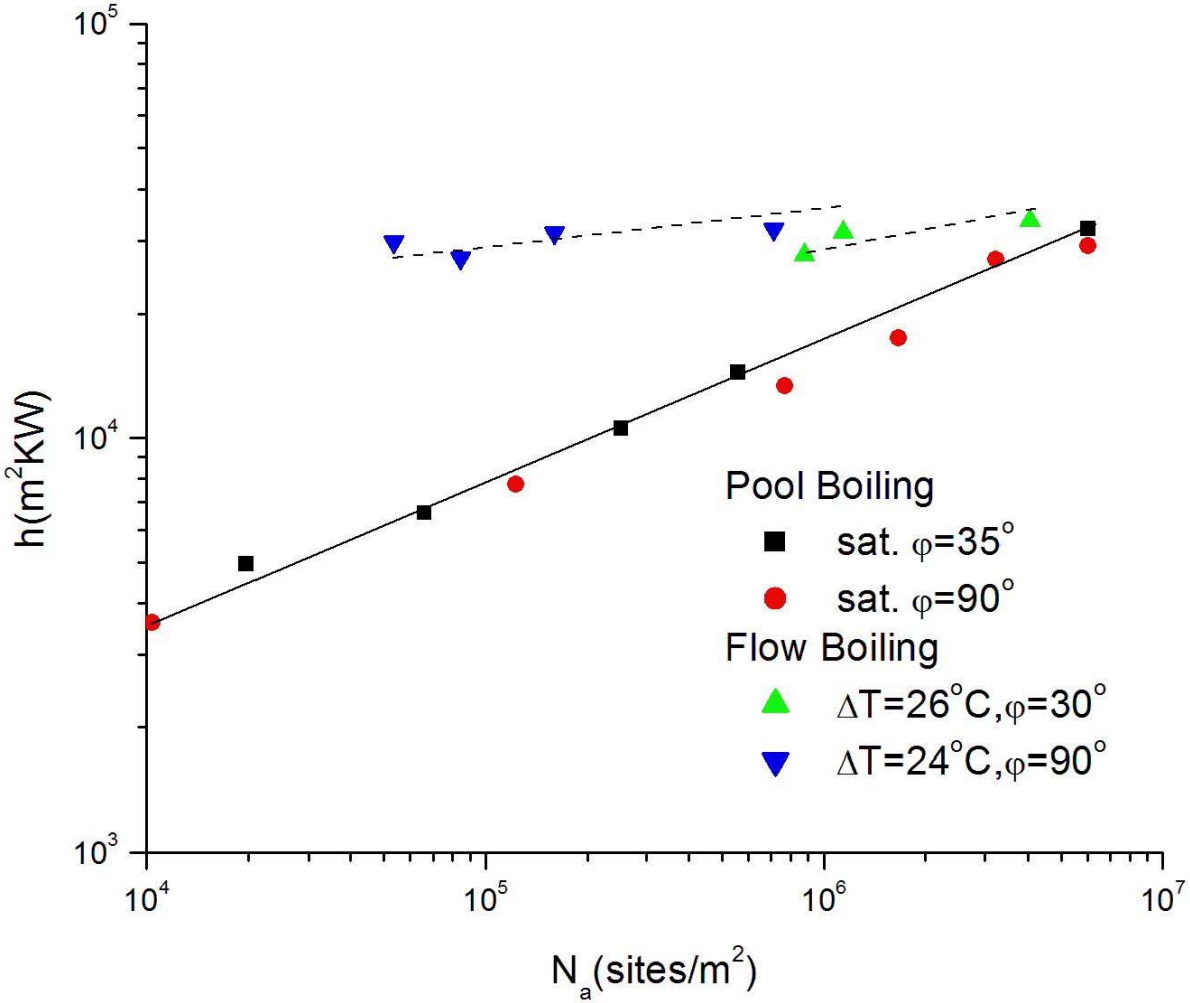

Figure I.3 Currently accepted mechanisms

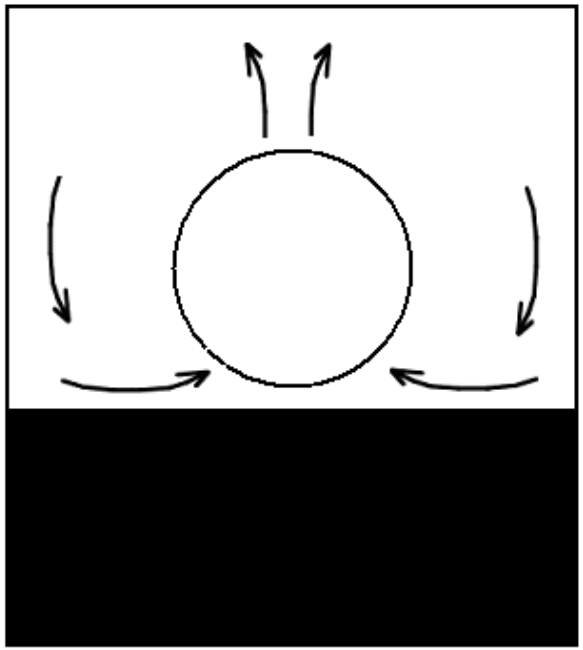

Sensible heat transfer

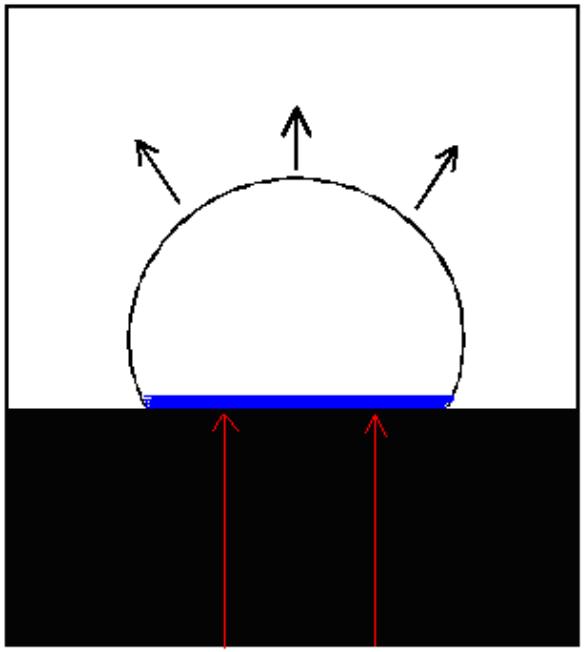

Micro-layer Model (latent heat involved)

Chapter II

General Formulation of Continuum Model and Preliminary Results

In contrast with transition or flow boiling heat transfer, our continuum model approach will mainly focus on nucleate pool boiling because its scalings allow an approximate decoupling of the heat transfer from the hydrodynamics. Our formulation and initial discussion follow L.Huang's[51] treatment that focus on the initial growth of an existing incipient vapor bubble. That analysis does not proceed beyond the stage where the vapor bubble is either a sphere near the solid surface or a section of a sphere on the solid surface. That is, it is restricted to Bond numbers much less than one, i.e., situations where gravity is negligible compared with surface tension forces. We begin with a completely rewritten code for L.Huang's theoretical analysis[51] that first confirms his results and then allows their extension to the situation where gravity begins to slowly deform the vapor bubble and then detach it from the solid heater surface. These latter stages allow for irregular, i.e., non-spherical, axisymmetric bubble geometries.

II.1 Scalings and Assumptions

In general, bubble growth has four characteristic time scales[51]:

1. $t_d \cong a'^2/\alpha_\ell$: the time over which a liquid of thermal diffusivity α_l conducts heat over distances characteristic of the bubble radius a';
2. $t_\nu \cong a'^2/\nu_l$: the time over which the kinematic viscosity ν_l diffuses vorticity over a distance a', which characterizes viscous fluid motions;
3. $t_s \cong \left(a'\rho_l \nu_l\right)/\sigma$: the time for motion a distance of a' at the capillary velocity, where surface tension acts on the interfacial shape against viscosity;
4. $t_g \cong a'/\dot{a}'$: the time a bubble needs to grow a distance equivalent to its radius, where $\dot{a}'$ represents the time rate change of the bubble radius.

For L. Huang's model approach to explore the mechanism of nucleate pool boiling, which is our initial model, we describe the system over time scales of the order t_d, for a situation where $t_g >> t_\nu$, $t_g >> t_d$ $t_g >> t_s$. One can reframe these inequalities in terms of nondimensional groups as follows:

1. Reynolds number $\mathrm{Re} := a'\dot{a}'/\nu_\ell << 1$.

2. Peclet number $\mathrm{Pe} := a'\dot{a}'/\alpha_\ell$ <<1. This states that convection is insignificant with respect to conduction. This allows us to neglect convection in the heat equation and conditions 1 and 2 (slow bubble growth) permit a quasistatic treatment.
3. Capillary number $\mathrm{Ca} := \dot{a}'\mu/\sigma$ <<1. Surface tension dominates viscosity and the shape of vapor bubble is determined by gravity and surface tension through solving Young-Laplace Equation.
4. Bond number $\mathrm{Bond} := \left(g\Delta\rho a'^2\right)/\sigma$ <<1. From the dependence on a', this clearly applies when bubble size is small enough. The bubble shape is then simply a section of a sphere. We shall relax this assumption in the later stages of bubble growth.

L. Huang[51] collected the required data for water and concluded that these assumption should be valid for the case of vapor bubble growth up to a radius of ~1mm. Naturally, he (and we) will check *a posteriori* that our results are consistent with these assumptions.

II.2 Governing Equation and Boundary Conditions

It is convenient to define the dimensionless qualities in this chapter before setting up the problem. Dimensionless temperature is defined as $T_\pm := \left(T'_\pm - T'_v\right)/\left(T'_s - T'_v\right)$, where T'_s is the solid wall temperature and T'_v is the saturation temperature of liquid and the subscripts + and - denote the liquid and solid phases, respectively, and all the length in the simulation is scaled by the spherical vapor bubble's radius a'. The conductivity ratio is defined as $\kappa := \kappa_l/\kappa_s$.

We focus on the growth of a single vapor bubble and therefore construct an axisymmetric, cylindrical cell of finite solid and liquid thicknesses, h and H, respectively. The cell is also finite in the radial direction and has the bubble at its center, as shown on Figure II.1. We shall apply periodic boundary conditions on the edge of the cell so as to mimic bubble-bubble interactions. Adjusting the extent of the radial length at which we apply these periodic conditions allows us to explore the effects of different active bubble nucleation site densities.

Under the above assumptions, the heat equations for both the liquid and solid regions reduce to Laplace's Equations:

$$\nabla^2 T_{\pm} = 0 . \qquad \text{(II.0)}$$

We choose a spherical coordinate system (r, θ, ϕ) whose origin is at the center of the bubble. If the bubble is only a section of a sphere, the origin is where the center of the bubble would be if the bubble were extended to a complete sphere. This origin lies a distance d from the planar solid-fluid interface. Let Z be the coordinate perpendicular to the solid-fluid interface with Z=0 at the height of the bubble center. Note that the solid-liquid plane is then at Z=-d. We shall assume the problem is axisymmetric about the Z-axis passing through the bubble center. On the liquid free surface (Z=H-d), the temperature is a prescribed uniform constant and for simplicity, we also prescribe the constant, uniform temperature at the bottom of the solid (Z=-(h+d)). Alternatively, one could also prescribe a constant heat flux at the bottom of the solid, which is the third part of equation (II.1). For simplicity, L. Huang [51] mainly presented results for the case of a prescribed temperature on the solid wall. We shall focus on this case to verify his results.

$$\begin{cases} \begin{cases} T_+ = T_f & at \quad Z = H - d \\ T_- = 1 & at \quad Z = -h - d \end{cases} & Dirichlet \\ \dfrac{\partial T_-}{\partial Z} = j_s := \dfrac{j_s' a'}{\kappa_s (T_s' - T_v')} \quad at \quad Z = -h - d & Neumann. \end{cases} \qquad \text{(II.1)}$$

At the liquid-solid interface, the temperature and heat flux are continuous,

$$\kappa \nabla T_+ \cdot \vec{n} = \nabla T_- \cdot \vec{n} \quad \text{and} \quad T_+ = T_- \quad \text{at} \quad Z = -d \qquad \text{(II.2)}$$

where we treat the temperatures at liquid-solid interface as unknown values.

Because the vapor and the liquid are comprised of molecules of the same species and since their interface is molecular dimension, it should attain local thermodynamic equilibrium on a time scale far faster than macroscopic heat transfer over length scales of the order of a'. Let T_{vl} be the temperature of the liquid-vapor interface. Thus liquid-vapor interface is always assumed in local thermodynamics at its saturation temperature:

$$(T_{v\ell} :=) T_+ = 0 \qquad \text{at} \quad R = 1, Z \geq -d \qquad \text{(II.3)}$$

If the bubble is attached to the solid interface (with a contact angle, measured in the liquid phase φ), there will be a solid-vapor interface as well. Insulating boundary condition is applied

$$\frac{\partial T_-}{\partial Z} = 0 \qquad \text{at} \quad Z = -d \quad \text{for} \quad 0 \leq R \leq R_{CL} \qquad \text{(II.4)}$$

Let R_{CL}:= sinφ (due to scale with bubble radius a') be the radius of the contact line (CL) on the solid-fluid surface and let R_c be the finite extent of the radial coordinate that defines our periodic (by abuse of geometry, since cylinders do not tile the plane) unit cell. For such finite cell radius configurations, periodicity requires the radial flux on the lateral cell boundary to be zero,

$$\frac{\partial T_{\pm}}{\partial R} = 0 \qquad \text{at} \quad R = R_c. \tag{II.5}$$

Note that this quasistatic problem has no time derivative and thus needs no initial condition. Below, when we examine quasistatic bubble growth, we will introduce a condition for the advancement of the liquid-vapor interface with time and a series of models for the motion of the CL with bubble growth. The former condition will derive from the relationship between bubble growth (Volume V') and total heat transfer (Q) for vapor bubble growth or shrinkage,

$$\frac{dV'}{dt} = \frac{Q}{\rho_v h_{fg}} \tag{II.6}$$

where ρ_v is the vapor density and h_{fg} is the latent heat for evaporation.

II.3 Numerical Procedure

We use the boundary integral equation method[64] to numerically solve the problem we have set up above. This method has clear advantages to finite element methods that discretize the complete domain; the boundary integral method reduces the dimension of the calculation by one and its discretization is restricted only to the boundary. We now present the basic boundary integral equations (BIE) for the boundary integral technique used in this problem. In cylindrical coordinates, p represents an interior "load" point with coordinates (R_p, θ_p, Z_p) and q represents a "field" point on the boundary with coordinates (R_q, θ_q, Z_q). Let

$$m := \frac{2\sqrt{R_p R_q}}{\sqrt{[(R_p + R_q)^2 + (Z_p - Z_q)^2]}} \tag{II.7}$$

and $\boldsymbol{K}(m, \frac{\pi}{2})$ and $\boldsymbol{E}(m, \frac{\pi}{2})$ be the complete elliptic integrals of the first and second kinds respectively, defined as

$$\boldsymbol{K}\left(m,\frac{\pi}{2}\right)=\int_0^{\frac{\pi}{2}}\frac{d\alpha}{\sqrt{1-m^2\sin^2\alpha}} \tag{II.8}$$

$$\boldsymbol{E}\left(m,\frac{\pi}{2}\right)=\int_0^{\frac{\pi}{2}}\sqrt{1-m^2\sin^2\alpha}\,d\alpha \tag{II.9}$$

Let $\vec{e}_R$ and $\vec{e}_Z$ be the unit vectors in the R and Z directions. The unit normal $\vec{n}$ to a boundary surface has components $\vec{n}=n_R\vec{e}_R+n_Z\vec{e}_Z$. Also, let Φ be the axisymmetric Greens function (the second kernel K_2 (p,q)) for Laplace's equation in these coordinates,

$$\Phi(p,q)=K_2(p,q)=-\frac{m\boldsymbol{K}(m,\frac{\pi}{2})}{2\pi^2\sqrt{R_pR_q}}. \tag{II.10}$$

Its gradient (the first kernel K_1 (p,q)) is

$$\begin{aligned}\nabla_q\Phi(p,q)&=K_1(p,q)\\ &\frac{m}{4\pi^2R_q\sqrt{R_pR_q}}\left[\boldsymbol{K}\left(m,\frac{\pi}{2}\right)-\frac{R_p^2-R_q^2+(Z_p-Z_q)^2}{(R_p-R_q)^2+(Z_p-Z_q)^2}\boldsymbol{E}\left(m,\frac{\pi}{2}\right)\right]n_{R_q}\\ &-\frac{m}{2\pi^2\sqrt{R_pR_q}}\left[\frac{Z_p-Z_q}{(R_p-R_q)^2+(Z_p-Z_q)^2}\boldsymbol{E}\left(m,\frac{\pi}{2}\right)\right]n_{Z_q}\end{aligned} \tag{II.11}$$

After taking the interior point p to a boundary point P, we obtain the boundary integral equation for our temperature distribution bounded by a surface is:

$$\begin{aligned}C(P)T(P)+\int_\Gamma T(q)\nabla_q\Phi(P,q)R_q\,d\Gamma\\ =\int_\Gamma\Phi(P,q)\nabla_qT(q)R_q\,d\Gamma\end{aligned} \tag{II.12}$$

where C(P) is π/2 because Γ in our calculation is a continuous surface.

By dividing the boundary path Γ into a set of elements, we numerically implement these required integrations. There are some different methods to divide the boundary; we use isoparametric quadratic elements to carry out these numerical integrations. The details of dividing the boundary into isoparametric quadratic elements and integrating the kernels, including the singular one when P and q are at the same elements refers to that A. A. Bakr[64] developed in his textbook.

Furthermore, our heat conduction calculation in an axisymmetry domain involves solid and liquid sub-domains with thermal conductivities of κ_s and κ_l. Continuity condition will be applied at their common boundary, i.e. liquid-solid interface as such:

$$T_s = T_l$$
$$\kappa_s \left(\frac{dT}{dn}\right)_s = -\kappa_l \left(\frac{dT}{dn}\right)_l \qquad \text{(II.13)}$$

Negative sign means the different direction of the heat flux. Therefore, solid and liquid phase are coupled by a set of linear algebraic equations which can be solved by Gaussian-Jordan elimination.

II.4 Special Treatment of Contact Line (CL)

Due to the existence of a three-phase contact line when bubble attach to the solid-liquid interface, one encounters technical difficulties in that both the geometric and physical boundary conditions become singular there. That is, the insulating boundary conditions of the dry spot, the temperature and flux continuity conditions of the liquid-solid interface, and the zero temperature condition of the bubble surface all overlap there. This contact line region will turn out to be critical in this study and must therefore be handled carefully and accurately. The boundary integral equation method involves integrals over the entire boundary of the system, which, in our case, includes the contact line. Unfortunately, the integrands tend to diverge strongly in these regions, as one has seen previously in Sadhal's elegant analytic solutions[46] of a similar problem, but one having solid and liquid regions semi-infinite in extent, the integrands tend to diverge strongly in these regions, even though the integrals themselves are finite. In order to accurately calculate them, the most promising approach would be to derive an analytic solution (say, from Sadhal's solution) that is valid along the boundary very close to the contact line, and to integrate this limiting form analytically out to a point where one could connect to the full boundary integral equation integrands. Due to technical complexities of this method, L. Huang[51] was forced to develop both a special meshing technique and an asymptotic analytic solution to avoid the singularity of the CL. That is, since the only analytic form solution that seemed possible was Sadhal's solution to a different, but related problem, he presumed that the solution extremely close to the CL was insensitive *in form* to the far-away boundary conditions at the far solid and liquid surfaces, Z=H-d

and Z=-(h+d), but could differ by a factor to be determined in the calculations. He drew a very small circle (its radius around 0.001 of CL radius) in the R-Z plane around the contact line (which he called an asymptotic ring). Since this is a quasisteady formulation that conserves heat, rather than integrating through CL, he was able to replace the portion of the solid-vapor and solid-liquid boundaries inside this asymptotic ring with the integral along the perimeter of this ring from its intersection with the solid-vapor boundary through the solid and liquid phases, until it intersects the liquid-vapor interface. See Figure II.2[51] for node placement that L. Huang used on and close to the asymptotic ring to facilitate his computations. Each physical node at the intersection of the asymptotic ring with each phase boundaries contains temperature and its gradient that includes 2 components: one normal and one parallel to the boundary of the asymptotic ring. In his work, four labels to the physical node at this intersection are assigned, where two are in the liquid phase and represent the normal and tangential components of the temperature gradient, which can be calculated from the liquid phase. The remaining two labels are in the solid phase and represent normal and tangential components of temperature gradient, which can be calculated from the solid phase. Each component of the flux at the intersection can be calculated from the solid and liquid phases. The distances between this node and the nearest phase boundary nodes not on the asymptotic ring are the same as those between nodes on the asymptotic ring. The distance to each subsequent node along that phase boundary is 1.5 times that to the previous node until the distance between the two nodes reaches a maximum length determined by the global size of the cell. Some of the new parameters will be determined by requiring them to give the same values, such as A_+ and A_-, which must both equal A^* in equation II.14 and II.15. More details of this discussion can be found in L. Huang's dissertation[51]. Since heat is conserved, the total heat that crosses the boundary of this closed region must be zero. Thus the magnitude of the heat source/sink at the CL plus that across the small portion of the bubble surface inside the asymptotic ring must equal the integral of the heat flux around the balance of the boundary of the asymptotic ring. As suggested above, he then derived an asymptotic form of Sadhal's solution that is valid very close to the CL, but with an as yet undetermined multiplicative constant (again as long as R_c is not too close to one, the form of the temperature field in the region immediately adjacent to the contact region is

insensitive to far away conditions) to prescribe the temperature fluxes on the ring needed for the integrals shown.

These are the temperature solution in liquid and solid that Huang[51] developed:

$$T_+ = A^* \sqrt{2\cosh\xi - 2\cos\eta}\, e^{-\xi/2} e^{-\xi\beta} \sin\beta(\varphi-\eta)\cos\pi\beta \qquad \text{(II.14)}$$

$$T_- = A^* \sqrt{2\cosh\xi - 2\cos\eta}\, e^{-\xi/2} e^{-\xi\beta} \cos\beta(\eta+\pi)\sin\varphi\beta\,. \qquad \text{(II.15)}$$

where $\eta = \arctan\left(\dfrac{2c(Z+d)}{(Z+d)^2 + R^2 - c^2}\right)$ and $\xi = \tanh^{-1}\left(\dfrac{2cR}{(Z+d)^2 + c^2 + R^2}\right)$ are the standard toroidal coordinates[65]. Notice that T_+ and T_- should have different magnitude A_+ and A_-, but they can be reduced to one constant A^*. In these coordinates, the flux at the asymptotic ring is regulated by

$$\frac{\partial T_\pm}{\partial n} = \frac{1}{H_\eta^2}\left\{\left(\frac{\partial T_\pm}{\partial\xi}\frac{\partial R}{\partial\xi} + \frac{\partial T_\pm}{\partial\eta}\frac{\partial R}{\partial\eta}\right)\vec{e}_R + \left(\frac{\partial T_\pm}{\partial\xi}\frac{\partial Z}{\partial\xi} + \frac{\partial T_\pm}{\partial\eta}\frac{\partial Z}{\partial\eta}\right)\vec{e}_Z\right\}\cdot\vec{n} \qquad \text{(II.16)}$$

where $H_\eta = H_\xi = c/(\cosh\xi - \cos\eta)$.

L. Hunag[51] employed least square method to determine the magnitude A^* which is an unknown coefficient in expressions above. He suggested that for each of the solid-vapor interfacial nodes whose distance close to the contact line, say, less than 5% (small enough so that the limiting form of Sadhal's solution is still accurate) of the radius of the contact line, the temperature value for analytic solution should agree with the boundary integral values.

II.5 Results for Static Suspended and Attached Bubble

Let Q_s be the total heat across the solid-liquid interface in the presence of the bubble and Q_{sN} be the total heat across the solid-liquid interface without the bubble. We plot the heat enhancement defined as Q_s / Q_{sN} as a function of vapor bubble position for conductivity ratios (κ 0.001and 0.1) in Figure II.3. L. Huang[51] calculated this and we check our code by reproducing his results. The conditions for this calculation are R_c= H= h= 5, T_s=1 and T_f =T_v =0. Let δ:=(d-1)/2, then positive, zero and negative correspond to a bubble detached from, tangent to or attached to the heater surface. Let $\kappa=\kappa_l/\kappa_s$, the ratio of liquid to solid thermal conductivities, then small κ corresponds to highly conducting solid. Notice that, for highly conducing solid case, the heat enhancement

jumps almost discontinuously by an order of magnitude when looks from right to left in the figure, as the detached vapor bubble becomes tangent to the solid surface and a three-phase CL appears. We also find that the conductivity of solid (or the conductivity ratio) has a strong effect on the heat enhancement. The reason for this dramatic effect is that, in the absence of a three phase contact line, the much more highly conducting solid would be nearly isothermal at the temperature of the heater, and only begin to rise when the relatively "cold" bubble (at T_{sat}) is extremely close to it so as to be able to influence its temperature. As a result, nearly the entire thermal load would be taken over the superheated liquid (with low thermal conductivity relative to the solid) between the solid-liquid and bubble surfaces. The quasi-steady heat flux is roughly equal to the product of the low liquid thermal conductivity and the temperature gradient across it. In contrast, the existence of the contact line, the coincidence of the vapor-liquid interface and the solid-liquid surface, causes the local region of the solid-liquid surface to be dramatically cooled to the fluid's saturation temperature, which shifts the thermal load from the poorly conducting liquid to the highly-conducting solid near the contact line. This shift means the steady heat flux is now the product of the highly thermal conductivity of the solid and the large thermal gradient, which greatly increases the overall steady heat conduction and, in particular, that through the solid towards the contact line.

Let Q_v be the heat absorbed by the bubble, we plot the fraction $\sigma_{vs} = Q_v / Q_s$, a measure of the amount of heat absorbed by bubble relative to the heat across the solid-liquid interface as a function of ω($\omega := \left(\frac{a}{R_c}\right)^2$) for H = h= 5 and T_f = 0 in Figure II.4. The figure shows that, for various bubble positions and ratios of conductivities, more than 80% of the total heat that passes through the solid-liquid interface enters the bubble, regardless of δ or κ when the radius of the cell is about 3 bubble radii, i.e., R_c=3 ($\omega \approx 0.11$). This results is agreement with the calculations from L. Huang[51]. Obviously, the bubble acts as a heat sink that can draw significant heat from the solid heating wall.

Furthermore, let Q_{CL} be the heat transferred into the CL region, Q_B be the heat transferred from the superheated liquid into the vapor bubble surface and Q_E be the heat that escapes from free liquid surface. There is a discussion in the literature over which of these Qs is more important in nucleate boiling. Therefore, We plot ratios of Q_{CL}, Q_B and

Q_E to Q_s as functions of conductivity ratios for T_f =0 (corresponding to T_{sat}) and T_f=-1 (corresponding to the temperature below T_{sat}) in Figure II.5 (calculation conditions are H=h=5,R_c=2 and φ=120^o). The ratio of Q_{CL} to Q_s decreases whereas Q_B to Q_s increases as the conductivity ratio increases for both T_f =0 and T_f =-1. The reason is that as the liquid becomes more conducting, much more heat bypasses the vapor bubble and conducts though the liquid to evaporate the bubble surface instead of evaporating of the CL. In addition, Q_E has little change as the conductivity ratio increases for T_f =0 and T_f =-1,but Q_s decrease sharply as the liquid becomes more conducting, that's why we see the ratio of Q_E to Q_s increases with conductivity ratio in T_f=0 and T_f=-1. Furthermore, when the temperature at the liquid surface is lower than its saturation temperature (T_f =-1), much more heat leaves the top of vapor bubble surface and conduct through the liquid, finally leaves the liquid surface. Therefore, the ratio of Q_E to Q_s increases higher as the liquid becomes more conducting when the temperature of liquid surface is below its saturation temperature.

Early experimental studies have shown, the heat transfer per unit area and the bubble density (that enters via R_c) obeys a power law relationship with powers varying from 1/3 to 1 according to various authors[6,9,66,67]. In our simulation, we assume that an embryonic water bubble grows in a composite cell of a 5 mm thick (thermal) layer of liquid over a 5 mm thick solid (H′ =h′ = 5mm). The pressure is atmospheric, the gravitational acceleration is 9.807m/s^2 and the temperature at the top of the liquid surface is the saturation temperature (373°K). Other properties of the water are: vapor density 0.60kg/m^3; liquid density 958kg/m^3; latent heat 2257kJ/kg; liquid heat capacity 4.184J/kg/°K; surface tension 0.0589kg/s^2; liquid kinematic viscosity 0.2818×10^{-6}m^2/s; liquid diffusivity 0.168×10^{-6}m^2/s and liquid conductivity 0.680J/m/°K/s. Figure II.6 shows that our simulations are agreement with the power law relationship between heat transfer per unit area and bubble density for different conducting solid and different bubble position. Furthermore, the powers that one finds from these plots all lie in the experimentally reported range of 1/3-1[6,9,13,66,67].

Finally we reconstruct the boiling curve that has appeared to be qualitatively universal for both experimental and theoretical studies since the 1930s. Since our calculation focuses on the growth of a small, single vapor bubble that is undeformed by

gravity, and its interaction with neighboring bubbles via the periodic boundary condtion at R_c, it is only reasonable to compare the results of our calculation with the region to the left of the "jets and columns" sub-region of the nucleate boiling regime, i.e., to the "single bubble" sub-region. We shall return to this comparison after having discussed bubble deformation and detachment. In order to carry out this simulation we need to input an empirical relationship between nucleation site densities (N) and wall superheat (ΔT). L. Huang[51] derived $N \propto (T_w - T_{sat})^2$ from the most widely used Rohsenhow correlation[9] for nucleate boiling states:

$$\frac{c_p (T_w - T_{sat})}{h_{fg} P_r^s} = C_{sf} \sqrt[3]{\frac{q}{\mu h_{fg}}} \sqrt{\frac{\sigma}{g(\rho_\ell - \rho_v)}} \qquad \text{(II.17)}$$

By matching the calculated heat flux ($\kappa = 0.001, \varphi = 90^o$) with the experimental value in the standard boiling curve at superheat 4K, we obtain the constant in the relationship nucleation site densities (N) and wall superheat (ΔT). Figure II.7 reconstruct boiling curves for different solid conductivities and bubble positions. Clearly the upper curves corresponding to attached bubbles, particularly those for the more realistic value κ=0.001, can account for heat flux enhancement represented in this portion of the standard boiling curve.

Again these calculations are based on the assumption of small nondimensional numbers such as Reynolds, Peclet, Capillary and Bond numbers that we proposed at the beginning of this chapter. For the static simulations that we have done in this chapter that do not involve bubble growth, we have not calculated a velocity of vapor bubble growth and cannot yet check these assumptions. Therefore we will present these checks in next chapter after we have simulated bubble growth and check that these non-dimensional quantities are indeed small.

Figure II.1 Geometry and boundary condition of vapor bubble attached in finite cell

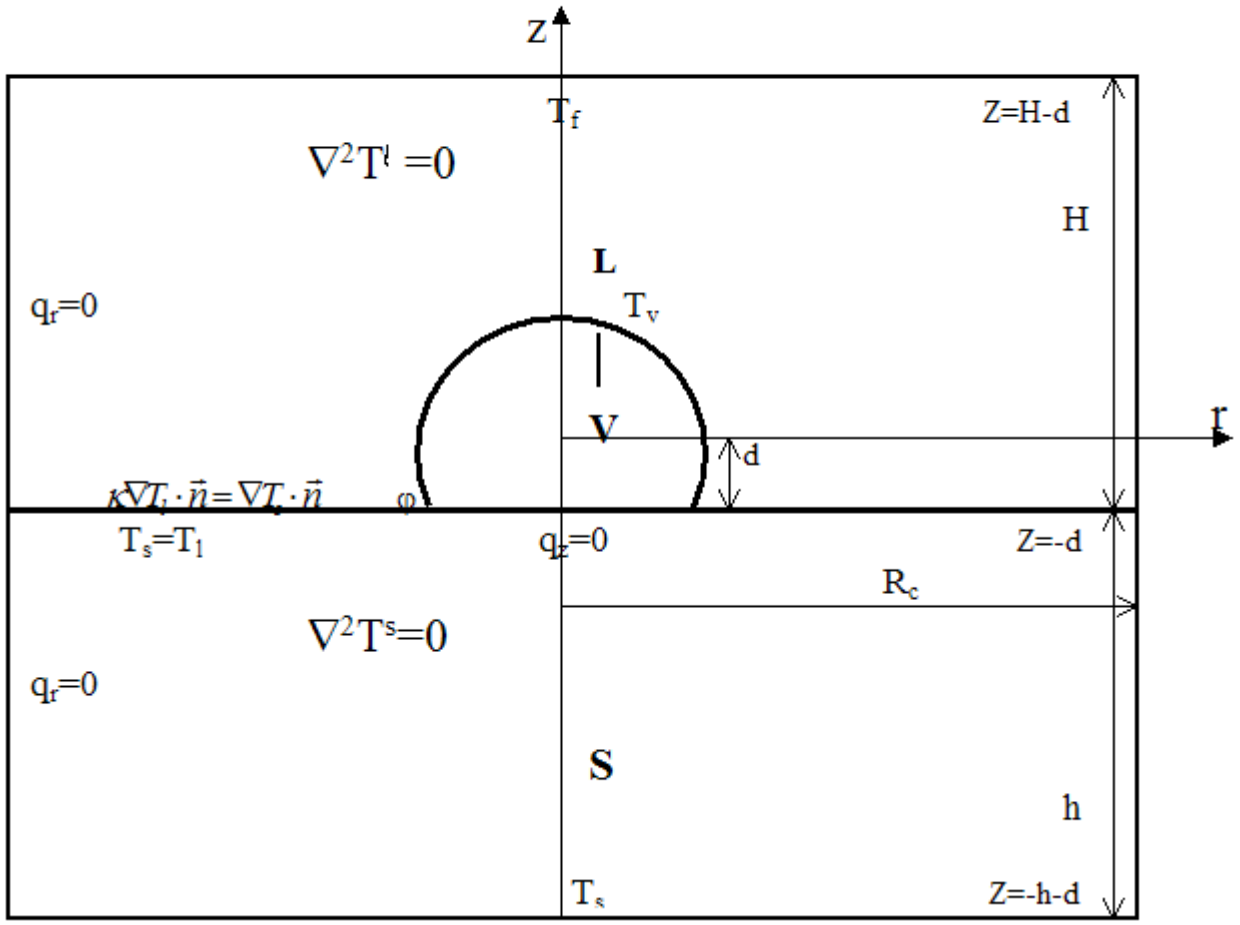

Figure II.2 Special treatment of CL region

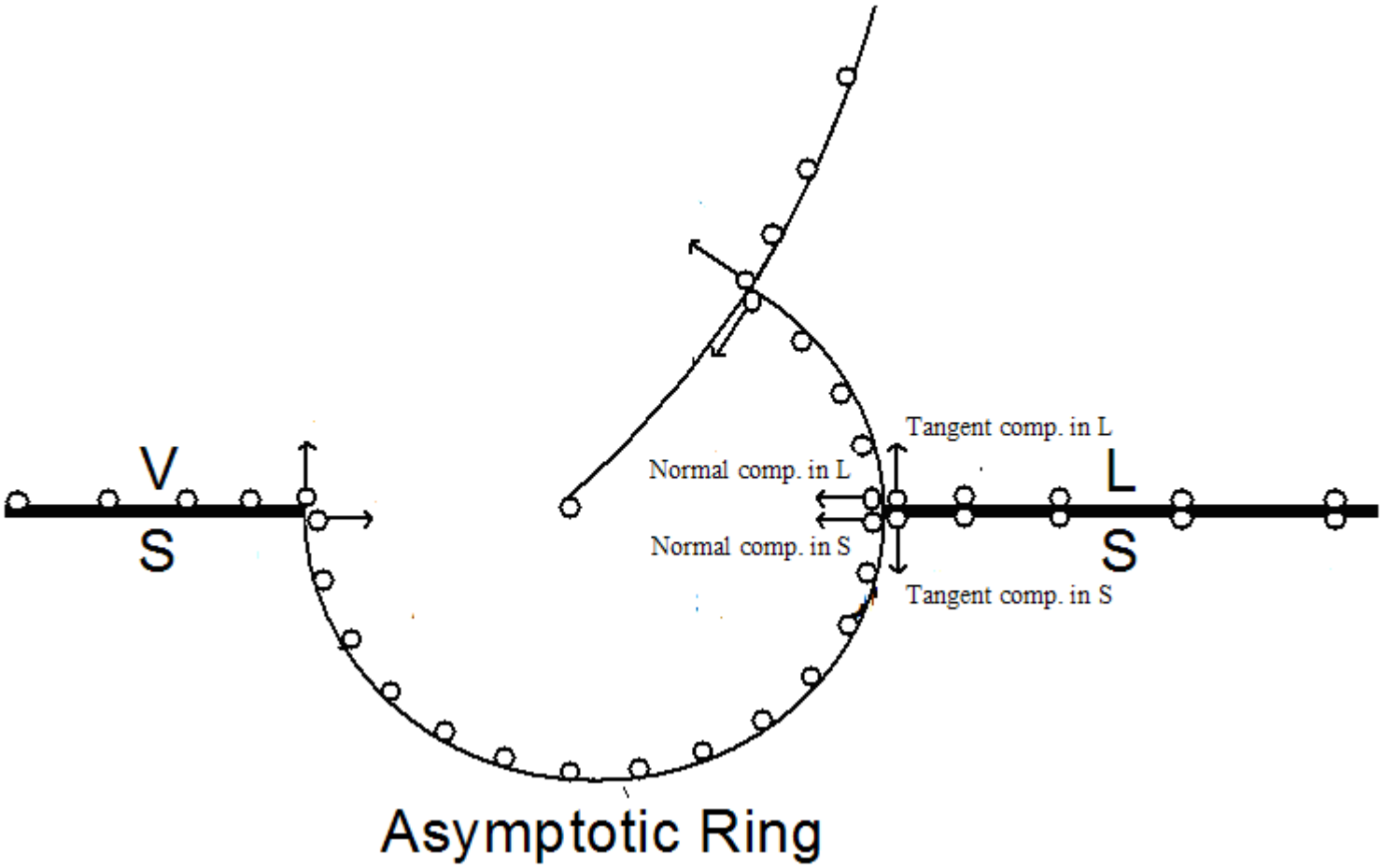

Figure II.3 Heat Enhancement
($T_I = 0$, $H = h = R_c = 5$)

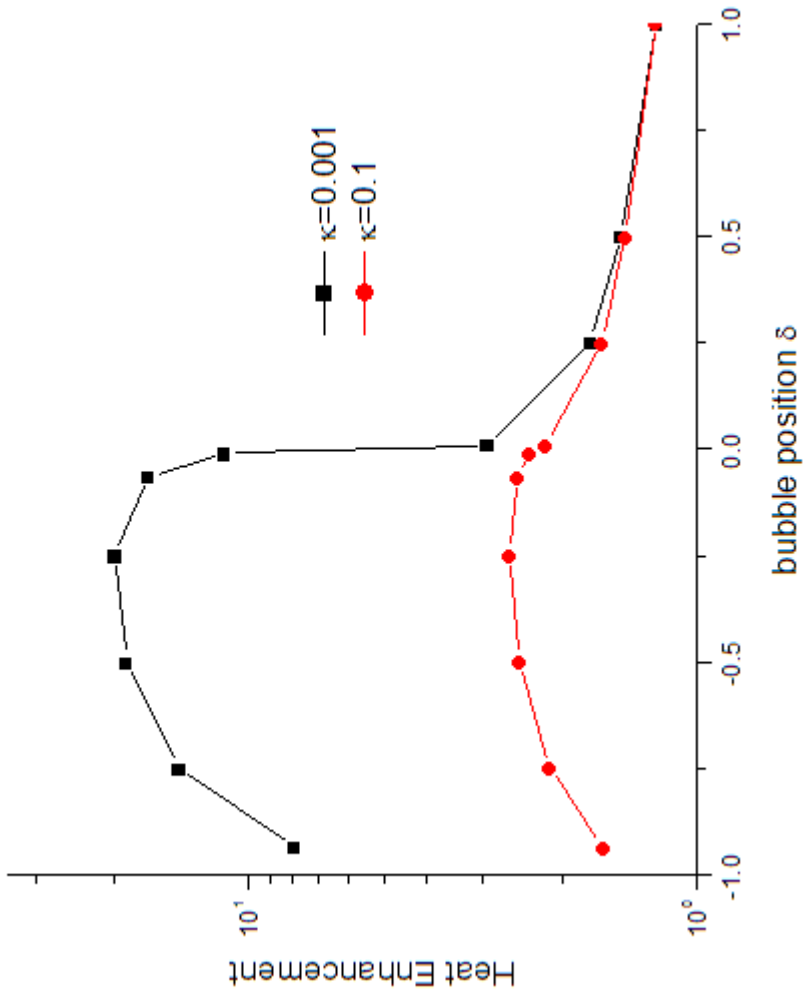

Figure II.4 σ_{vs} Vs bubble density

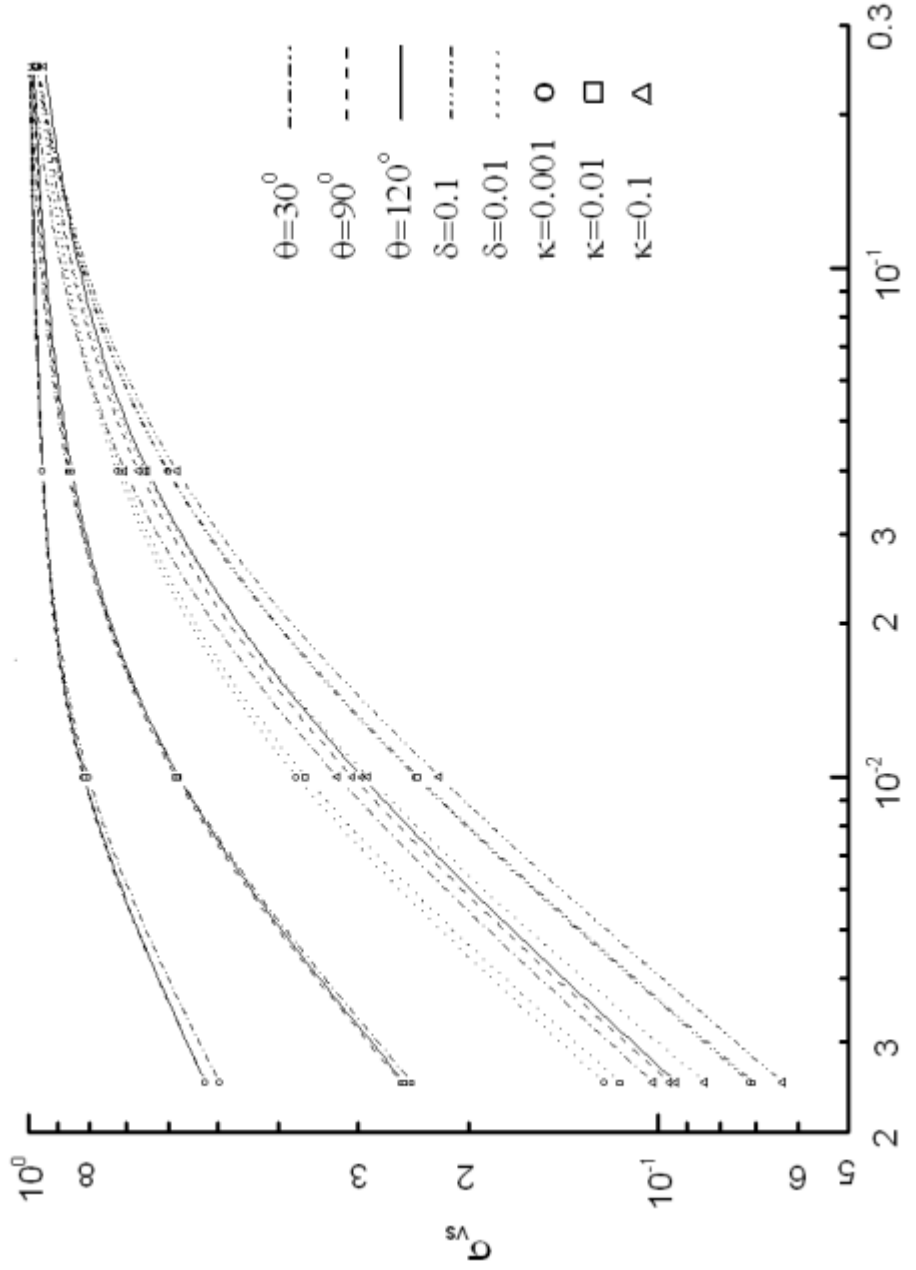

Figure II.5 Heat distribution Vs conductivity ratio
(H = h = 5, R_c = 2)

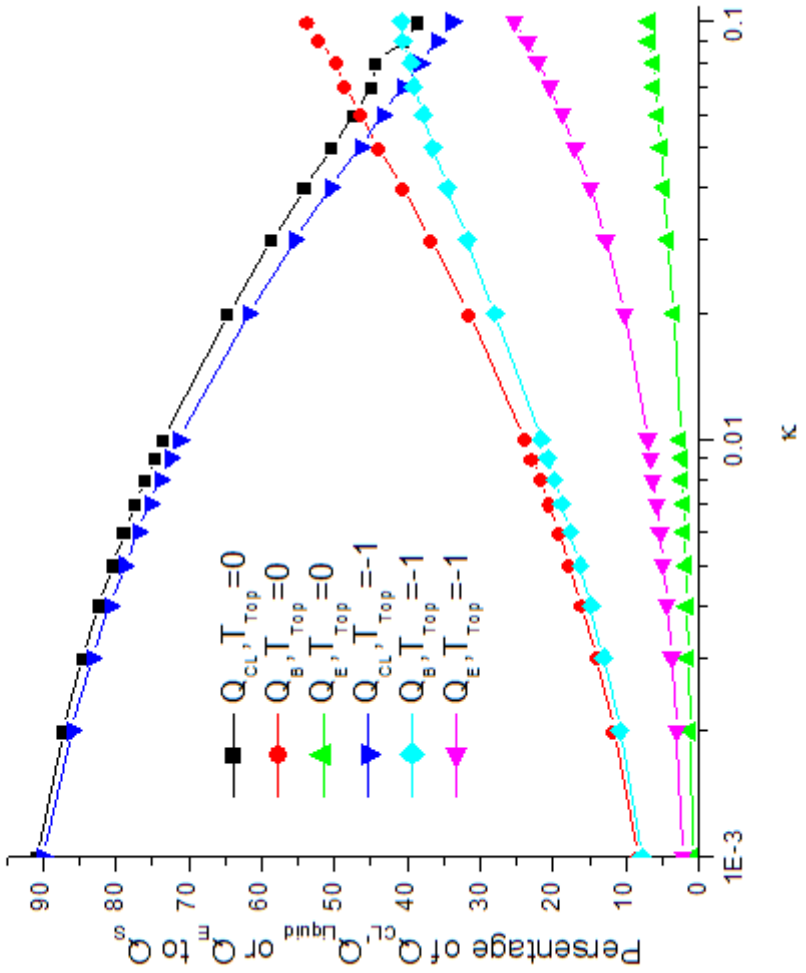

Figure II.6 Power Law Correlation

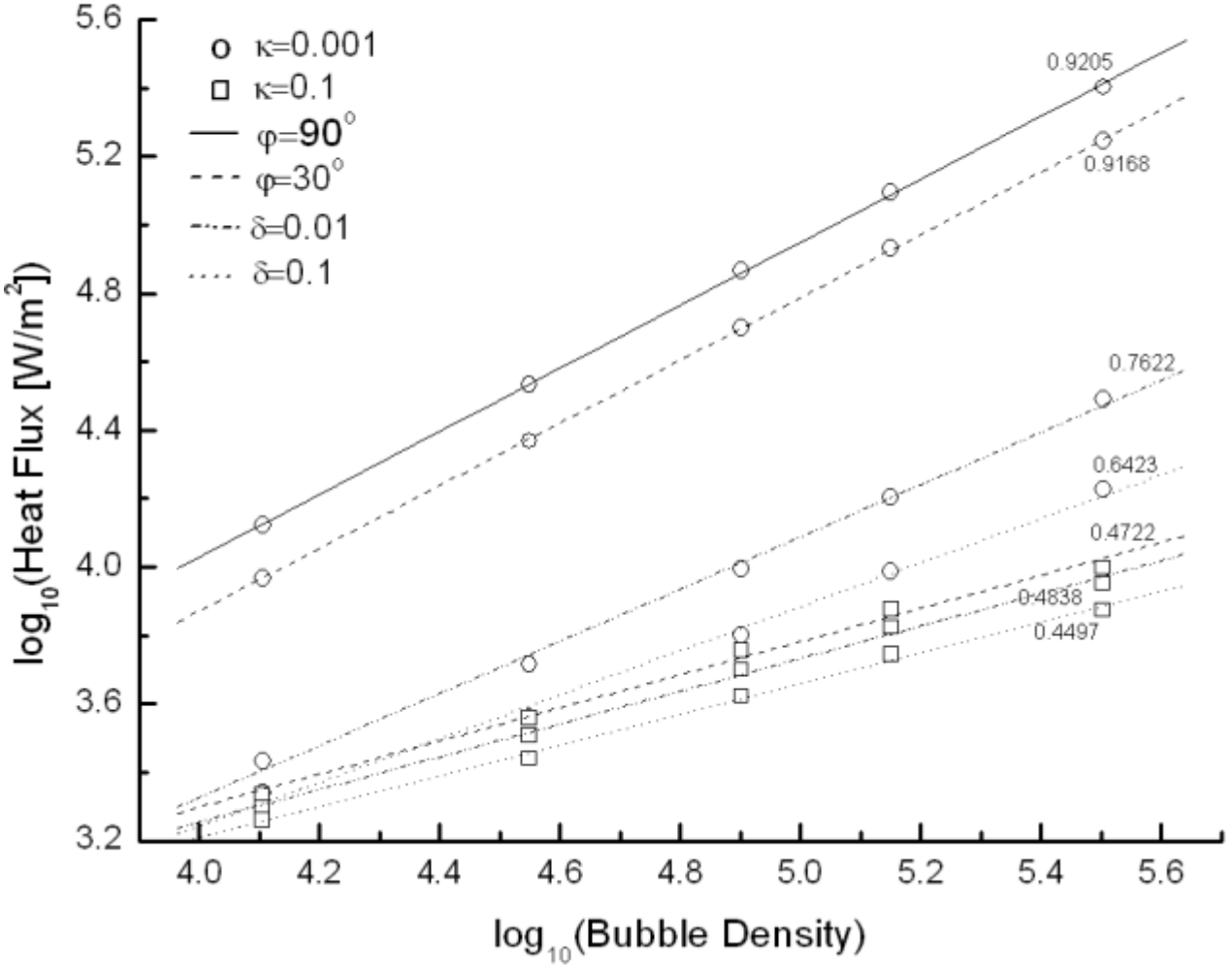

Figure II.7 Reconstruct Boiling Curve

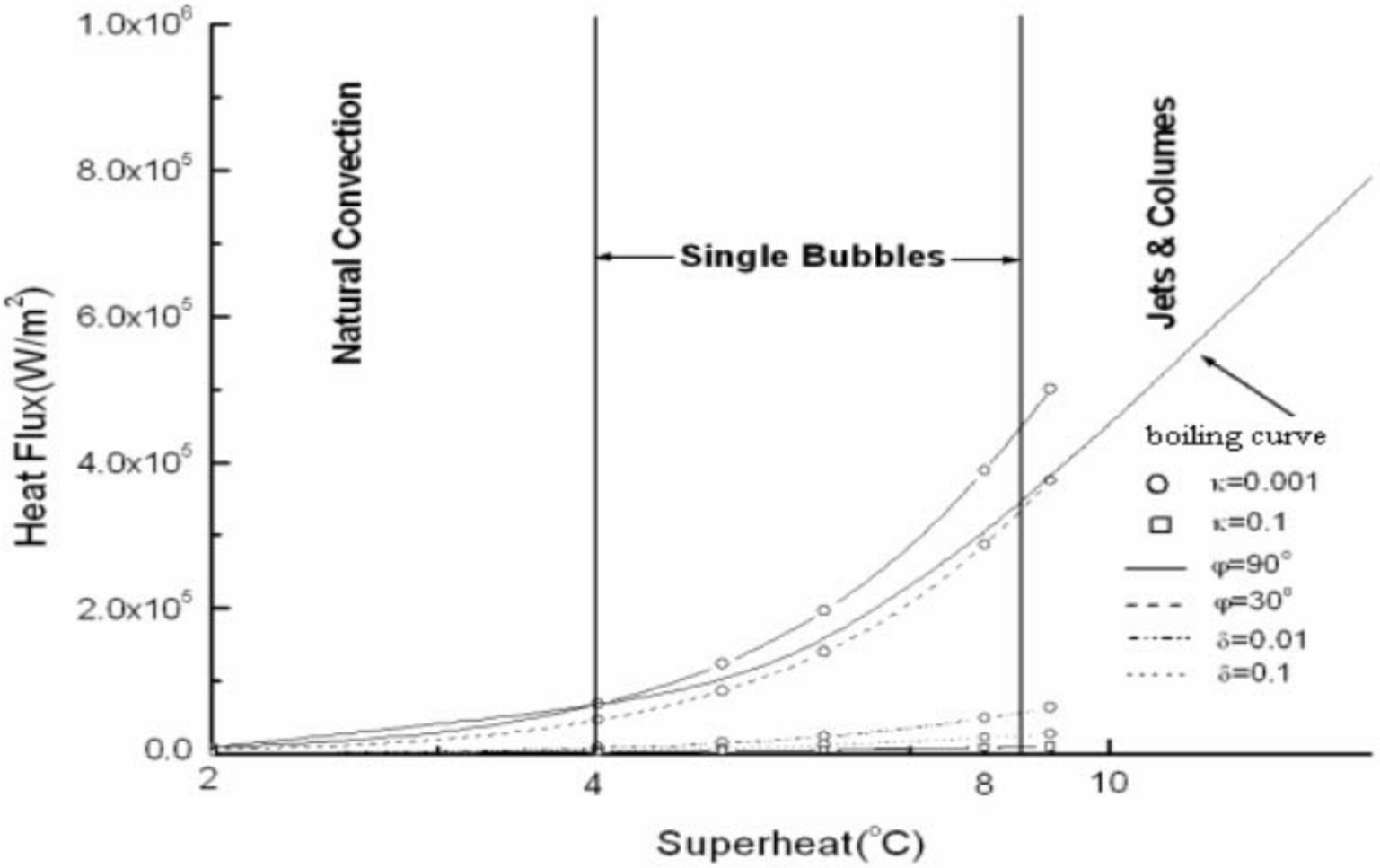

Chapter III

Slow, Solid-Conduction-Dominated Growth of a Vapor Bubble in a Composite Cell

In the preliminary work discussed in Chapter II, we examined the static heat transfer to a spherical bubble. For the case where the thermal conductivity of the solid far exceeds that of the liquid, these results, in the context of our model, indicated that the existence of solid-liquid-vapor CL, which under these circumstances acts as a strong heat sink, is the leading cause of heat transfer enhancement in nucleate pool boiling. In this chapter, we shall depart from that fully static point of view and focus on the quasistatic dynamics of vapor bubble growth in composite cell of finite thickness. This should provide further insight into the dynamics of the complex process of nucleate boiling on a hot solid surface.

III.1 Method for Investigating the Early, Slow, Quasi-static Growth of a Vapor Bubble in the Regime of Solid-conduction-dominated Heat Transfer

Typically in order to nucleate a stable bubble, there is a critical size, below which the bubble collapses and above which it persists. For this critical size, the free energy required for (heterogeneous) bubble nucleation in a cavity on a solid surface is much less than that for nucleation in the bulk liquid[68], since the energy is proportional to the solid angle of surface formed, and the cavity makes it possible to nucleate a bubble with significantly less than 4π solid angle. Since the probability of such a nucleation event is exponential in this energy divided by kT[69], heterogeneous nucleation is essentially all that one will see for small superheat in our system. As such, the cavities (typically of order 1-10μm) act as sites for generation of vapor bubbles. Once a site has been activated, evaporation will begin at the liquid-vapor interface (or the base of the vapor bubble) if sufficient energy is put into the system. When the four nondimensional parameters discussed in Chapter II are indeed small, we can model the slow vapor bubble growth from 4μm (the size of surface irregularities) in radius to 1 mm using quasi-steady heat conduction with a moving liquid-vapor interface in a composite cell. For demonstration purposes, we shall use a cell with a 5 mm thick layer of liquid over a 5 mm thick solid.

The pressure is atmospheric, the temperature at free liquid surface/ top of the thermal layer is 373K and all physical properties used here are the same as in chapter II.

Because of the presence of a bubble with a concave interface, the vapor pressure will change with the bubble radius r_b. The Kelvin equation describes this pressure difference

$$\ln(\frac{P_b}{P_{sat}}) = \frac{2\sigma}{\rho_v r_b R T_v} \tag{III.1}$$

where σ is the bubble's surface tension, ρ_v is the vapor density, P_b is the pressure inside the vapor bubble and P_s is the saturation pressure, R is the universal gas constant. The relationship between the change of pressure and change of temperature in the two phases can be determined by the Clausis-Claperyron equation

$$\ln(\frac{P_b}{P_{sat}}) = \frac{h_{fg}}{R}(\frac{1}{T_{sat}} - \frac{1}{T_v}) \tag{III.2}$$

where h_{fg} is the latent heat, , and T_{sat} is the saturation temperature of the liquid at the pressure P_{sat}. Equating equation III.1 and III.2, we obtain the small curvature correction to the temperature at the vapor-liquid interface

$$T_v = T_{sat}(1 + \frac{2\sigma}{\rho_v r_b h_{fg}}) \tag{III.3}$$

The observations from Griffith and Wllis[70] confirm that the above relationship is indeed satisfied. Bubble radius increases as it grows, as a result, correct saturation temperature T_v decreases and the thermal driving force for heat transfer to vapor bubble increases, thus speeds up vapor bubble growth. This brings into question how long all of the previous assumptions (Small Re, Peclet, Ca, Bo numbers) will continue to hold. Thus it is important for us to reexamine these assumptions after the simulation.

In addition, since the number and size of the time steps necessary for a given accuracy depend on the system parameters, one cannot predict them *a priori*. Instead, we calculate the size of each time step by fixing the maximal allowable fractional change in bubble size. We vary this fractional change and pick an appropriate fraction based on requiring a suitable overall change to be less than one percent for the bubbles growing from around 4 microns to 1 mm. Beyond that size, gravitational effects begin to deform

the bubble from its section of a sphere shape. We shall discuss and calculate this condition in III.4.

III.2 Three ad hoc Models for CL Motion as the Vapor Bubble Growth

As the bubble grows due to liquid evaporation, the three-phase CL may move. The governing equations and boundary conditions do not prescribe its motion with bubble growth, and this motion must be input into our model to make the problem of the growing bubble well-posed. Unfortunately, the physics of contact line motion, even in the absence of phase change at or near the CL, is not well understood and the subject of much discussion and disagreement in the literature[53,71-74]. Here we propose three quite simple somewhat ad hoc CL motion models to consider how different description of its motion affects the rates of bubble growth and heat transfer.

1) The CL is pinned and does not move as the vapor bubble grows. As the bubble grows, then, the contact angle (measured in the liquid) gradually decreases as the volume of the spherical bubble increases and the radius of bubble grows. We carry out the calculation as follows: we prescribe the radius of the CL and keep it fixed throughout the simulation, but allow the initial contact angle to change by virtue of the change in the bubble's volume at fixed contact angle and fixed shape – that of a section of a sphere. This allows us to calculate the vapor bubble's radius and its contact angle. For this geometry, one then calculates the total heat transfer to the vapor bubble from our quasi-static heat conduction model and boundary conditions as given. This heat is completely converted into latent heat to evaporate the liquid and increase the bubble volume. Because we choose the fractional change in volume that is allowed per step, the time step is obtained from the relationship between bubble growth and the heat transfer, $\frac{\mathrm{dV}}{\mathrm{dt}} = \frac{Q}{\rho_v h_f}$. Finally the new contact angle and radius of bubble at this time step is obtained by recognizing that its shape is just the section of a sphere with the fixed contact line and the newly given volume. This process continues until the vapor bubble violates at least one of our assumptions. Figure III.1 and III.2 show the bubble growth and contact angle variation for different volume change fractions. We find that when the fraction is at 0.7% and 0.5%, an overall change less than 0.5% for both bubble growth and contact angle variation; thus we pick volume change fraction as 0.7% in this CL motion model.

2) Equilibrium contact angle. Here we assume that the bubble grows slowly enough and the interface moves slowly enough that the bubble can always find its equilibrium contact angle on a time scale far slower than bubble growth and interface motion. This condition specifies the CL at all times. We carry out the calculation as follows: we prescribe the initial bubble radius and fix the contact angle at its equilibrium value. We then calculate the net amount of heat transferred to the bubble from our quasistatic model and put all of this heat into evaporation. We assume that the bubble instantaneously reorganizes into a section of a sphere with the new volume and with its equilibrium contact angle. This then specifies the instantaneous position of the contact line. The maximum fractional change in radius in a single step is set to 0.28%[51]. Given that contact line velocities can be large (~10m/s), the equilibrium contact angle assumption may not be realistic, In order to more accurately model bubble growth, one needs to physically model the motion of the CL as the bubble grows. Alternately, in Chapter IV, we use molecular dynamics to, among other things, look at the motion of the CL as the vapor bubble grows.

3) Kinematic CL motion. This model assumes that the bubble grows too quickly to instantaneously find its equilibrium contact angle. Rather, as the bubble grows, this model assumes that local evaporation alone determines its contact angle. That is, the bubble's contact angle is simply driven by local evaporation of fluid at the CL with absolutely no additional adjustment. That is, we first calculate the heat transferred to each portion of the liquid-vapor interface during a given time step. Since L. Huang's calculations[51] show that almost all of the heat transferred to the bubble is transferred to a very small region in the CL vicinity, we assume the heat evaporates fluid locally from the liquid next to the original CL, which expands it. This region is very nearly a sector of a circle in the R-θ plane, centered at the CL, extending from the liquid-vapor interface through the liquid to the liquid-solid interface; its radius R, i.e, its volume, which determines the time step, is chosen to make an overall change of less than 0.5% for both bubble growth and contact angle variation. Figure III.3 and III.4 show the bubble growth and contact angle variation for different evaporation ratios (r/r_b). We find that when this ratio is 0.0020 and 0.0019, the differences between the values both of the bubble growth and of the contact angle variation are less than 0.8%. Thus we pick the maximum evaporation ratio as 0.0020 in this CL motion model, and this determines the time step.

Interestingly, the combination of the volume expansion of the bubble due to vaporization and this new contact line position may result in a contact angle that can either increase (initial contact angle of 30^o in Figure III.14) or decrease (initial contact angle of 150^o Figure III.14) from one time step to the next.

III.3 Results

Firstly Figure III.5 compares the vapor bubble growths for these 3 different CL models for an initial bubble radius of 4μm (the radius of CL is 4μm for the pinned CL motion model calculation), initial contact angle of 90^o, conductivity ratio 0.0001 and 10K superheat, R_c=2mm and H=h=5mm. All 3 of these models have two growth regions that are evident in these log-log curves, at least the latter of which exhibits power law growth. Clearly the major heat transfer is in this second regime since it represents nearly the whole time period (the plot is log-log) and the rate of bubble growth is far larger there. Notice our simple theory (developed later in this section) for non-pinned CL motion predicts that $R^2(t)\sim R^2(0)+At$ or, by Taylor series expansion, $R(t)\sim R(0)(1+(1/2)At/R^2(0)-(1/8)(At/R^2(0))^2+O(t^3))$, valid for $At/R^2(0) \ll 1$. Actually $At/R^2(0)\sim o(10^{-4})$ in our case, which corresponds to the initial growth phase in Figure III.5.

In principle the vapor bubble can grow to a very large radius with a tiny contact angle in the pinned CL motion model; however, we just simulate its volume to reach to $\sim 10^{-3}$ mm^3 (corresponding to a bubble radius of 60μm and a contact angle of 6^o). This simulation displays a power law (1.24) growth dependence on time in its second growth phase is clearly slightly lower than for the other two models (1.5). However, this power law growth in the pinned CL model is strongly dependent on the conductivity ratios (shown in Figure III.6, 1.24 for κ=0.001,1.41 for κ=0.01 and 1.71 for κ=0.1; the vapor bubble grows fastest for κ=0.001), but not dependent on wall superheat (shown in Figure III.7, 1.24 for all wall superheats at κ=0.001). The bubble grows most slowly in its second growth phase in the CL pinned model. It is widely expected that heat transfer under a higher contact angle would be higher than under a lower contact angle if liquid flows to meniscus is not limited, as is the case in our simulation. This is partly due to the decrease of the contact angle, leaving less and less fluid near the contact line to transport the heat to a region of the liquid-vapor interface just beyond the contact line. That is it affects the portion of the heat apparently that has to transport to the bubble farther from

the contact line, which is a less efficient route. Therefore the lower the contact angle, the slower the growth of vapor bubbles. Figure III.2 shows how the contact angle decreases with vapor bubble growth in fixed CL motion. Compare it with Figure III.5 and notice that contact angle drops slowly, which corresponds to the bubble's first growth regime (up to 10^{-8}s); then it drops quickly, which corresponds to the bubble's transition growth regime (10^{-8}s to 10^{-6}s); and finally it drops slowly again, which corresponds to its second growth regime. In addition, unlike in the other two models, in the fixed CL model the CL cannot grow with the vapor bubble, and this limits the growth of the vapor bubble. In contrast to the pinned CL model, in the other two models, the continuous expansion of the contact line as the bubble grows means that the local heat transfer near the contact line is never inhibited by a heat sink that does not grow with the bubble's size.

Although the kinematic model and the quasi-static model (equilibrium contact angle) show different heat transfer rates, they both show the same power law growth dependence on time which turns out to be 3/2. Below we shall present a simple back of the envelope theory to explain this dependence. This exponent is in agreement with experimental observation of FC72[44] and boiling water[75]. The pinned CL motion model does not follow this scaling, which is no surprise since experimental observation[76,77] does not suggest that the CL is normally pinned in boiling on a fairly smooth surface, we de-emphasize it in our discussions below. We now compare our simulation results using the two other models with experiments on water under atmospheric pressure done by Nonn Jr[78], a prior student in our group. Phase-Doppler Anemometry (PDA) measures the phase difference from the difference in optical path length of reflected ray traveling through the particles to determine the size of these particles. Nonn employed this technique to measure the early stage of vapor bubble growth (from 10 to 540μm) in contact with clean copper heater embedded in a glass silica insulator by controlling the heater flux from the bottom of the solid. Due to high copper conductivity and thin thickness of experimental solid layer, the solid is almost isothermal, thus it gives us little difference between prescribing heat flux and temperature on the bottom of solid. Therefore, in comparison with Nonn's experimental data, we prescribe the temperature of the bottom of solid that Nonn measured at solid surface. Figure III.8 and III.9 show the comparisons of our simulation results with experimental data in different solid wall superheats. The data

indeed exhibit the predicted power law dependence of vapor bubble radius growth on time of 0.5. We find that the experimental data lies in the range between the simulation results based on our two different non-fixed CL motion models. When the superheat is 11.2^{o}C, the experimental data are much closer to the results using the kinematic model; when the superheat is 12.6^{o}C, the experimental data are much closer to the results using the quasi-static model. It is not clear if this difference is significant, since the heating rates differ only slightly; one would expect a significantly faster heating rate to allow the bubble less time to find it equilibrium contact angle, and thus its data should lie farther from the fixed contact angle model's results. These results may indicate that CL motion in reality is more complicated than either of the ad hoc models that we assumed here.

Before proceeding to the analytic theory, we now perform the *a posteriori* check that in our simulations, the Reynolds and Peclet numbers, as well as Capillary number and bond number are indeed small. As we know[51], for water, as long as vapor bubble is small, i.e. the radius of bubble is the order of 1mm or less Bond number is small. Further, as we can see from their definitions, the Peclet number is just the Reynolds number multiplied by a Prandtl number that is a constant of order one for water. Thus we focus only on the Reynolds number. From Figure III.10, we can see that the overall bubble Reynolds number is on the order of 100 for both quasi-static CL motion model and the kinematic CL motion model. At the first glance, it seems that the small Reynolds number (and small Peclet) assumptions are violated. However, according to L.Huang's results[51], for more conducting solids, when vapor bubble is attached to heating surface, almost 90% of the heat transferred to vapor bubble goes to a tiny small region close to CL, which we call the CL region. The size of this region is O (10^{-3}), in terms of non-dimensional arc length parameter s, measured from the contact point along the vapor-liquid interface. Due to the fact that our focus is on the quasistatic heat conduction, and given the fact that nearly all of the conductive heat transfer is to small region next to the CL rather than to the entire bubble surface, we shall use a length scale characteristic of this region in order to assess the relative contributions of conductive to convective heat transfer, i.e., the Peclet (and Reynolds) number, there. Therefore we redefine the local Peclet and Reynolds numbers by length scale s. Figure III.11 plots this adjusted, local Reynolds number as a function of time. Both the quasi-static and kinematic models

satisfy the small Reynolds, Peclet assumptions for this choice of length and velocity. Furthermore, Figure III.12 easily checks the small capillary number assumption (using the bubble radius's growth rate as the velocity) for those two models involved in the motion of the CL.

Next, in order to better understand the mechanism of nucleate boiling heat enhancement, we consider the effects of different system parameters such as the conductivity ratio, superheat and initial contact angle on vapor bubble growth. Clearly, dV/dt scales as the total heat transfer to the vapor bubble. As we learned from L.Huang's results[51], for more highly conducting solids, when the vapor bubble is attached to heating surface, 90% or more of the heat transferred to the vapor bubble goes to a tiny region close to the CL (we assume it as small arc length s). With this and a simple approximation for the thermal gradient in the solid, we write the total heat transferred to the entire bubble surface as

$$Q = (2\pi R_{CL} s)\kappa_s \frac{T_S - T_{sat}}{h_s} \qquad \text{(III.4)}$$

and $R_{CL} = R_b \sin\varphi$ (φ is the contact angle measured in liquid phase). Therefore, dV/dt scales as $\kappa\Delta T\sin\varphi$. In the quasi-static CL motion model, φ is fixed, if we plot $[V(t)-V(0)]/[\kappa\Delta T\sin\varphi.]$ vs t on a log-log scale, then all of the curves for different system parameters should collapse into one curve, This is shown in Figure III.13. They all show the power law growth of bubble volume with time of 1.5. In the kinematic CL motion model, although we choose different initial contact angles (30^o, 90^o, 150^o), Figure III.14 shows that after initial very short time of variation in contact angle, the vapor bubble seems to maintain a constant contact angle (58^o, 89^o, 86^o corresponding to above cases respectively). So instead of the using initial contact angle, we use this constant contact angle in $\kappa\Delta T\sin\varphi$ and again plot $[V(t)-V(0)]/[\kappa\Delta T\sin\varphi_{eq}]$ vs t on a log-log scale in Figure III.15. Again we can see all these curves collapse into one curve and all show the power value is 1.5. Figure III.13 and Figure III.15 tells us the bubble growth satisfies a power law (1.5) independent of system parameters such as conductivity ratio, wall superheat and initial contact angle. More importantly, it is also the same for two of our CL motion models, but not for the pinned CL model.

Simple theory for $t^{3/2}$ Recall that, independent of parameter values, the second growth regime in both CL motion models follows the same power law $V(t)-V(0)\sim t^{3/2}$ as $t\to\infty$. We now develop a simple physical theory to explain this observation. The growth of the vapor bubble is due to the evaporation of liquid adjacent to the CL, with heat supplied by heat transferred to the CL, i.e.,

$$\frac{\mathrm{dV}}{\mathrm{dt}} = \frac{Q}{\rho_v h_{fg}} \tag{III.5}$$

where the total heat is calculated from equation III.4 and after substituting III.4 into III.5 and collecting the constants, we obtain the following:

$$\frac{dV}{dt} = (2\pi R_{CL} s)\kappa_s \frac{T_S - T_{sat}}{h_s \rho_v h_{fg}} \tag{III.6}$$

Suppose the volume of the vapor bubble is approximately equal to a constant fraction η times $\frac{4}{3}\pi R_b^3$ and that the radius of CL grows in proportion to the radius of vapor bubble. Under these circumstances, Equation III.6 reduces to

$$\frac{dR_b^2}{dt} = \frac{s}{h_s \rho_v h_{fg} \eta}[\kappa_s \Delta T \sin\varphi] \tag{III.7}$$

That means that $R_b(t)-R_b(0)\sim At^{1/2}$, or $V(t)-V(0)\sim At^{3/2}$,

where $A=\frac{s}{h_s \rho_v h_{fg} \eta}[\kappa_s \Delta T \sin\varphi]$. For the case of a fixed equilibrium contact angle, both of the above suppositions are satisfied exactly, i.e., $\eta=\frac{1}{2}(1+\cos\varphi)$ and self-similarity of the growing bubble guarantees that the radius of CL is exactly proportional to the bubble radius. For the kinematic model, figure III.16 shows that the contact line grows very nearly in proportion to the bubble radius with the slope $\sin\varphi_{eq}$, where φ_{eq} is the constant contact angle after a short time.

III.4 Slow Growth of a Vapor Bubble under the Influence of Gravity until Detachment

As we noted before, as the bubble grows it starts to violate the assumptions of sphericity (Bond and/or Capillary numbers become too large), quasi-static growth (Reynolds and Capillary numbers too large) and dominance of conduction over

convective heat transfer (Thermal Peclet number too large). These are all serious issues, but they may or may not occur simultaneously. Introducing all of these complications into the problem at once would render it far too complicated to solve by the methods used above. Instead, we focus on the addition of one complication at a time. Our calculations thus far indicate that the capillary number of the bubble (the ratio of viscous force to surface tension) remains below 10^{-2}-10^{-3} during vapor bubble growth for small enough ΔT ($10^{o}C$). As such, when the vapor bubble grows to a size where its Bond number (the ratio of gravity to surface tension) is no longer small, bubble begins to deform from its spherical shape, but still satisfies the other three nondimensional parameter conditions. Due to the small capillary number of the vapor bubble, its new shapes are still (static, just now, non-spherical) solutions of the Young-Laplace equation[79,80] for a given bubble volume (prescribed by the calculated vaporization during the previous time step) and for a given contact line, which a choice of CL model decides. Here we consider equilibrium contact angle and kinematic CL models.

The Young-Laplace equation balances surface tension and gravity to determine the interfacial shape in the absence of any significant dynamic forces as:

$$P_0 - \rho_l g z = \sigma\left(\frac{1}{R_1} + \frac{1}{R_2}\right) \tag{III.8}$$

where P_0 is the pressure surplus at apex 0. R_1 and R_2 are the principal radii of curvature.

Figure III.17 shows schematically a vapor bubble growing on a heating surface, in which ϕ is the angle formed by the tangent to the meridian and the horizontal axis. Thus, the principal radii of curvature can be expressed by using differential geometric relations:

$$\frac{1}{R_1} = \frac{d^2 z / dr^2}{[1 + (dz/dr)^2]^{3/2}} = \frac{d\phi}{ds}$$

$$\frac{1}{R_2} = \frac{dz/dr}{r[1 + (dz/dr)^2]^{3/2}} = \frac{\sin\phi}{r} \tag{III.9}$$

Substituting (III.9) into (III.8), we rewrite the Young-Laplace equation:

$$\frac{d\phi}{ds} = \frac{P_o - \rho_l g z}{\sigma} - \frac{\sin\phi}{r} \tag{III.10}$$

$$\frac{dr}{ds} = \cos\phi \tag{III.11}$$

$$\frac{dz}{ds} = \sin\phi \qquad \text{(III.12)}$$

We are also interested in calculating the vapor bubble volume. This is given by

$$\frac{dV}{ds} = \pi r^2 \sin\phi \qquad \text{(III.13)}$$

The numerical procedure is based on guessing an initial value for P_0 and integrating along the curve to desired vapor bubble volume. The CL position obtained is unlikely to be the prescribed value, so we adjust P_0, using the secant method and repeat it until it is.

The system of differential equations is integrated using a fourth order Runge-Kutta integration scheme. We must provide four initial conditions (one for each element in the system). At the apex of vapor bubble where r(0)=0, there is a singularity (both r and sin ϕ are zero there) in the right-hand side of formula III.10. Therefore we integrate from the spot very close to apex as the first step. F. Sheriff[81] developed an analytic solution close to the apex for a dew drop by using truncated series expansions for the variables. We use Taylor series expansions to develop a set of analytic solutions close to the apex but for a vapor bubble. We set up the following expressions:

$\phi(s) = a_1 s + a_2 s^2 + a_3 s^3 + o(s^4)$ (III.14)

$r(s) = b_1 s + b_2 s^2 + b_3 s^3 + o(s^4)$ (III.15)

$z(s) = c_1 s + c_2 s^2 + c_3 s^3 + o(s^4)$ (III.16)

$\cos\phi = 1 - 1/2\ \phi^2 + o(\phi^4)$ (III.17)

$\sin\phi = \phi - 1/6\ \phi^3 + o(\phi^5)$ (III.18)

Then we substitute III.14-III.18 into III.10-III.12 to obtain the analytic solutions for ϕ, r, z and V as functions of s as:

$$\phi(s) = \frac{1}{2} P_O s\left(1 - \frac{1}{8}\frac{\rho_l g}{\sigma} s^2\right) + o(s^4) \qquad \text{(III.19)}$$

$$r(s) = s\left(1 - \frac{1}{24} P_o^2 s^2\right) + o(s^4) \qquad \text{(III.20)}$$

$$z(s) = \frac{1}{4} P_O s^2\left[1 - \frac{s^2}{16}\left(\frac{\rho_l g}{\sigma} + \frac{1}{3} P_o^2\right)\right] + o(s^5) \qquad \text{(III.21)}$$

$$V(s) = \frac{\pi}{8} P_o s^4\left[1 - \frac{s^2}{12}\left(\frac{\rho_l g}{\sigma} + P_o^2\right)\right] + o(s^7) \qquad \text{(III.22)}$$

As the integration proceeds, a check is made to see whether the volume has attained or exceeded the required value. If this check returns the correct volume, integration is stopped. The CL position (either the contact angle or the CL radius) at the required volume is determined accurately by linear interpolation on the CL position and the bubble volume. Two points, say (X_1, V_1), (X_2, V_2), are connected by a straight line, in which X represents the contact angle or the CL radius depending on CL motion models. Then the X_3 at volume V_3 is given by

$$X_3 = X_1 + \frac{X_2 - X_1}{V_2 - V_1}(V_3 - V_1) \qquad \text{(III.23)}$$

The boundary integral calculation we have employed to simulate early stage of vapor bubble growth only requires the bubble shape to be axisymmetric and can, therefore, be easily modified to accommodate any axisymmetric Young-Laplace shape such as those described above. Thus we will be able to follow the evolution of the slowly growing vapor bubble from the time it begins being influenced by gravity until its detachment, which we define below. We hypothesize that right after a vapor bubble detaches, two competing processes occur. If the departing bubble necks and leaves a vapor residue left on the solid surface[27], its CL continues to act as a heat sink, rapidly draw heat through the solid, which tends to grow the bubble. Opposing this trend, the departing bubble causes cooler fluid from above to convect to the surface to replace it, and this cooler fluid will tend to condense the residue bubble. The balance between these two effects, likely dependent on ΔT, determines whether the residue will continue to grow and efficiently draw heat from the heater or be quenched and introduce a (possibly long) delay until a new bubble nucleates there. The former is possibility reminiscent of the "jets and columns" regime and the latter of the "single bubble" regime in Figure I.1. CL motion is critical as an input into the calculation to determine the existence and size of the residue bubble. Therefore we need to investigate how the CL moves during vapor bubble growth. In this chapter we will use the equilibrium contact angle and kinematic models as inputs to simulate vapor bubble growth and detachment. In Chapter IV we will employ Molecular Dynamics to physically trace, among other things, three-phase CL motion. Typically, at some point we define a snap off in the bubble's evolution when a single lobe solution to the Young-Laplace equation ceases exist for the specified volume

and contact line condition. It is then assumed that snapping at the neck's minimum radius represents the detachment process, from which we calculate the detached volume. If the bubble neck's narrowest point has gone through a minimum in one of the immediately preceding time steps, one assumes that this neck is what snaps[82,83].

III.5 Results of Vapor Bubble Deform and Detachment Calculation

First Figure III.18 compares vapor bubble growth prior to and including its deformation and detachment in the two different CL motion models; a small inset expands the portion of the curves corresponding to vapor bubble deformation and detachment. Please note the simulations start at a bubble radius of 4μ and an initial contact angle of 130^{o}, in order to emphasize vapor bubble deformation and detachment, instead of showing their growth from the very start ($\sim 10^{-10}$s). We just show bubble growth from 10^{-4}s in Figure III.18. For both CL motion models, there is a decrease in the otherwise uniform slope of the curve (in a log-log plot) in the late stage of vapor bubble growth. The post-deformation slopes are 1.103 for the equilibrium contact angle model and 1.241 for the kinematic model, both less than 1.5, the value in both models before vapor bubble deformation begins. This indicates that a dramatic change happens when vapor bubble deforms from its spherical shape. We examine the evolution of the radius of CL in Figure III.19. For both of these CL motion models, the radius of CL grows monotonically before vapor bubble becomes large enough to "feel" the gravity. Once it feels gravity, it continue to grow until it experiences an abrupt change in shape, meaning the neck-free shape solution ceases to exist and is replaced by a solution with a neck, as seen in the figure inset. It is this change that results in an abrupt contraction of the bubble's CL radius, the abruptness due to the fact that these are static solutions to the Young-Laplace equation. Notice that the requirement of maintaining the equilibrium contact angle in the quasi-static model results in a sharp drop in the CL radius. In contrast, the kinematic model does not, in principal, permit the CL radius to decrease. However at some time step N, a solution of the Young-Laplace equation given bubble volume V_N and prescribed CL radius $R_{CL}(N)$ cease to exist. We then allow the program to find a solution to Young-Laplace equation that has a single inflection point for this volume V_N and the contact angle φ_{N-1} at the previous step N-1. (Actually π-φ_{N-1} is applied in calculations so that Young-Lapace equation can give a solution with reasonable

physics. This is because Figure III. 14 shows that no matter what the initial contact angle is, before bubble detachment, its contact angle becomes equal to or less than $\pi/2$.) This readjustment at this time step results in an instantaneously shrinkage of the CL radius. In reality (as opposed to in our model), the expansion/contraction of the radius of CL depends on force balance parallel to the wall, which includes surface tension, evaporation momentum, inertia and viscous forces (viscous forces are small in this case). Surface tension force tend to contract the radius of CL, however, evaporation momentum try to expand it. In our model, we include neither fluid mechanics, i.e., viscous forces, inertia nor evaporation momentum, but rather only balance surface tension and buoyancy via the Young-Laplace equation. In the quasistatic model, as the bubble volume increases beyond the largest neck-free shape, further growth at fixed contact angle would require the bubble shape to bend more than surface tension would permit, causing a change in bubble shape having a smaller radius of curvature, which causes surface tension forces to increase. This step change in curvature is coupled to a jump in the surplus pressure at the vapor bubble apex - see Figure III.20. Before the vapor bubble abruptly changes shape, this surplus pressure decreases gradually (via the Young-Laplace equation) as the volume and radius of the vapor bubble gradually increase, but jumps abruptly as the vapor bubble abruptly changes from its spherical to its necked shape to its Young-Laplace necked shape.

Table III.1 considers the effects of various parameters on vapor bubble deformation and detachment. As we already knew, before vapor bubble deforms, the bubble volume grows as $t^{3/2}$; after shape change the bubble's volume growth still follows a power law as t^{y}. However this power y is in the range between 1 and 1.25. The exact number highly depends on the CL motion model that we assume, i.e., y=1.239 in the kinematic CL motion model, compared with y= 1.105 in the quasi-static model for initial contact angle of 90^{o} for wall superheat of 10^{o}C and conductivity ratio of 0.001. However, the degree of superheat and the initial contact angle appear to have little effect on the power. This again indicates that, for a better understanding of the heat enhancement mechanism in nucleate boiling, one needs a better physical understanding of CL motion during bubble growth.

Finally, we look at how the vapor bubble detaches from the heating solid surface in Figure III.21. Because our integration starts from the bubble apex (details refer to section

III.4), we plot the vapor bubble shape from the apex along with its arc length to its CL and all the curves shown in Figure III.21 are plotted on the same length scale. The figure clearly shows the dramatic change in the curvature of vapor bubble shape at the point that the vapor bubble changes from its spherical shape to Young-Laplace shape. Mathematically, as already noted, the Young-Laplace equation can give multiple solutions, but physically we are only interested in the least complicated and most stable solution. From our simulation, when the vapor bubble grows slowly (Ca<<1, Re<<1) for non-zero equilibrium contact angle, it will depart from the heating solid surface in a manner that leaves a vapor residue, and this is the case for both CL motion models that we have assumed. As we have discussed, a vapor bubble residue with a three-phase CL, can significantly enhance heat transfer relative to the residue-free case. We have also calculated the detachment time, detached volume, residue volume and neck position for these two CL motion models, measured from the same initial conditions, e.g., initial bubble volume. Vapor bubbles detach more quickly because they grow faster in the quasi-static CL model (0.00502s) than in the kinematic CL model. There is a larger detached volume (4.11 mm^3) and a smaller residue volume (0.39mm^3) in the quasi-static CL model compared with 3.364mm^3, 1.296mm^3 respectively in the kinematic CL model. The radius of CL at detachment is larger in the kinematic CL motion model. Coupled with its larger residue volume, this model predicts a residue that will be harder to quench. Because vapor bubble detachment causes liquid convection, the larger detached volume and the smaller residue volume in the quasi-static is easier to quench.

S. Gong and W. Ma[77] investigated boiling by means of imaging bubble dynamics in the vicinity of a bubble's nucleation site. They use a silicon wafer with conductivity of 100W/m/K as the heater's surface (corresponding to κ=0.0068). The heating zone is 10mmx10mm locating in the center of the silicon wafer (corresponding to R_c=5.6mm) and the thickness of liquid water is maintained at 7~8mm. The static contact angle is assumed to be 60^o and bubble grows slowly (around 0.1m/s-0.3m/s, which satisfies our assumptions). They measured the CL motion evolution for different wall superheats (Figure III.22 replots their experimental data to show the growth of CL radius with the bubble radius). Notice the CL radius first increases and then decreases abruptly with bubble growth, just as when bubble shape change occurs in our simulation. Using their

experimental CL motion data rather than one of our ad hoc CL motion models, we simulate the vapor bubble growth until detachment. Surprisingly, in Figure III.23, our calculation predicts that the vapor bubble detaches from the heating solid surface without leaving any visible residue. This observation appears to contradict the results from both of our ad hoc CL motion models. Our calculations do suffer from the fact that the CL artificially contracts suddenly at the point of vapor bubble shape change, as opposed to a more realistic, continuous yet rapid CL contraction, and thus the model calculation misses some of the true dynamics, even when growth is extremely slow, during this adjustment time.

Next we simulate the bubble growth process using the experimental CL motion data and compare our results with their data in Figure III.24. With this CL motion model, our simulation shows vapor bubble volume grows with $t^{1.35}$, slower than with our ad hoc CL models, but the experimental data shows that the volume grows as $t^{1.5}$ before the bubble deform from its spherical shape, then decrease to a non-power law growth (i.e., no fix power value). In Figure III.25, we compare the evolution of the contact line radius in from simulation that uses the experimentally determined CL motion with the experimental results for CL radius vs time. The comparison is quite reasonable. Both curves show the same trend: at the beginning before the vapor bubble changes its shape, the radius of CL increases. Then it decreases gradually until the vapor bubble detaches. Again our quasistatic CL model only allows an abrupt change in CL radius and our kinematic model does not have a mechanism to allow CL radius contraction, other than that described above. These are clear shortcomings of these models.

As discussed above, there are approximations in our model formulation based on certain nondimensional groups being small and there is a reliance on a model for contact line motion, a process that is poorly understood. The above figures clearly highlight how the input for CL motion impacts bubble evolution in a particularly strong way once the bubble's equilibrium neck-free shape ceases to satisfy the Young-Laplace equation somewhat after the bubble size exceeds the point where its Bo ~0.1. Clearly, in order to progress, one needs a much better physical understanding of CL motion during the whole process of stable vapor bubble growth. As described in Chapter I, Molecular Dynamics provides the potential for revolutionary insight to the interface and CL motion problems,

problems that are not well understood on the macroscopic level, by dropping down to and gaining insight from the molecular level. In the next chapter, we step down in resolution to this scale in order to consider the problem at the level of individual atoms. Another advantage of going to molecular dynamics simulations is that they, in principle, not only model the conductive heat transfer processes present in this chapter's models, but also the fluid mechanics and associated heat convection as well.

Figure III.1 Bubble growth on different volume change fractions - CL pinned
(κ=0.001,φ_i=90^o,T_w-T_{sat}=10K)

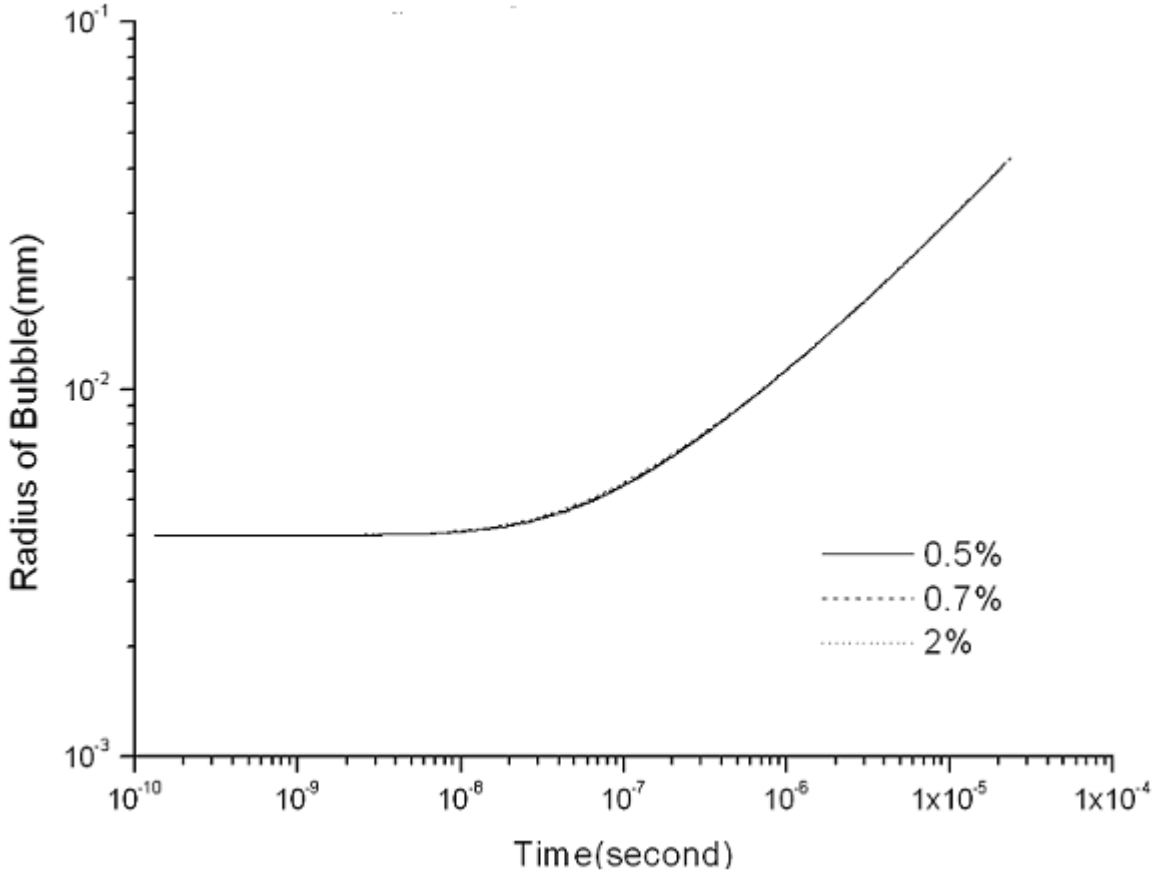

Figure III.2 Contact angle variations on different volume change fractions - CL pinned (κ=0.001,φ_i=90^o,T_w-T_{sat}=10K)

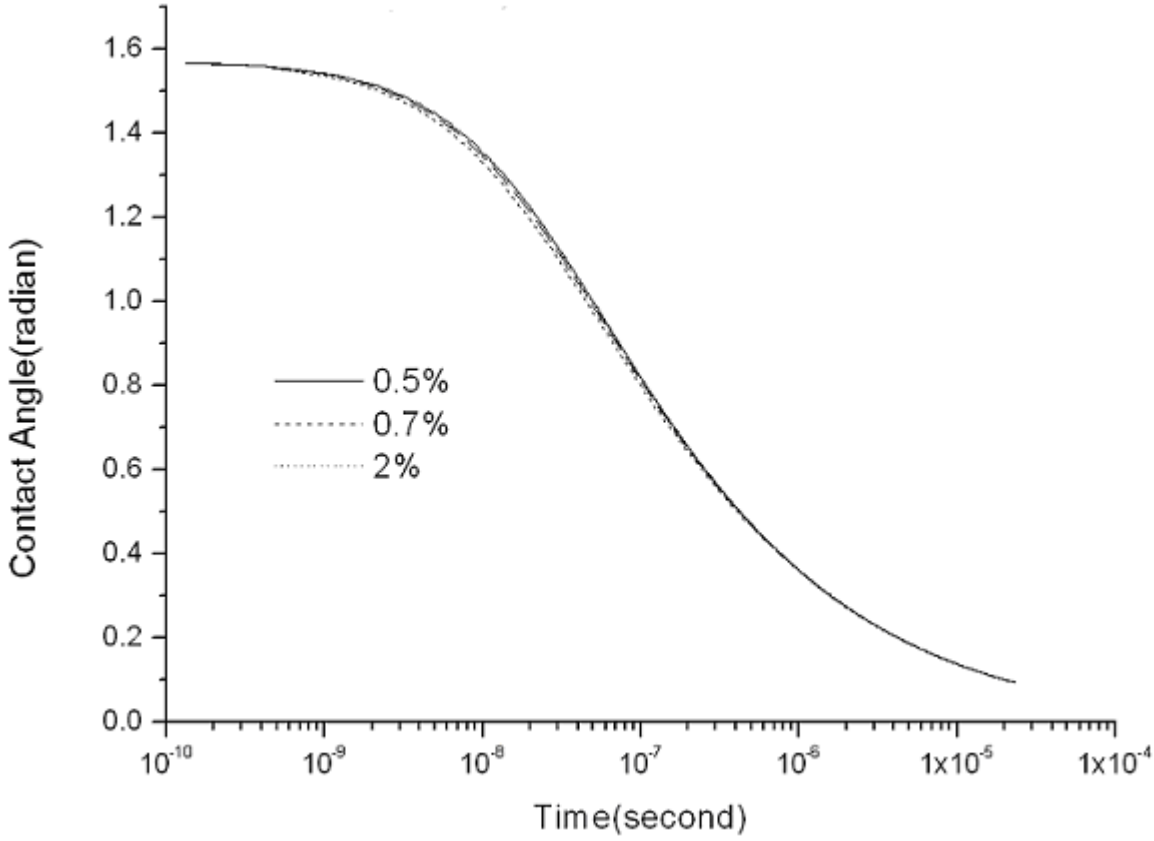

Figure III.3 Bubble growth on different evaporation ratios - CL kinematic
(κ=0.001,φ_i=90^o,T_w-T_{sat}=10K)

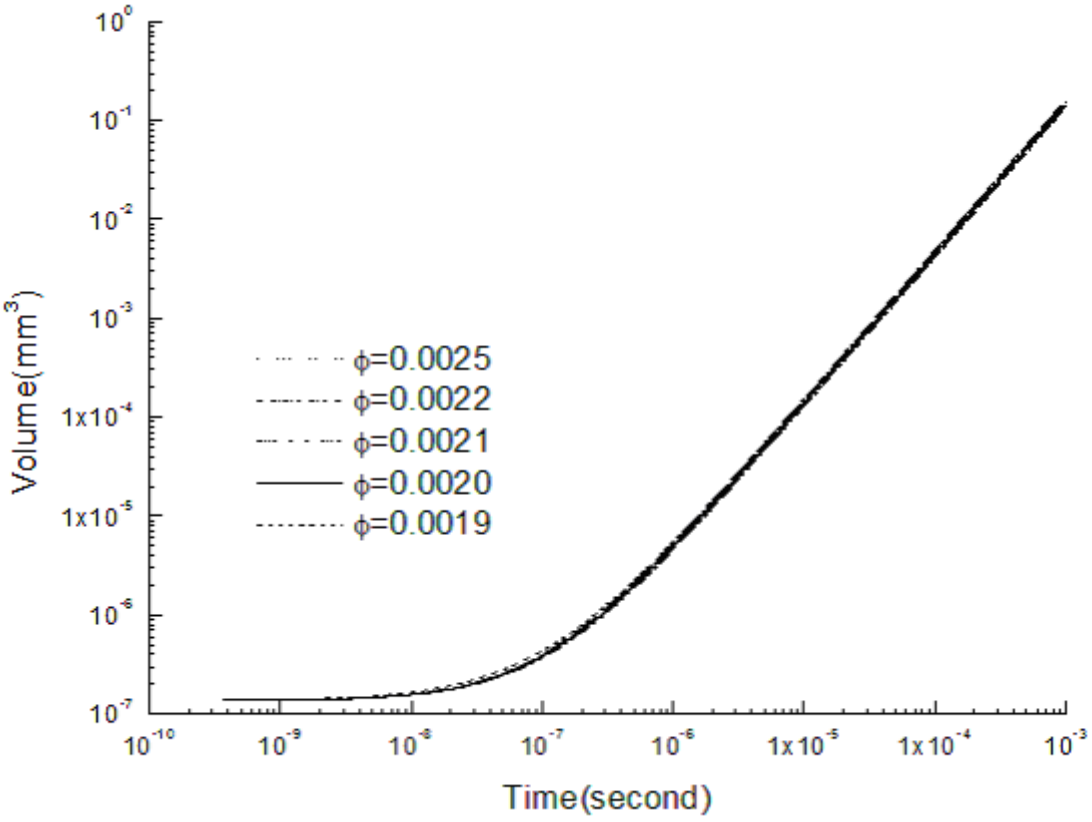

Figure III.4 Contact angle variations on different evaporation ratios - CL kinematic (κ=0.001,φ_i=90^o,T_w-T_{sat}=10K)

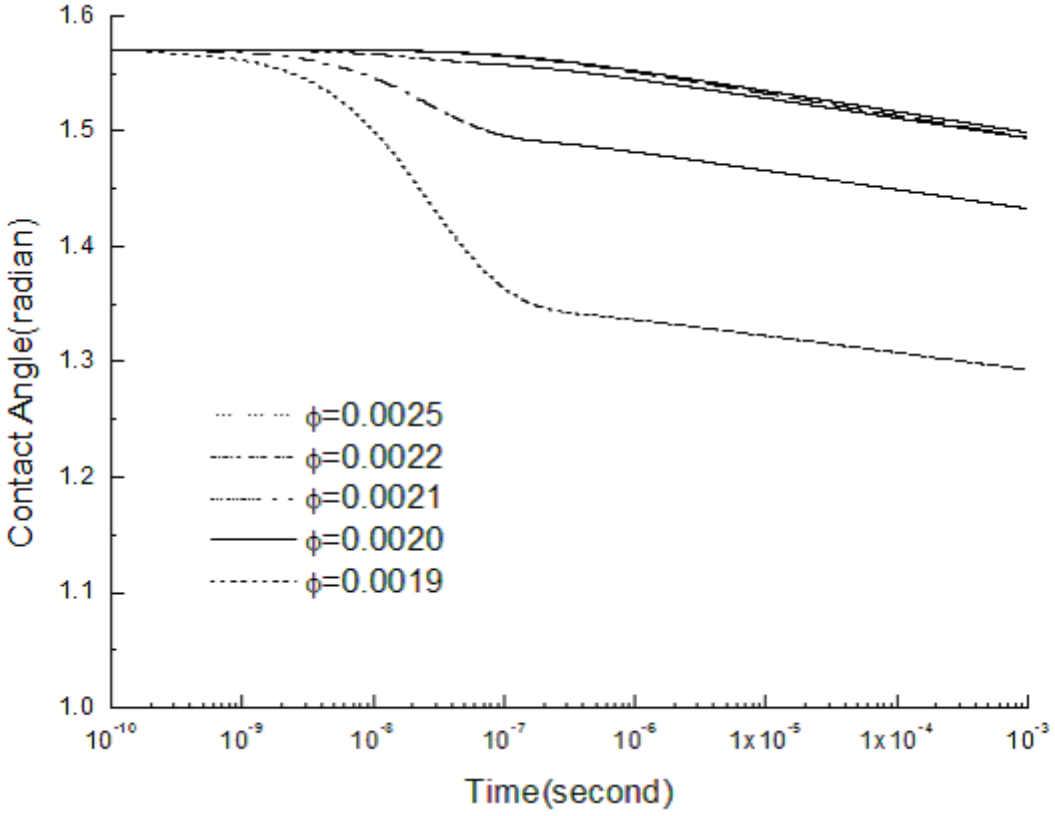

Figure III.5 Vapor bubble growth on 3 different CL motion models
(κ=0.001,φ_i=90^o,T_w-T_{sat}=10K)

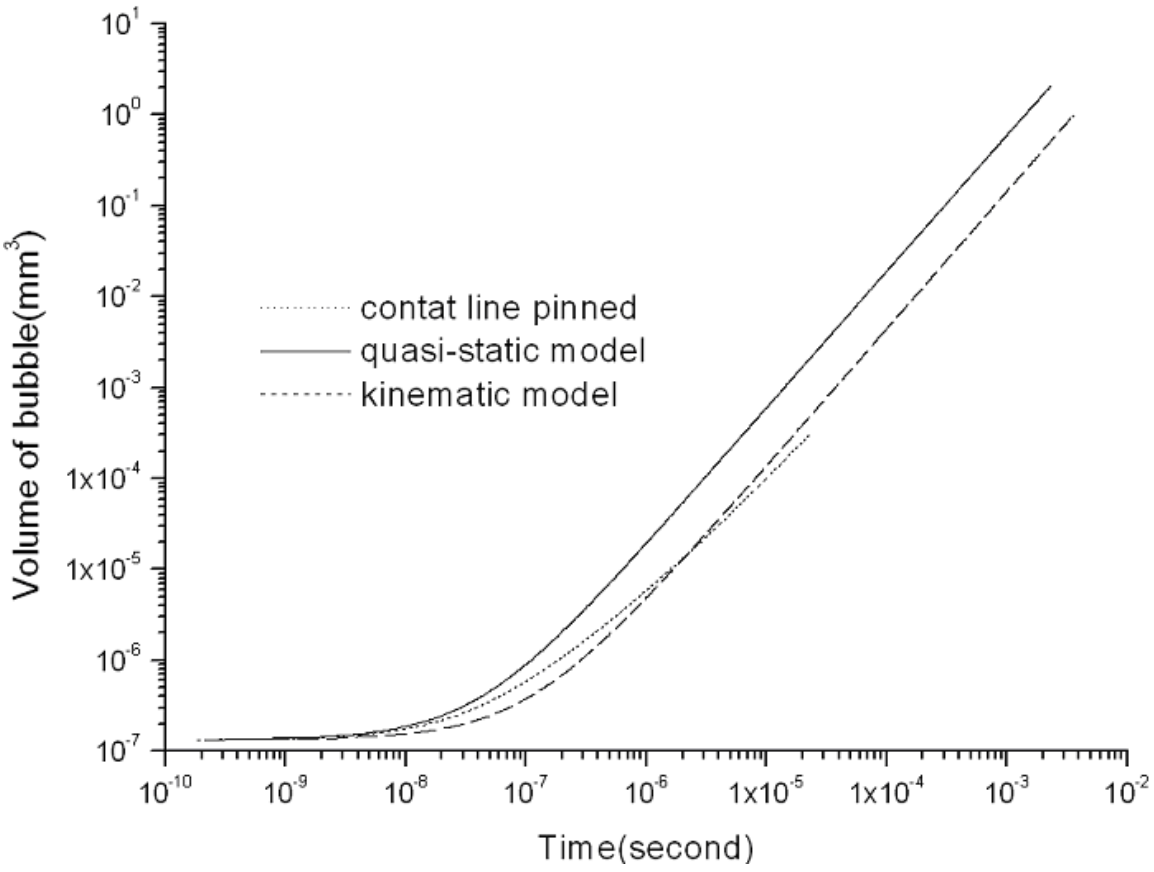

Figure III.6 Effect of conductivity ratio on bubble growth - CL pinned ($\varphi_i = 90^o$, $T_w - T_{sat} = 10K$, $R_{CL} = 4\mu m$)

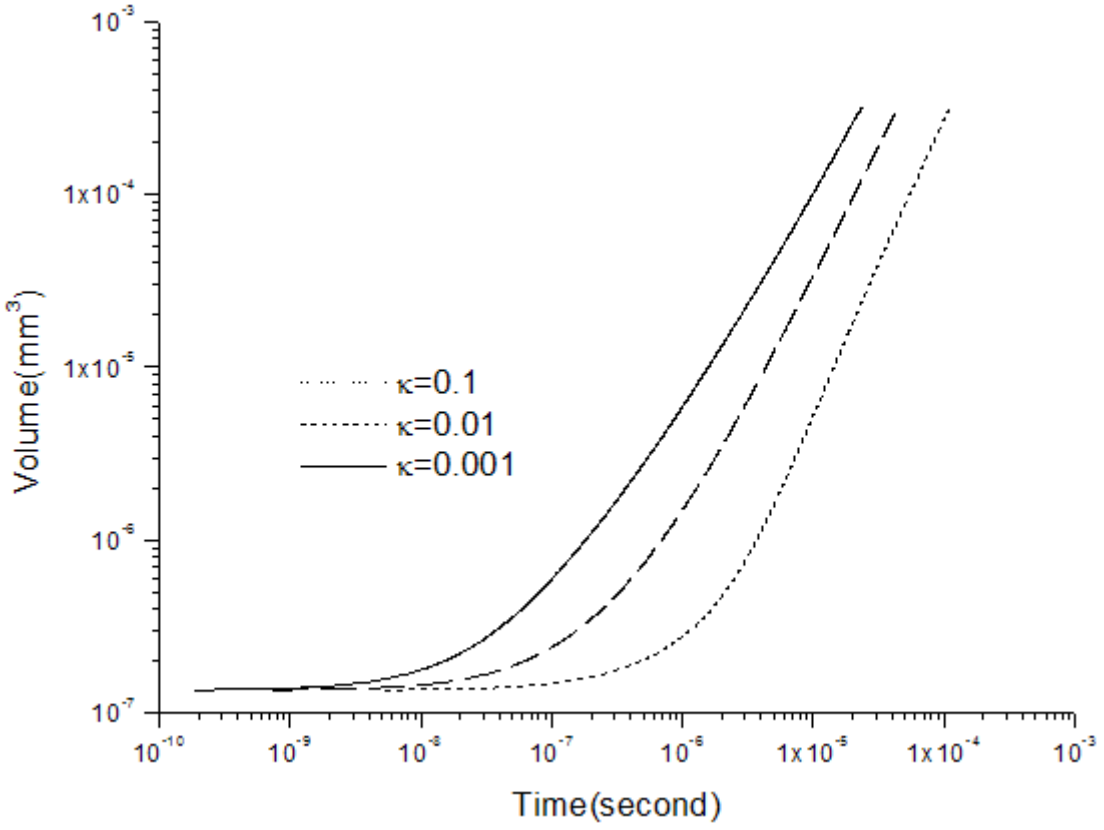

Figure III.7 Effect of wall superheat on bubble growth - CL pinned
(φ_i=90°, κ=0.001, R_{CL}=4μm)

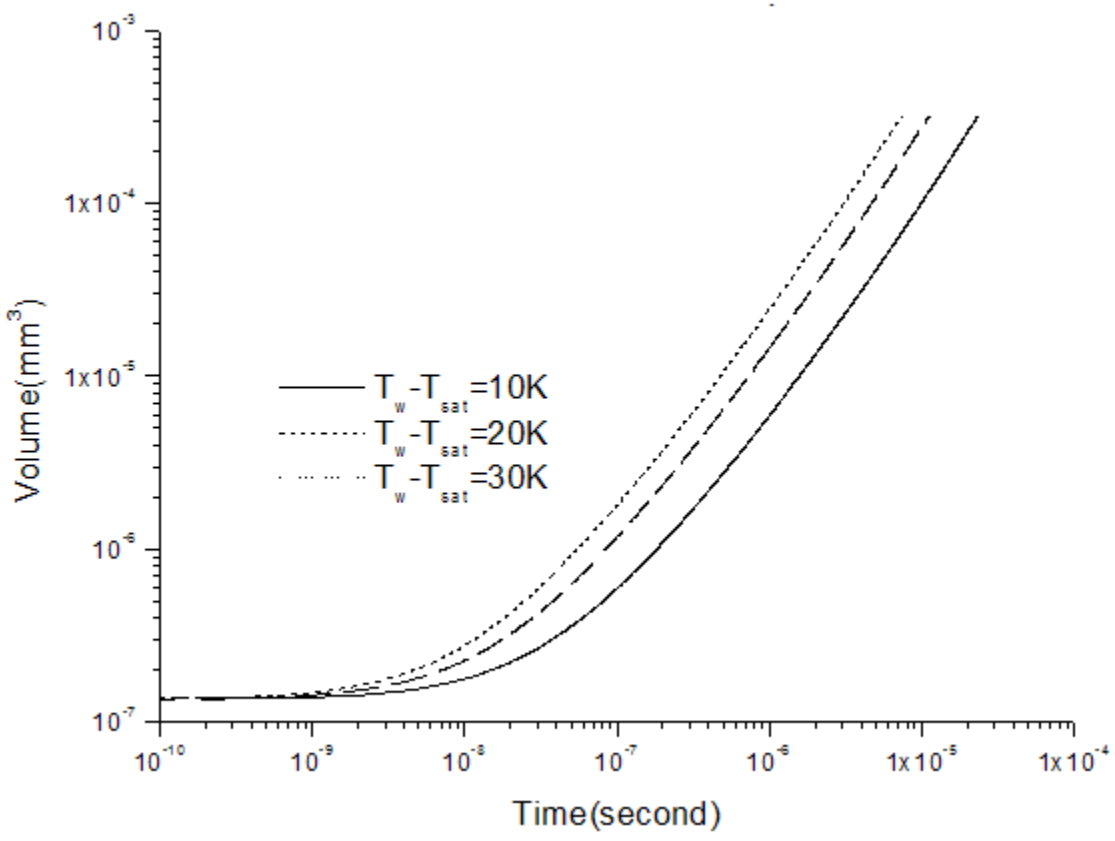

Figure III.8 Bubble growth on a clean copper surface (experiments done by Nonn Jr)

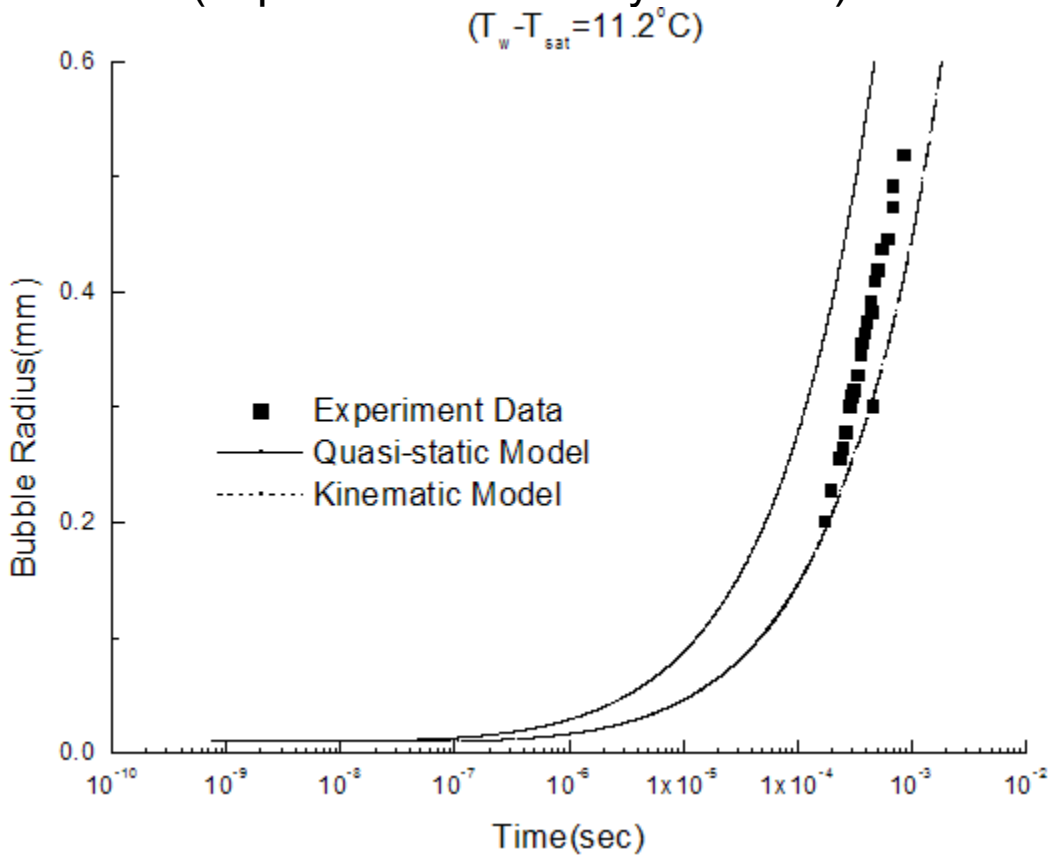

Figure III.9 Bubble growth on a clean copper surface (experiments done by Nonn Jr)

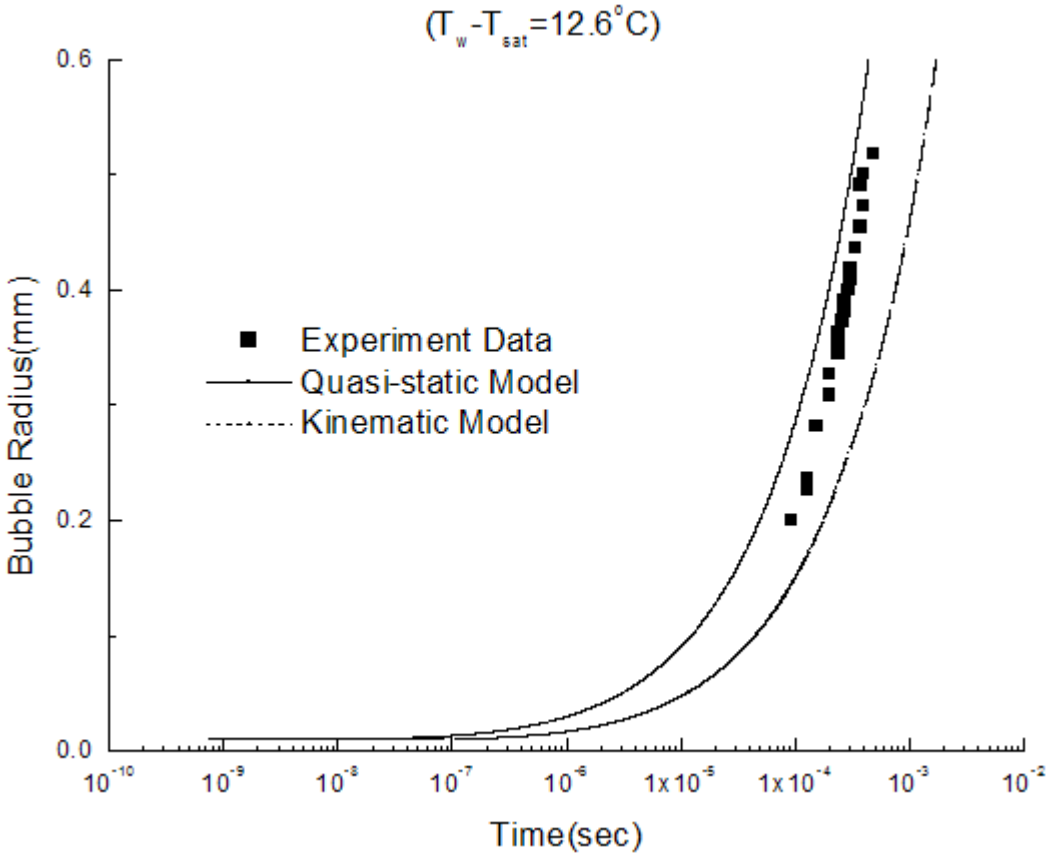

Figure III.10 Global Reynolds number evolution on CL motion models
(κ=0.001,φ_i =90^o, T_w-T_{sat} =10K)

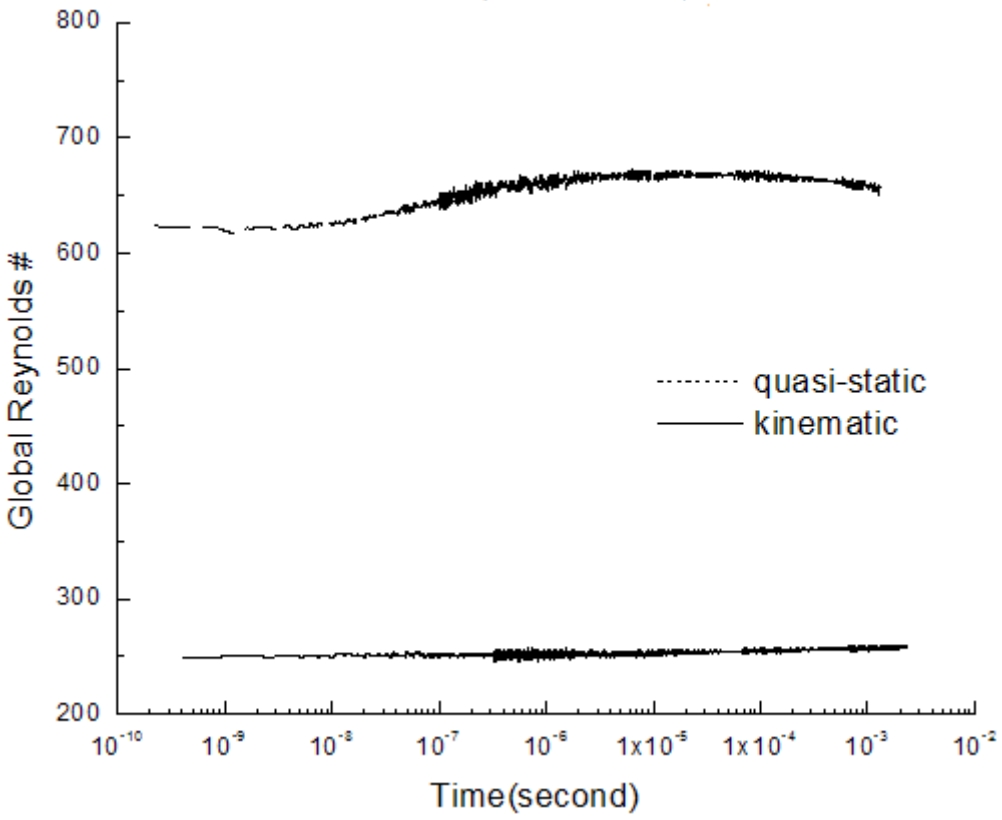

Figure III.11 Local Reynolds number evolution on CL motion models
(κ=0.001,φ_i =90^o, T_w-T_{sat} =10K)

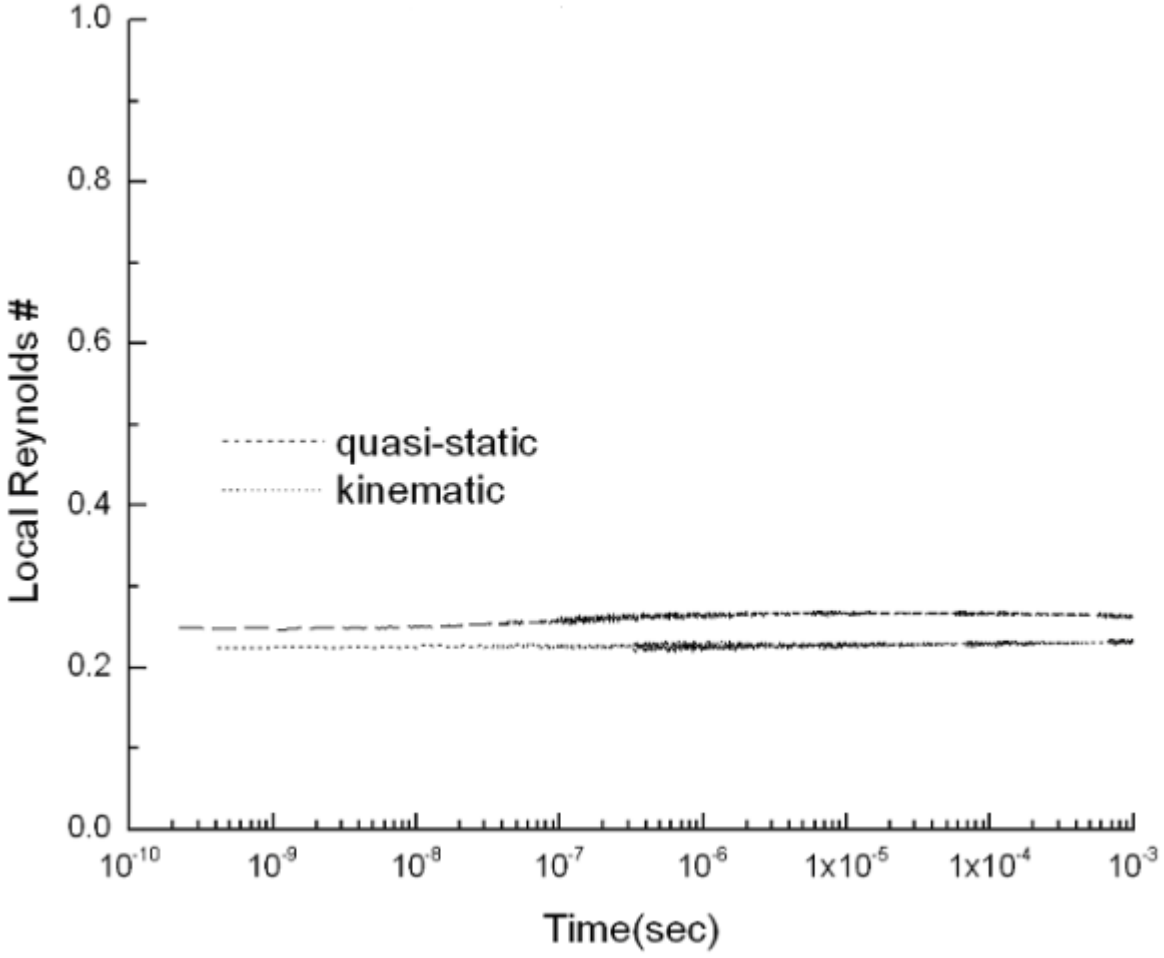

Figure III.12 Capillary number evolution on CL motion models
(κ=0.001,φ_i =90^o, T_w-T_{sat} =10K)

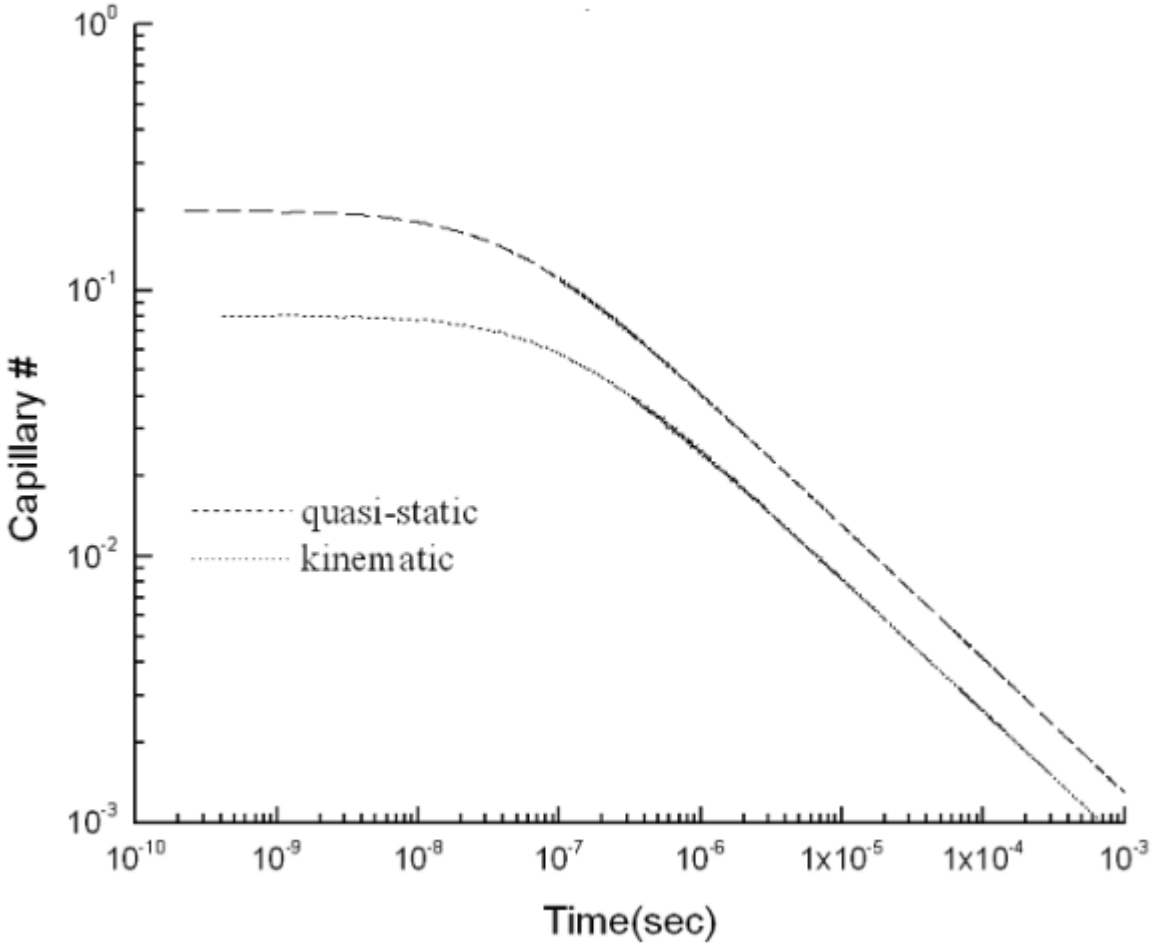

Figure III.13 Effects of system parameters on bubble growth - quasistatic CL

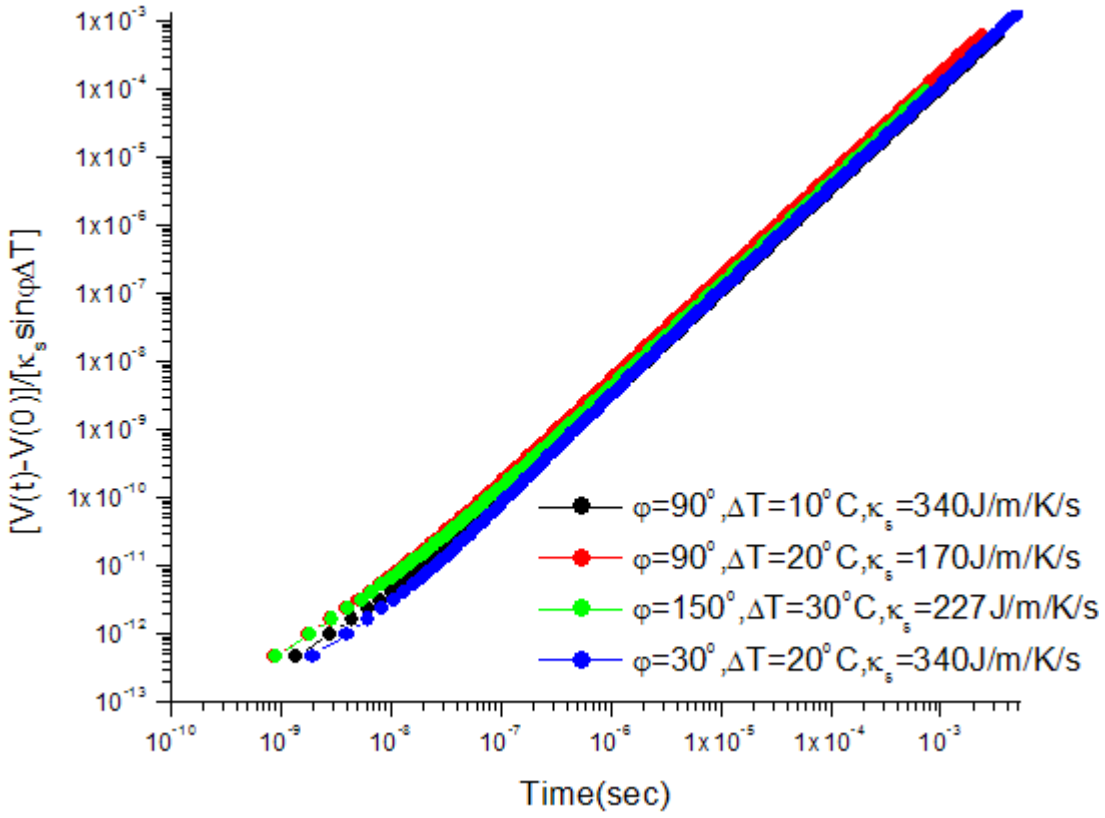

Figure III.14 Contact angle variation evolution on different initial contact angle – kinematic CL (κ=0.001, T_w-T_{sat} =10K)

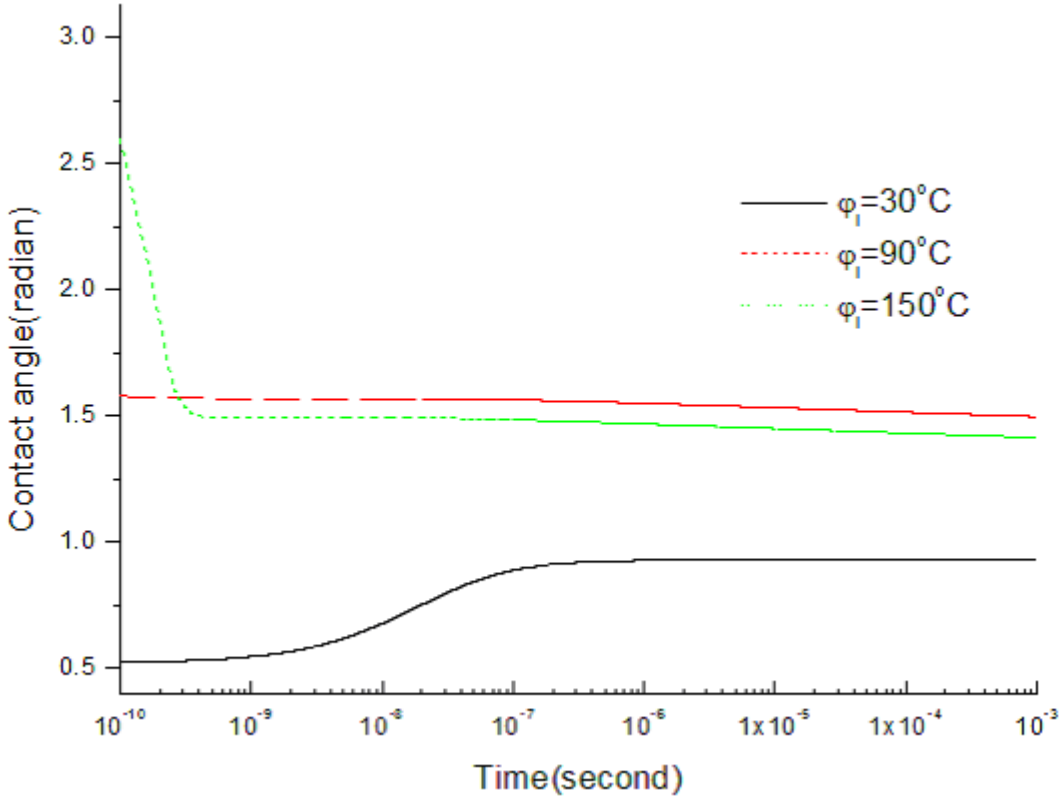

Figure III.15 Effects of system parameters on bubble growth - kinematic CL

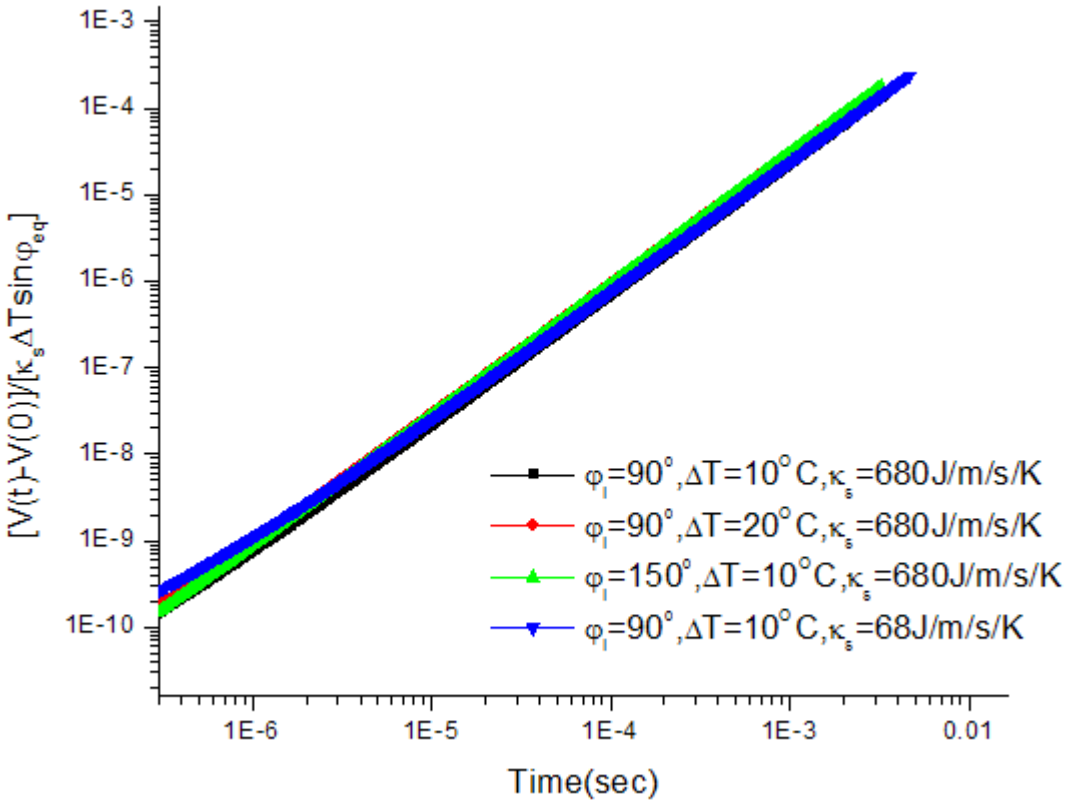

Figure III.16 Radius of CL Vs radius of vapor bubble - kinematic CL
(κ=0.001, T_w-T_{sat} =10K)

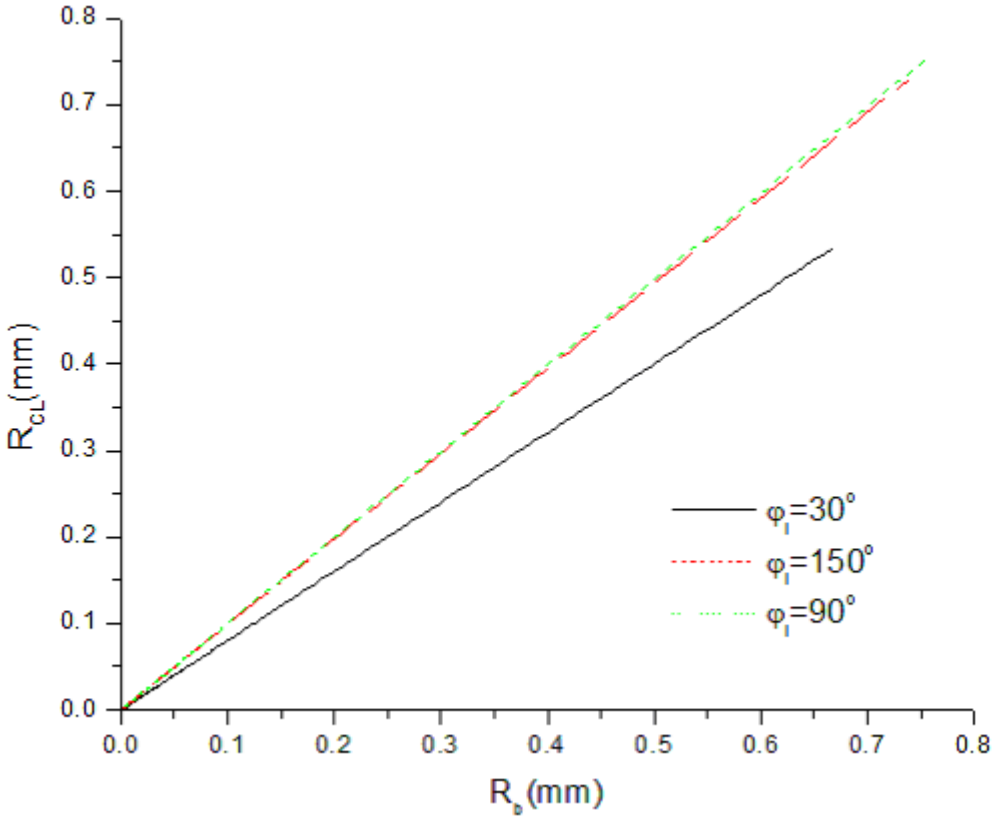

Figure III.17 Scheme of Young-Laplace (equilibrium) shape

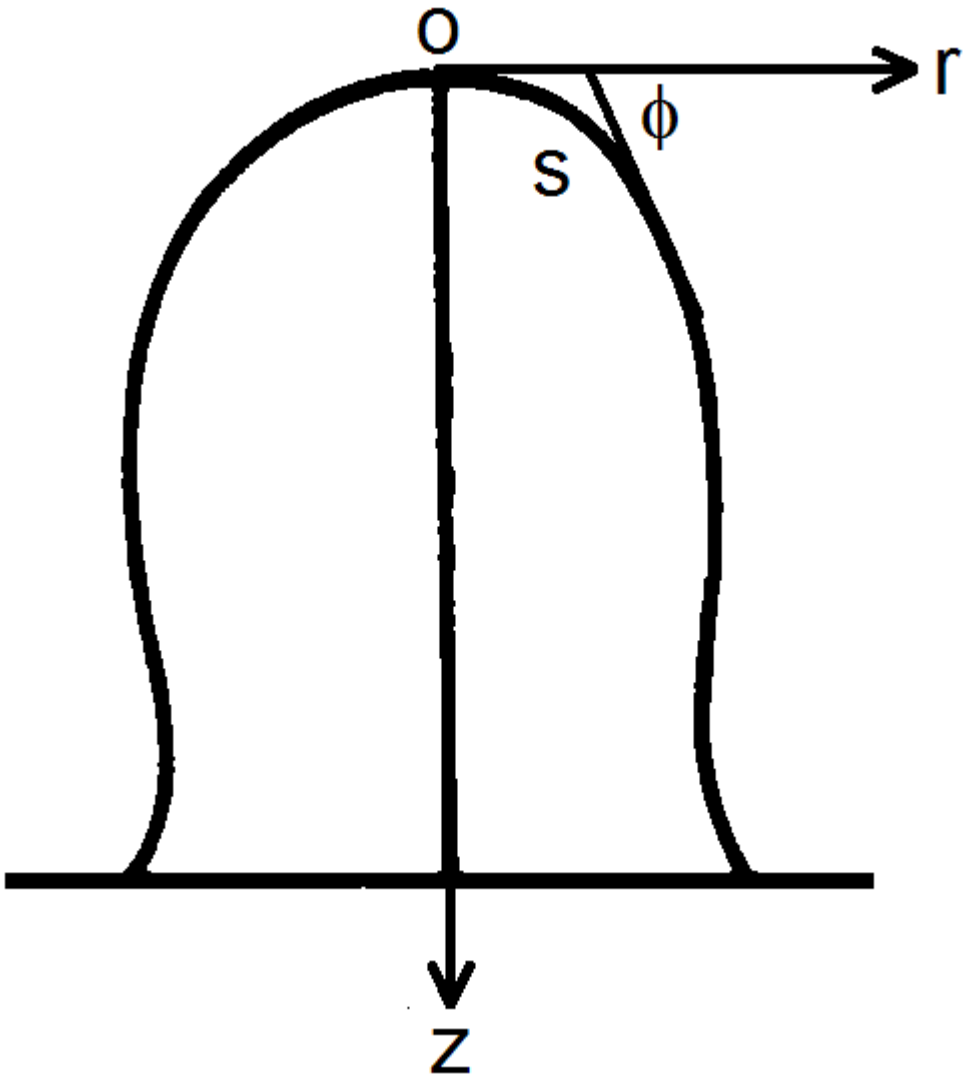

Figure III.18 Bubble growth and detachment in different CL motion models
(κ=0.001,φ_i =90^o, T_w-T_{sat} =10K)

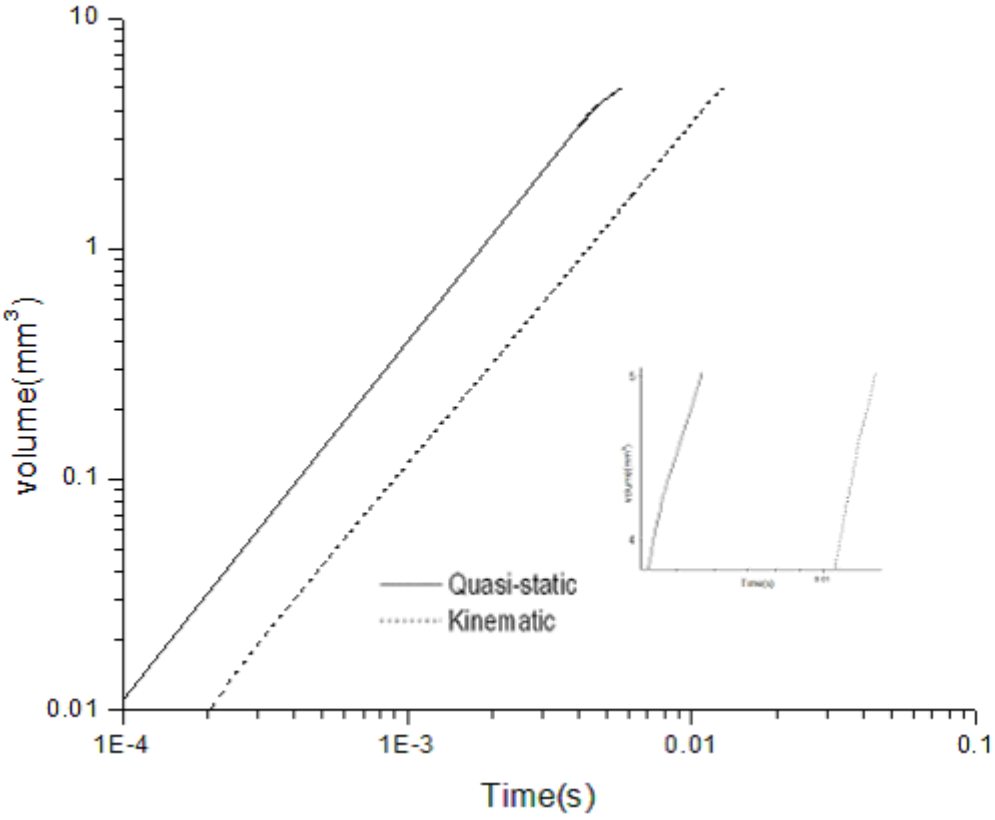

Figure III.19 Radius of CL Vs time in different CL motion models
(κ=0.001,φ_i =90^o, T_w-T_{sat} =10K)

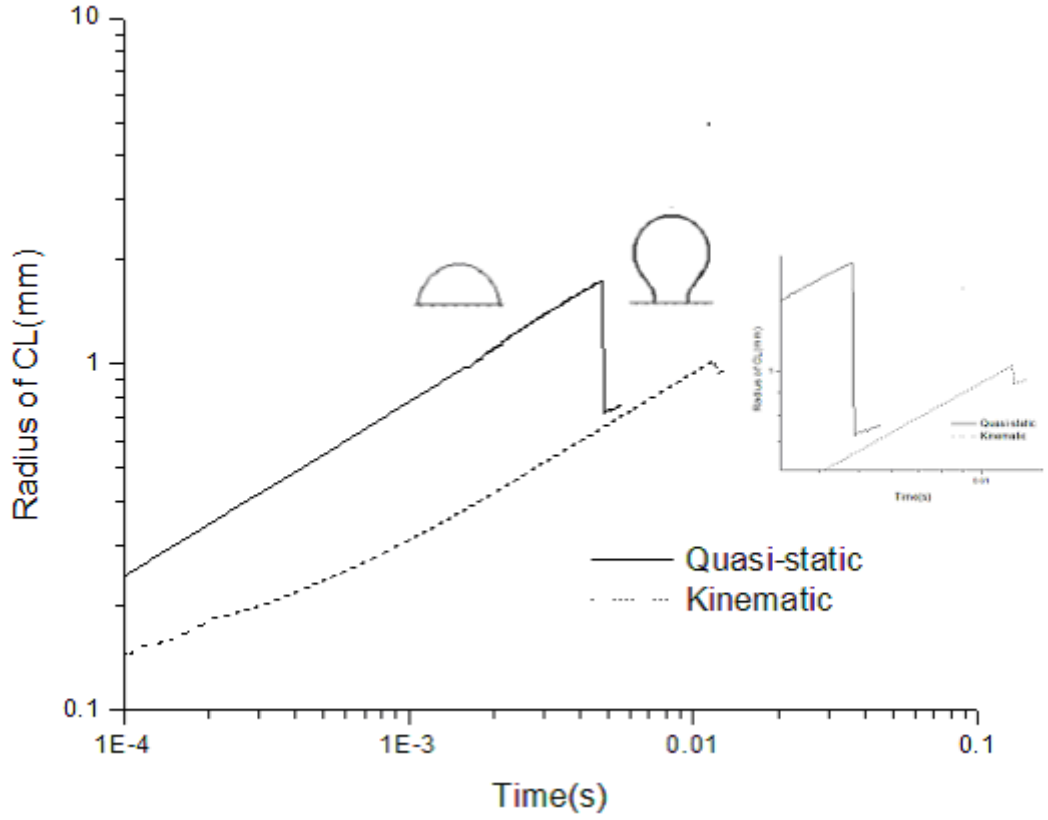

Figure III.20 ΔP at bubble apex Vs bubble volume (κ=0.001,φ_i =90^o, T_w-T_{sat} =10K)

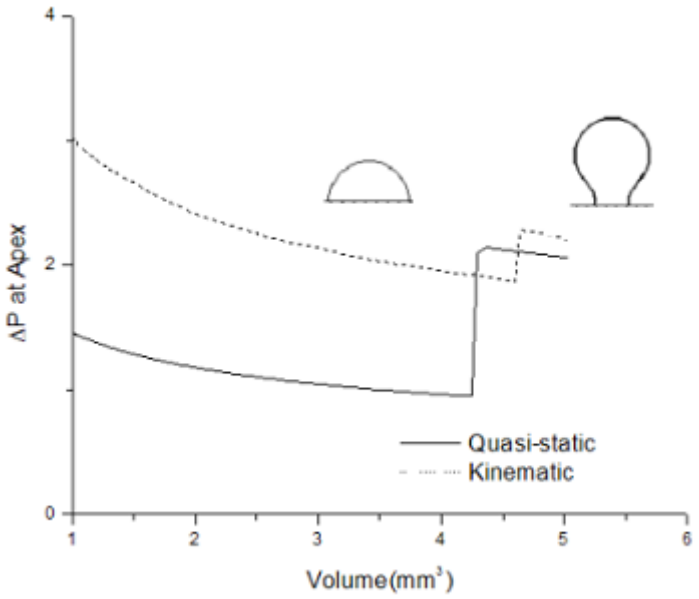

Table III.1 Effects of different parameters on vapor bubble growth for κ=0.001

	Power Dependence on time (before deform)	Power Dependence on time (after deform)
Wall Superheat (^{o}C)		
10[Kinematic CL]	1.51	1.239
20[Kinematic CL]	1.50	1.242
Initial Contact Angle(^{o})		
90[Kinematic CL]	1.51	1.239
130[Kinematic CL]	1.49	1.241
90[Quasistatic CL]	1.50	1.105
130[Quasistaic CL]	1.50	1.003
CL Motion		
Kinematic [φ_i 90^{o}]	1.51	1.239
Quasistaic [φ_i 90^{o}]	1.50	1.105

Figure III.21 Vapor bubble detachment in different CL motion models

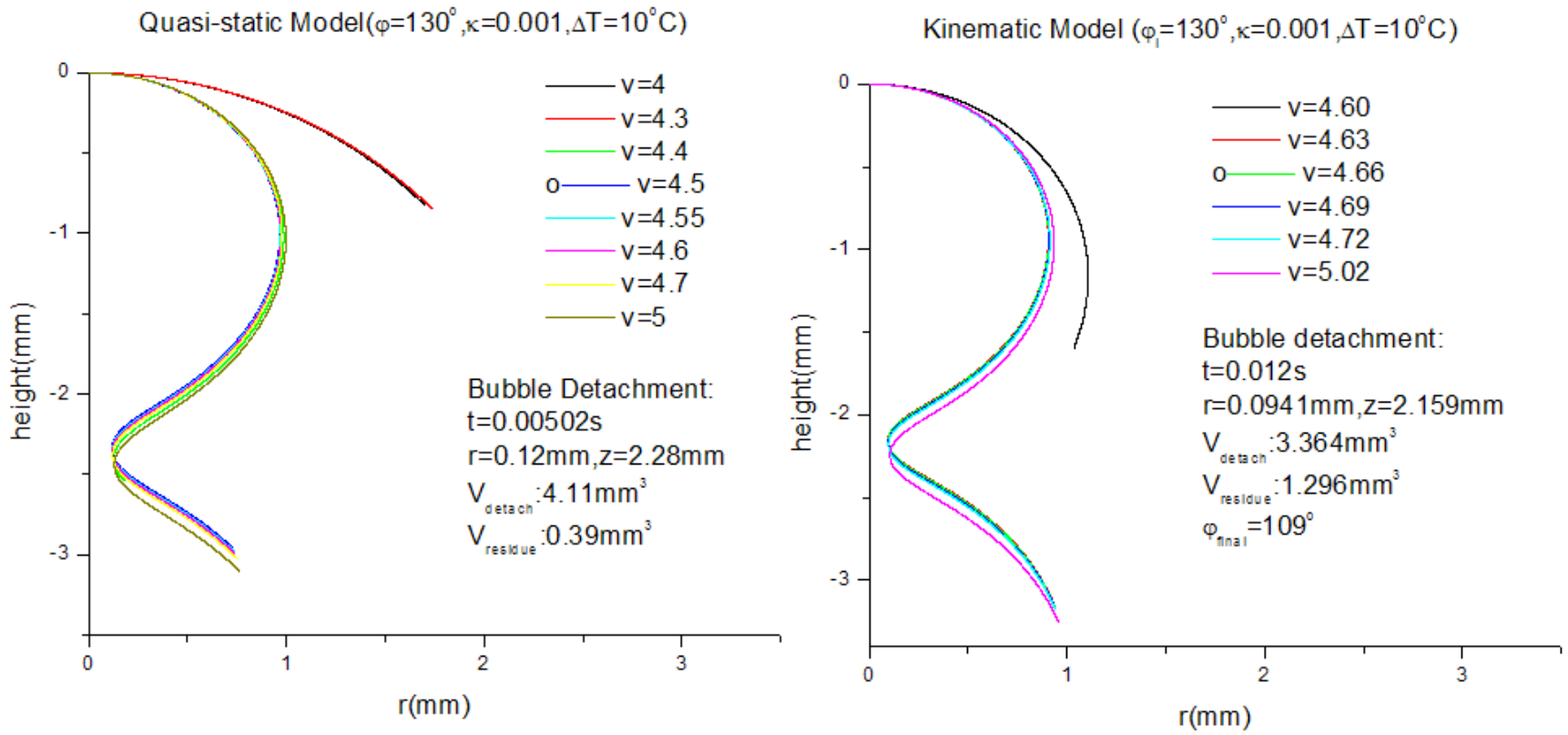

Figure III.22 Diameter of CL Vs Diameter of vapor bubble
(Experiments done by S. Gong and W. Ma)

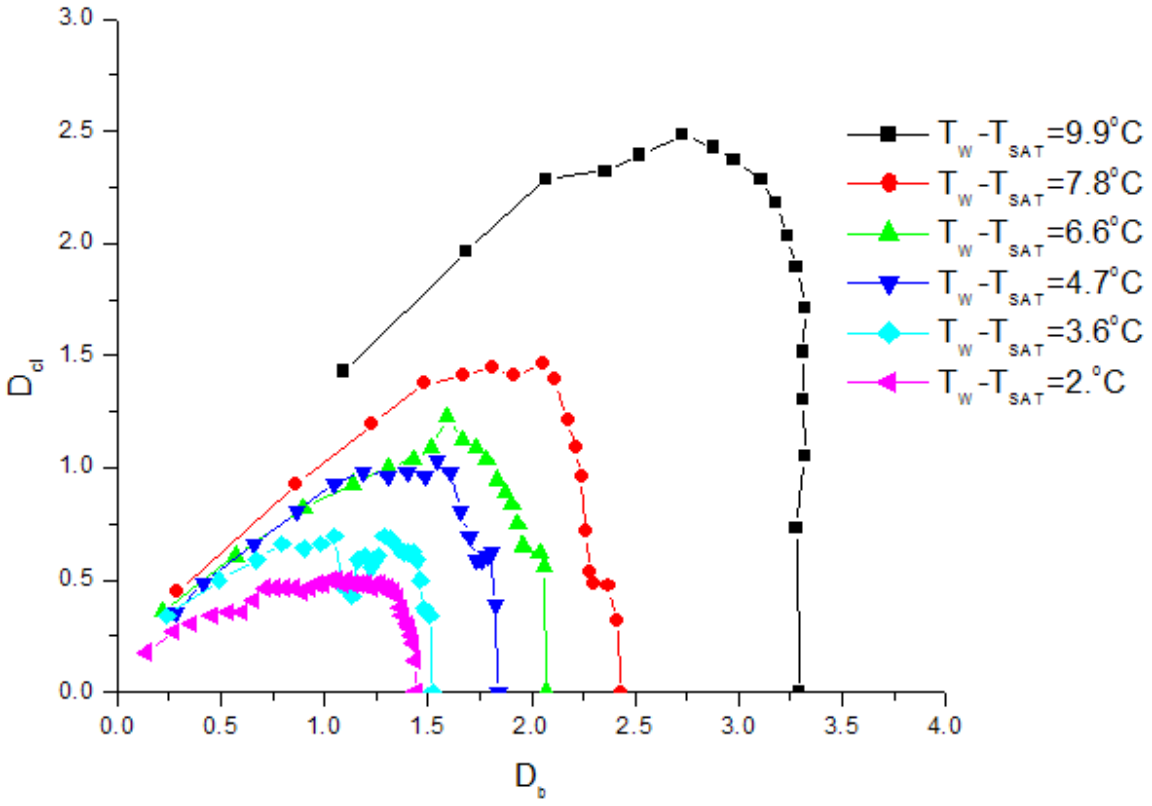

Figure III.23 Vapor bubble growth until its detachment from experimental CL

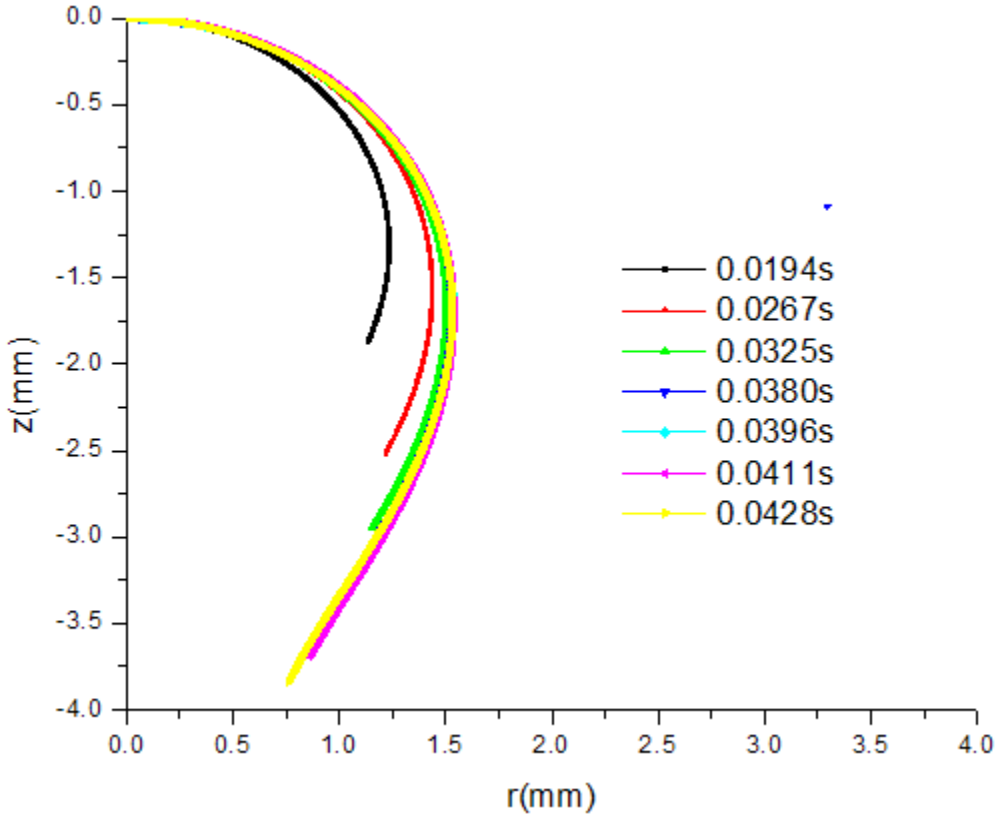

Figure III.24 Comparison of simulation of vapor bubble growth with experiment

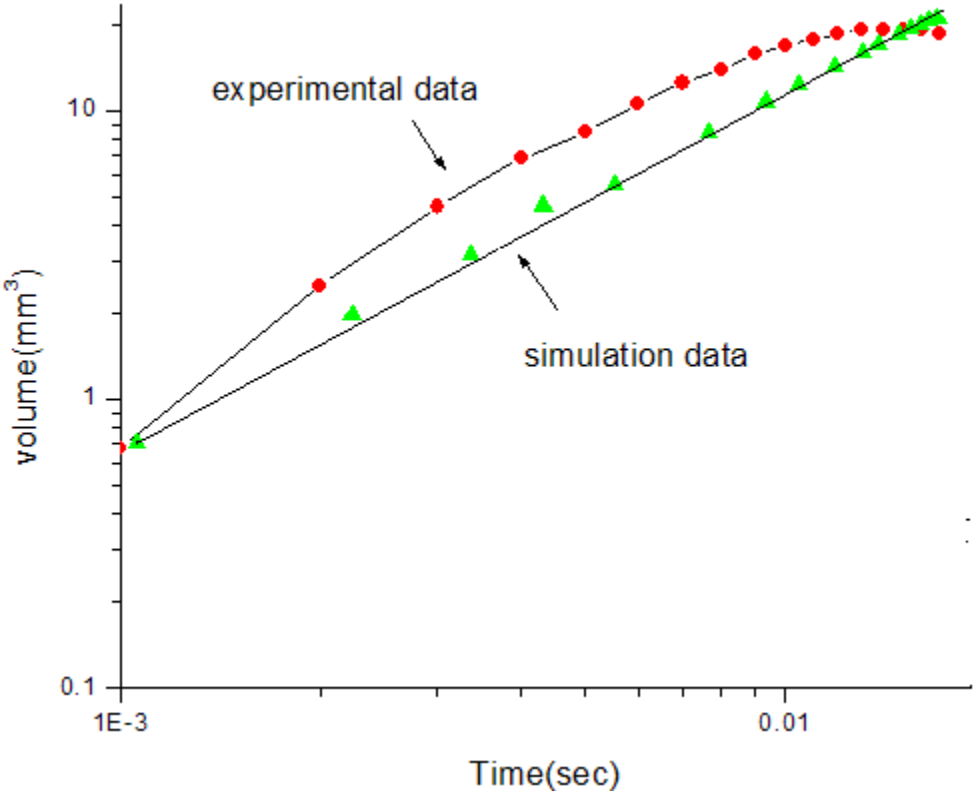

Figure III.25 Comparison of simulation of radius of CL evolution with experiment

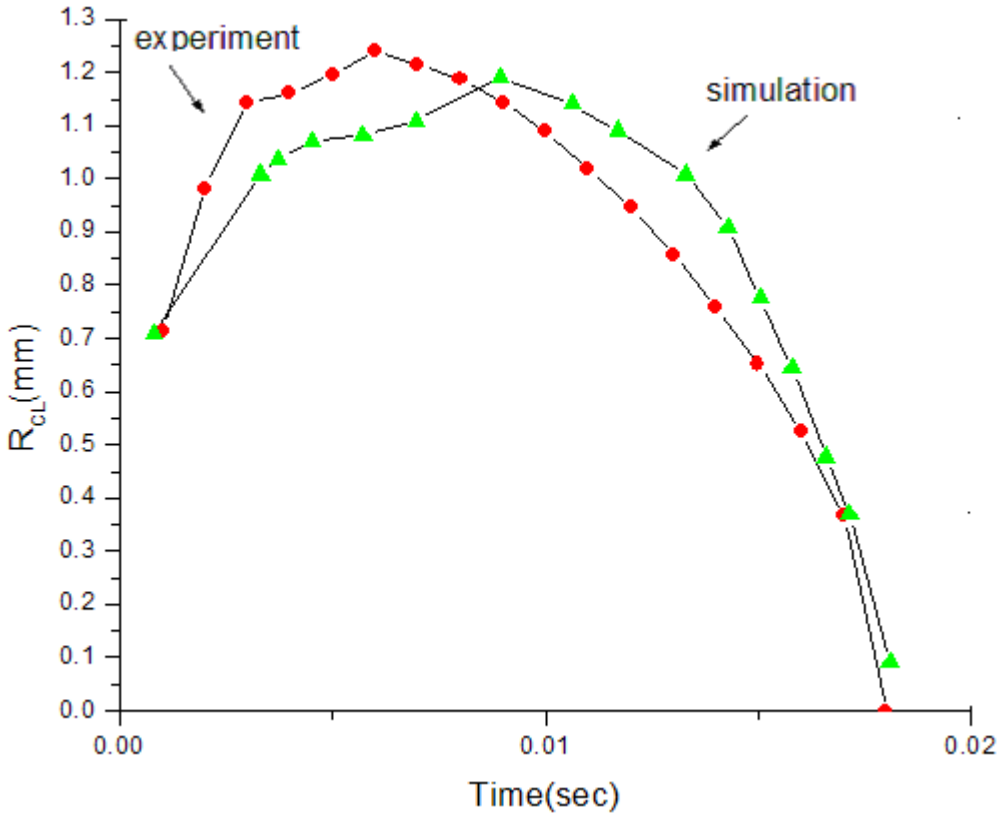

Chapter IV

Molecular Dynamics Simulation of Stable Vapor Bubble Growth

IV.1 Introduction of Molecular Dynamics Method

Molecular simulation is a computer simulation to study system of molecules, thus it can relate microscopic properties to macroscopic properties, more importantly it can be applied to nano-size system directly. There are two main techniques of such simulations: Molecular Dynamics (MD) and Monte Carlo (MC). The obvious advantage of MD over MC is that it is a deterministic technique; it thus gives us a route to calculate dynamic properties of the system that is out of its equilibrium state. Its main disadvantage is that it is computationally expensive. The basic idea of MD is as follows: Beginning with a specification of the various interaction potential energies, one can easily calculate the total forces on each atom. The classical equations of motion (Newton's laws) then determine the acceleration, the velocity and the position of each atom. By solving these equations for a large number of particles and performing appropriate temporal and spatial averaging, we can obtain the properties and behavior of larger-scale of interest.

Michael P. Allen's *Introduction to Molecular Dynamics*[84] provides a concise, lucid exposition for the basic method and we follow his development. MD simulation involves numerical integration of the classical equations of motion step by step, which is written as:

$$m_i \ddot{r}_i = f_i = -\frac{\partial}{\partial r_i} U_i \qquad \text{(IV.1)}$$

Therefore one needs to know potential energy $U(r^N)$ so as to calculate the forces f_i acting on the each atom, where $r^N = (r_1, r_2 \ldots\ldots r_N)$ represents the complete set of 3N atomic coordinates for the N-particle system being simulated.

IV.1.1 Molecular Interactions

The potential energy $U_{non\text{-}bond}$, which represents the non-bonded interactions among atoms, is traditionally be approximated by Lennard-Jones (LJ 12-6) potential

$$U_{non-bound}(r^N) = v^{LJ}(r) = 4\varepsilon\left[\left(\frac{\sigma}{r}\right)^{12} - \left(\frac{\sigma}{r}\right)^{6}\right] \qquad \text{(IV.2)}$$

where σ is the atomic radius, and ε the depth of the potential well. Generally a cutoff radius r_c (2.5σ for our MD simulations) is used to speed up the calculation so that atom pairs whose distances are equal to and greater than r_c are assigned a zero interaction energy. To make both the potential and the force continuous at r_c, the LJ potential, v^{LJ}, must be shifted so that the truncated potential would be zero exactly at the cut-off radius. The shifted LJ potential v^{LJ}_{trunc} is defined as follows:

$$v^{LJ}_{shift}(r) = v^{LJ}(r) - v^{LJ}(r_c) - \frac{dv^{LJ}}{dr}(r - r_c) \quad \text{for} \quad r > r_c \tag{IV.3}$$

In contrast to atoms, molecules need an additional interaction to bind the atoms together. There are some commercial simulation packages to represent different forms for different molecules and calculate the bond energy based on their functional forms. For simplicity, Finitely extensible non-linear elastic (FENE) potential between beads are applied for polymers by modeling each polymer as a simple chain of beads. It is written as:

$$v^{FENE} = -\frac{k}{2}\ln(1 - \frac{r^2}{r_0^2}) \tag{IV.4}$$

In our simulation, we are interested in understanding of the behavior of the contact line as the vapor bubble grows, for simplicity, Argon atom is used as simulation fluid and the potential between them is simply represented by shifted LJ potential.

IV.1.2 Force Evaluation

When evaluating the force exerted on any one atom by all of the other atoms by using equation IV.1 with shifted LJ potential, the computation time is clearly $O(N^2)$, which is the most expensive part of MD simulations. However, in practice the local neighbors of a given atom remain the same for hundred of femto-seconds. In our MD simulation, a time step is set to 5 femto-seconds, thus, these neighboring atoms will stay close to a given atom during 20 time steps. Verlet[85] constructs a list to maintain a list of neighbor between the distance of r_m ($r_m > r_c$, it is also refers to skin thickness and usually sets it to 3.5σ). We use this technique and update this list every 20 steps so as to avoid atoms travel more than skin thickness. The "Verlet list" remains $O(N^2)$ but decreases the calculation of forces by a factor of update time intervals. Using a cellular division of the

simulation cell and a linked list, one truly obtain O(N) algorithm. By dividing the MD simulation domain into smaller cells and choosing the size of one cell greater than skin thickness, one only need to search the atoms in the same cell as the atom of interest and other 26 closest neighbor cells when calculating the total force acting on an atom of interest. The cell structure can be set up and used by the method of linked lists[86]. This method is employed on Our MD simulation to compute the forces.

IV.1.3 Periodic Boundary Condition

Periodic boundary condition at the boundaries of simulated system is usually used because no matter how large the simulated system is, its number *N* of atoms would be negligible compared with the number ($O(10^{23})$) of atoms contained in a macroscopic piece of matter, as a result the ratio between the number of surface atoms and the total number of atoms would be much larger than in reality. This would cause the calculated surface effects to be much more important than they are in real systems. We can assume that each atom interacts with the nearest atoms or image atoms in the periodic array. If an atom leaves the basic simulation box during the simulation, attention will be switched to the incoming image.

IV.1.4 Integration Algorithm

Frenkel's textbook[87] summarizes the present states such as the Verlet algorithm, the velocity Verlet algorithm and the leap-frog algorithm. Predictor-corrector algorithm that is based on Taylor expansion is used to integrate a set of equations of motion in our simulation. The details are as following: If the position *r*, velocity *v*, acceleration *a* and time derivative of the acceleration b of the atoms are known at time *t*, these quantities after time step Δt can be predicted as shown in the following equation:

$$\begin{aligned} r(t+\Delta t) &= r(t) + v(t)\cdot\Delta t + \frac{1}{2}a(t)\cdot(\Delta t)^2 + \frac{1}{6}b(t)\cdot(\Delta t)^3 + ... \\ v(t+\Delta t) &= v(t) + a(t)\cdot\Delta t + \frac{1}{2}b(t)\cdot(\Delta t)^2 + ... \\ a(t+\Delta t) &= a(t) + b(t)\cdot\Delta t + ... \\ b(t+\Delta t) &= b(t) + ... \end{aligned} \qquad \text{(IV.5)}$$

The quantities calculated from Equation IV.5 at t+Δt can be called the predicted values r^p, v^p, a^p, and b^p. The force will be calculated from Equation IV.1 at r^p. After obtaining the force, one can re-calculated the correct acceleration a at t+Δt (corrected

value with superscript c) by $a^c(t+\Delta t) = f(r,t)/m$, where f(r,t) is the total force exerted on the atom of interest and m is the atom mass. Clearly a^c is different from the predicted acceleration a^p, and the difference is called the error signal, as shown in Equation IV.6:

$$\Delta a(t+\Delta t) = a^c(t+\Delta t) - a^p(t+\Delta t) \tag{IV.6}$$

This term for the error signal is used to correct all the predicted quantities as follows:

$$\begin{aligned} r^c(t+\Delta t) &= r^p(t+\Delta t) + c_0 \Delta a(t+\Delta t) \\ v^c(t+\Delta t) &= v^p(t+\Delta t) + c_1 \Delta a(t+\Delta t) \\ a^c(t+\Delta t) &= a^p(t+\Delta t) + c_2 \Delta a(t+\Delta t) \\ b^c(t+\Delta t) &= b^p(t+\Delta t) + c_3 \Delta a(t+\Delta t) \end{aligned} \tag{IV.7}$$

All the "magic number" from c_0 to c_3 can be determined by maximize the stability of the calculation; the method is very detailed and left to the reference[88]. Normally they can be found in textbook[87,88]. The algorithm shown here is a third-order algorithm. Due to the truncation of the Taylor expansion and the round-off errors caused by computer, the order of this algorithm needs to be carefully chosen to balance accuracy and computational speed. A fifth-order algorithm is used in our simulations and these coefficient values from c_0 to c_5 are 3/16, 251/360, 11/18, 1/6 and 1/60 respectively[87].

IV.1.5 Reduced Units

Physical quantities in molecular dynamics simulations are expressed in reduced units because instead of working with the extremely large or small numbers, this places all quantities at around the same order, which reduces the error. Furthermore, by working in reduced units, one can use a single model to study different problems.

The following basic units are used for a system with LJ potential: length σ, energy ε and mass m. With the replacement of $r^* = r/\sigma$ and $v^* = v/\varepsilon$, the LJ potential becomes

$$v_{LJ}^*(r^*) = 4[(r^*)^{-12} - (r^*)^{-6})] \tag{IV.8}$$

Other reduced quantities are time $t^* = t\sqrt{\frac{\varepsilon}{m\cdot\sigma^2}}$, pressure $P^* = P\cdot\frac{\sigma^3}{\varepsilon}$, temperature $T^* = {k_b T}/{\varepsilon}$ and density $\rho^* = \rho\cdot\sigma^3$.

IV.1.6 Microscopic Representation of the Properties of Fluid Mechanics

In MD simulations, we are interested in macroscopic quantities such as the local density, temperature and stress tensor. Here we define the microscopic expressions for

these quantities. If the mass of the individual atoms in our system is m_i, then the mass per unit volume at a position r and time t can be obtained by taking an appropriate ensemble average (<>) over the normalized N-particle distribution function $f(r^N, p^N, t)$.To specify that particle i is at the position r_i, we will use a delta function, $\delta(r-r_i)$. Ensemble averaging is almost never used because it is relatively expensive in computer time. We assume that the ergodic hypothesis is valid, i.e., that the result obtained by ensemble averaging is equal to that obtained by time averaging the same property. This allows us to develop expressions for some macroscopic quantities without computing ensemble averages. Below, we write microscopic exact expressions involving ensemble averages, but compute them by instead averaging a simulation over a suitably long simulation time. The mass density ρ(r,t) can be calculated from:

$$\rho(r,t) = \left\langle \sum_i m_i \delta(r - r_i(t)) \right\rangle \tag{IV.9}$$

There is a convenient definition of the temperature by using of the equi-partition of energy over all degrees of freedom. In particular for the average kinetic energy per degree of freedom, we have the following formula to calculate temperature

$$\left\langle \frac{1}{2} m v^2 \right\rangle = \frac{1}{2} k_b T \,. \tag{IV.10}$$

To calculate the stress tensor, we follow the method presented in D. Frenkel's textbook[87] and the class notes (Molecular Simulations, CHE 57580, City College, Spring 2007) of Professor J.Koplik and start from the continuum mass continuity equation

$$\frac{\partial \rho(r,t)}{\partial t} = -\nabla \cdot \left[\rho(r,t) u(r,t) \right] \tag{IV.11}$$

Substituting equation IV.9 into the left-hand side of equation IV.11 gives:

$$\frac{\partial \rho(r,t)}{\partial t} = \sum_i m_i \frac{\partial r_i}{\partial t} \frac{\partial}{\partial r_i} \delta(r - r_i(t)) = -\frac{\partial}{\partial r} \sum_i m_i \dot{r}_i \delta(r - r_i(t)) \tag{IV.12}$$

after comparing with the right-hand side of equation IV.11, we obtain the instantaneous momentum density J(r,t) is:

$$\rho(r,t) u(r,t) = J(r,t) = \sum_i m_i \dot{r}_i \delta(r - r_i(t)) \tag{IV.13}$$

Laboratory velocity of each atom can be divided into 2 parts: a thermal part v_i (the random part of the laboratory velocity) and a streaming part $u(r_i,t)$ (the non-zero mean value of the laboratory velocity in the control volume). Using this decomposition and differentiating the instantaneous momentum density, we obtain:

$$\frac{\partial}{\partial t}[\rho(r,t)u(r,t)] = \frac{\partial}{\partial t}\sum_i m_i \dot{r}_i \delta(r-r_i) = m_i \ddot{r}_i \delta(r-r_i) - \sum_i m_i \dot{r}_i \dot{r}_i \frac{\partial}{\partial r}\delta(r-r_i) \qquad \text{(IV.14)}$$

and the first term of equation IV.14 is

$$\begin{aligned} m_i \ddot{r}_i \delta(r-r_i) &= \sum_{i\neq j} f_{ij} = \sum_{i\neq j} f_{ij}\delta(r-r_i) = \frac{1}{2}\sum_{i\neq j}[f_{ij}\delta(r-r_i) + f_{ji}\delta(r-r_j)] \\ &= \frac{1}{2}\sum_{i\neq j} f_{ij}[(\delta(r-r_i) - \delta(r-r_j)] \end{aligned} \qquad \text{(IV.15)}$$

Let $r_{ij} = r_i - r_j$ and use the Taylor expansion of $\delta(r-r_j)$ as follows:

$$\delta(r-r_j) = \delta(r-r_i) + r_{ij}\frac{\partial}{\partial r}\delta(r-r_i) + ... \qquad \text{(IV.16)}$$

Substituting equation IV.16 into IV.15, we obtain:

$$m_i \ddot{r}_i \delta(r-r_i) = \frac{1}{2}\sum_{i\neq j} f_{ij} r_{ij} \frac{\partial}{\partial r}\delta(r-r_i) \qquad \text{(IV.17)}$$

the second term of equation IV.14 can be simplified to

$$\begin{aligned} \sum_i m_i \dot{r}_i \dot{r}_i \delta(r-r_i) &= \sum_i m_i (v_i + u(r_i,t)(v_i + u(r_i,t)\delta(r-r_i) \\ &= \sum_i m_i v_i v_i \delta(r-r_i) + \rho(r,t)u(r,t)u(r,t) \end{aligned} \qquad \text{(IV.18)}$$

As we know, momentum continuity equation in continuum:

$$\frac{\partial}{\partial t}[\rho(r,t)u(r,t)] = -\nabla\cdot[\rho(r,t)u(r,t)u(r,t) + P] \qquad \text{(IV.19)}$$

After we substituting equation IV.17 and IV.18 into equation IV.14 and comparing that with equation IV.19, the expression for pressure/stress tensor is obtained:

$$P(r,t) = \sum_i m_i v_i v_i \delta(r-r_i) - \frac{1}{2}\sum_{i\neq j} f_{ij} r_{ij} \frac{\partial}{\partial r}\delta(r-r_i) \qquad \text{(IV.20)}$$

These expressions build a bridge between hydrodynamic macroscopic properties and microscopic quantities.

IV.2 MD Setup for the Problem of Heterogeneous Nucleation and Vapor Bubble Growth

We construct a nanometer-scale, three-dimensional experiment that includes the solid-liquid and solid-vapor interfaces as well as the thermodynamic liquid-vapor interface. We consider two methods to implement this experiment: one is a constant volume MD experiment; the other is a constant pressure MD experiment.

In the constant volume MD experiment, the simulation domain of interest is a cuboid that is composed of two regions: the solid wall and the ”fluid” region. The solid wall lying at the bottom of simulation domain is represented by four layers of atoms that are tethered to their lattice position by harmonic force. The forces between atoms, harmonic around their equilibrium separations in the Born-Oppenheim approximation, push the solid atoms around as they thermalize. The upper boundary of the computation domain is an imaginary reflecting wall. The collision of an atom with this boundary is purely elastic. The distance from this wall to the solid surface below is selected to be large enough (the chosen distance is based on Yi et al's work[56] and on our trial-and-error calculations) so as not to affect the evaporation process. Periodic boundary conditions are applied at the other four lateral boundaries of the computation domain as described in IV.1.3. Right above the solid wall is the fluid region, which is fully occupied by argon molecules (liquid phase and vapor phase). The potential energy between a pair of argon atoms is described by equation IV.4 with parameter values σ=3.4A, $\varepsilon = 120k_b$. For the interactions between the solid and argon atoms, we employ the same equation but with different parameters, e.g., $\sigma=1/2(\sigma_{Pt}+\sigma_{Ar})$=3.085A. The choice of ε for these interactions is more delicate, because it is related to solid surface wettability[61]. This reference observes more wetting with increasing strength of the interaction potential between the solid and argon atoms. Therefore, if this ε is too large, i.e., if the interaction potential between solid and argon is too large, it will be very difficult to nucleate at vapor bubble. On the other hand, if this interaction potential is too low, the liquid and solid phases will hardly interact with one another and too little heat will be transferred to grow an already-nucleated vapor bubble. Since our goal is to track CL motion with vapor bubble growth, this situation is also inadequate. Thus we will need to experimentally tune the value of ε in order to be able to both nucleate and grow vapor bubble on the heated solid's surface.

In the constant pressure MD experiment, the simulation domain is again a cuboid, this time composed of the two solid walls and a fluid region (again of argon molecules)

sandwiched between these two walls (see Figure IV.1). The interaction potentials between a pair of argon atoms, and between solid and argon atoms, and the harmonic forces that tether the solid atoms to their lattice positions are identical to those in the constant volume simulation described above. We also retain the periodic boundary conditions on the four lateral boundaries. Some references[61,63,89], expand the top wall at constant temperature until the system achieves a negative pressure so as to nucleate a vapor bubble on the surface of bottom wall by cavitation. In contrast, to begin the experiment, we shall equilibrate the system at a uniform, fixed temperature below the fluid's saturation temperature and then gradually expand the top wall of the simulation domain until the system reaches a fixed positive pressure, as measured at the top wall. We shall then increase the temperature at the bottom layer of the solid to a value above the fluid's saturation temperature and allow heat conduction through the solid to nucleate vapor bubble at the solid-fluid interface. Before carrying out this numerical experiment, we will need to find an appropriate target positive pressure by trial and error. Once found, we will maintain that pressure afterward by moving the top solid wall up and down, as in a cylinder with a frictionless piston. We then expect to observe the growth of the nucleated vapor bubble by heat transfer and evaporation due to maintaining the temperature gradient between the two solid walls.

Before continuing to the simulation results, we describe the method by which we shall represent the simulation results. In our simulations, we use two methods to visualize the vapor bubble. One is to search "void points" in the liquid region (as Maruyama's group did[61]). Here one constructs a 3-dimension tiling of lattice size 0.5σ; one marks a tile as "void" if there are no molecules within 1 or 1.2σ of its center; otherwise it is occupied, i.e., liquid. The assembly of such voids represents the vapor bubble. A second method is to plot the 3D density contours and to define a threshold density value; we choose a threshold value for the local density as 0.15 to represent the liquid-vapor interface based on the M. Mecke's reference[90].

IV.3 The Constant Volume MD Experiment

The advantage of a constant volume MD experiment is that it is easier to set up and takes far less time to check the results because the top wall of simulation domain is simply an imaginary reflecting wall. We begin with a small simulation domain in order to

test different ε (e.g., ε= 0.3, 0.4, 0.5, 0.75) values between the solid and argon atoms to find an appropriate value to balance the heat transfer and vapor bubble nucleation. The size of this simulation domain is 21σx21σx37σ and it includes two regions: the solid wall that consists of 2888 solid atoms arranged in 4 layer (a spring constant set to $100\frac{\varepsilon}{\sigma^2}$ [91]) and a fluid region that includes 6760 argon atoms right above this solid wall. As an initial condition, all of the fluid atoms sit on their FCC crystal lattice positions. Recall in the microscopic representation of temperature discussed in IV.1.6, the constant temperature of the control unit means a constant total kinetic energy of all atoms in the control unit. Thus at every time step we rescale the velocity of each atom in the control unit by the factor of $\sqrt{\frac{\frac{3}{2}Nk_bT}{\sum_i \frac{1}{2}m_i v_i^2}}$; this technique is called velocity-scaling temperature control. We apply this technique directly to the solid and argon atoms for the initial 100,000 (100k) time steps at the reduced temperature T=0.75. Then we switch off the direct temperature control of the whole system and step change of temperature on the bottom layer of the solid wall to T=1.1 for another 400k time steps. We shall examine plots of the temperature, averaged over planes parallel to the solid-fluid interface, and also time averaged over 500 consecutive time steps, at different distances z=z*/σ from it within the simulation domain at different times.

Figure IV.2 shows these temperature profiles after we have begun thermostating the bottom of the solid to a temperature of T=1.1 for a value of ε_{sf}=0.3. For this case we find no temperature change with time in the fluid because the interaction potential parameter between solid and argon is so weak that the heat cannot transfer from solid to argon.

Figures IV.4, IV.6 and Figure IV.8 employ the "void" point visualization technique to try to see vapor bubble nucleation and growth for various larger values of ε_{sf} and Figures IV.3, IV.5 and IV.7 are the corresponding temperature profile plots. Notice in these temperature plots that beyond a height of z~22, the temperature curves fluctuate wildly. This is because, beyond this height, there are too few particles in each cross section to get reliable averages. Notice also that the increase in the temperature with

simulation time for all z where there is adequate density to obtain good temperatures evinces heat transfer from the solid to the fluid. When ε_{sf} is 0.4 or 0.5, temperature increases with time are observed. Due to the limit of the space, we cannot list all the snapshots of the void patterns. However, these series of figures, show that patches of liquid where the local density is considerably low do appear, but they do not persist. That is, these patches only appeared and disappeared randomly in space and time, but no single stable vapor bubble is observed during the whole simulation process. In Figure IV.7 when $\varepsilon_{sf} = 0.75$ the temperature increase with time is the most pronounced, which indicates, unsurprisingly, that the best heat transfer form solid to fluid obtains for the largest ε_{sf}. Unfortunately, Figure IV.8 shows no nucleation during the entire simulation. This is agreement with Maruyama's results[61] that higher ε_{sf} means higher wettability of the solid surface, and thus more difficulty in forming a stable vapor bubble. From these simulations, it appears that 0.4-0.5 is the appropriate range of values for ε_{sf} to generate fluctuations that could possibly lead to a stable bubble, even though these simulations have not yet succeeded in generating such a stable vapor bubble.

We next tried a larger simulation domain with a correspondingly larger number of molecules. Here the size of simulation domain is 28.86σ x 28.86σ x 37σ, which includes 5000 solid atoms in 4 layers and 11560 argon atoms. We pick $\varepsilon_{sf} = 0.45$ and after initial equilibration of the whole system at T=0.75 (the boiling point for Argon), we increase the temperature at the bottom layer of solid to T=1.1. The other parameters and boundary conditions are the same as in the calculations described above. Figure IV.9 shows the temperature profile in fluid region for this run. Again, when the height is greater than 22σ there is a gas region with too few particles there to get good velocity averages, thus leading to temperature fluctuations. However because this system is larger than the previous one, the variations of data is lower and the magnitude of the fluctuations is smaller than in the smaller system above. We again clearly see the temperature increase with the simulation time, which again evinces good heat transfer from solid to fluid. Figure IV.10 plots 3D density contours to represent vapor bubbles when they exist. In the hope of finding a stable nucleated vapor bubble that grows. This series of evolution snapshots show patches of liquid where the local density is low. Again these low-density regions do not persist, but fluctuate in and out of existence. In the theory of nucleation

processes[69], fluctuations create nuclei of different sizes whose probability of appearance decreases exponentially with nucleus size. Only when an embryo whose radius is larger than a theoretical critical radius can the critical stable nucleation process proceeds. What seems to be happening in our simulation is that the radius of embryos that appear cannot seem to exceed this critical size for persistence; thus there is a tendency for these patches to collapse. Rather than continuing to pursue these simulations in the hope of attaining fluctuations greater than the crucial size, we switch below to constant pressure MD experiment. The hope is that this approach will give us both heat transfer and a stable vapor bubble that grows on the solid surface, thereby allowing the tracking of the CL motion.

IV.4 Constant Pressure MD Experiments

IV.4.1 Some Adjustments in Consideration of Nucleation

Nucleation is an activated process. In nucleation, small nuclei begin to form in a meta-stable region (refers to phase diagram of argon in the literature[89]). There is a positive free energy associated with the creation of new surface, and this free energy change as a function of size and reaches a maximum at a critical size. If the nuclei are larger than the critical size, they can grow larger and nucleation proceeds, otherwise nuclei collapse and nucleation stops.

There are two aspects involved in the ease of nucleation—solid surface wettability and the existence of defects in the solid surface. We addressed the first issue in the constant volume MD experiments and learned that the larger the value of ε_{sf}, the higher the wettability of the solid surface and the harder nucleation on that solid surface. We found an appropriate value ε_{sf} =0.45 at that time, given the consideration of nucleation and heat transfer. Here we shall also consider defects in the solid surface. Compared with nucleating a vapor bubble on a clean solid surface, where the creation of a nucleate involves the creation of a significant solid angle of liquid-vapor interface, nucleation in such a defect requires creation of far less interface area. Therefore, the energy barrier required for nucleation in such defects is significantly lower, and the probability of forming such a nucleate in these defects is considerably higher than on a smooth, flat solid surface. Our simulations represent both the top and bottom walls by 4 layers of harmonic molecules in their FCC surface with lateral dimensions of 45.05σ x 45.05σ. At

the center of the bottom wall we artificially create a defect whose largest width of 3σ, whose depth is 3 layers and whose angle is π/3 by removing a few solid atoms. Our simulations also set σ_s = 2.77A (for platinum crystals[63])and the spring constant k=50$\frac{\varepsilon}{\sigma^2}$ (chosen so as to minimize the temperature slip on the solid surface; this issue will be discussed in IV.4.6) B. Novak[92] also calculated approximate critical volume of around 1000-2000A (corresponds to 2-3σ in radius) for different ε_{sf} values (0.5-1.0) by the method developed by L. Bartell and T. Wu[93].

Recall that our purpose is to observe a single stable vapor bubble on the surface of the bottom solid wall. The nucleation rate is defined as the number of nuclei formed per unit volume per unit time. B. Novak[92] also investigated the effect of system size on the nucleate rate. He found that increasing the solid area by a factor of about 2.1 decreased the nucleation rate by a factor of about 1.5. So we increase the system size to 45.05σ x 45.05σ x 30.65σ so as to inhibit nucleation rate and obtain a single stable vapor bubble, 40560 argon atoms, corresponding to an overall fluid density of 0.75, and 23076 solid molecules (11524 molecules in the bottom wall due to the existence of a defect, and 11552 molecules in the top wall). Initially we position all particles at their lattice positions. We again set periodic boundary conditions on the four lateral sides of the simulation box.

IV.4.2 Consideration of Gravity

As we know, when a vapor bubble grows to a certain size so that the Bond number is not longer small, gravity will deform it from its spherical shape until it eventually detaches from the surface. One of our goals is to simulate this process by including a body force that mimics gravity in our MD simulations. Unfortunately, due to the nano-scale size of our system, real "everyday" gravity far smaller than the forces between a pair of molecules and is, in fact, utterly negligible on these scales.

The Bond number is a dimensionless group that describes the ratio of gravity to surface tension. It is the not unreasonable to expect that, for a given ratio of uniform body force to surface tension force, a vapor bubble in a liquid might deform similarly, independent of the actual system being studies. Thus, we note that when the Bond number, say for an air-water system, is ~0.1 (result from chapter III), one begins to notice

bubble deformation leading to detachment. We introduce a uniform body force affecting the fluid particles in our system and define a Bond number based on the magnitude of this force, rather than on true gravity. In order to know how to choose the magnitude of this force, we find the value that for typical vapor bubble sizes expected will give a value for this modified Bond number of ~0.1 so as to allow us to access body-force driven bubble deformation and detachment. For this calculation we need certain properties of argon that we can obtain from reference[94]: at 95-100K, the density of its liquid phase is $0.0203A^{-3}$ (equivalent to $1348.84kg/m^3$) and the density of its vapor phase is $0.00017A^{-3}$ (equivalent to $11.30kg/m^3$); its surface tension is equal to 11.08dyn/cm. We also assume that the vapor bubble will grow to the equivalent radius of 12σ. This value is based on some trial MD experiments without this body force, before the vapor region expands enough to cover almost the whole solid surface; we calculate this radius from $r_{eq} = \sqrt[3]{\frac{3V}{4\pi}}$, where V is the bubble volume, Thus, we obtain a value of the magnitude of this body force, which we shall refer to as MD "gravity," of 0.0005 that we will apply in our MD simulations. Note that this value is equivalent to $3.38 \times 10^{10} m/s^2$, as calculated from $g = \frac{Bo \cdot \sigma}{(\rho_L - \rho_V) r^2}$, nearly nine orders of magnitude larger than terrestrial gravity. This gravity will have different effects on nucleation and on growth. We will address this issue in IV.4.7.

IV.4.3 Constant Pressure MD Simulation Process

Initially we equilibrate the whole simulation box at T=0.75 for 100k time steps by applying velocity-scaling temperature control directly to each phase. Next we directly measure the forces per unit area acting on the solid atoms of the top wall and denote the result as the wall pressure[63]. The equation for this pressure is: $P = \sum_j \sum_i f_{ij} / S$, where S is the surface area of the top wall (45.05σ x 45.05σ) and f_{ij} is the force of the fluid atom i acting on the solid atom j. A discussion of evaluating these forces is founded in section IV.1.2. Each measurement of wall pressure is an average over 500 time steps. Here the wall pressure we measure is around $1.29\frac{\varepsilon}{\sigma^3}$. We then slowly expand the top solid wall at

constant rate of 0.85m/s at constant system temperature T=0.75 to obtain lower top wall pressures of $0.99\frac{\varepsilon}{\sigma^3}$, $0.49\frac{\varepsilon}{\sigma^3}$, $0.25\frac{\varepsilon}{\sigma^3}$, $0.20\frac{\varepsilon}{\sigma^3}$ and $0.12\frac{\varepsilon}{\sigma^3}$. As the system volume increases, the pressure on the wall decreases. We choose a desired pressure and keep it fixed from this point onwards in the simulation by monitoring the wall pressure every 500 steps and adjusting the wall position by moving the wall atoms up and down so as to maintain that pressure. This process is analogous to a cylinder with a frictionless piston, the paradigm for a constant pressure system in thermodynamics. Finally, we instantaneously increase the temperature at of the bottom layer of the bottom solid wall to a temperature T higher than the saturation temperature, 0.75, of argon. We choose this solid temperature, taking into account the existence of temperature slip at liquid-solid interface (we will address this issue in IV.4.6), as at least 1. At the same time, we also maintain T= 0.75 at the top solid wall. This procedure maintains the temperature gradient between solid-liquid surface and the top solid wall so that heat transfer should persist both prior to and after bubble nucleation. As such, once a vapor bubble nucleates, there should be adequate heat transfer to guarantee that vapor bubble has the potential to grow by continued evaporation. Basically, when heat transfers through the bottom solid wall to solid-liquid surface, it can evaporate the liquid layer adjacent to the bottom solid surface. A relatively low wettability (ε_{sf} =0.45) on the bottom solid wall surface is expected to help to sustain the nucleated bubble.

Again, in contrast to previous studies[60,63], that decreased the wall pressure to a negative value at constant temperature to induce bubble formation via cavitation, we fix a positive target pressure at which, prior to heating the bottom solid surface, there are no vapor bubbles in the fluid. We then maintain a constant top wall pressure, and nucleate a vapor bubble by transferring heat though bottom solid wall to evaporate liquid close to liquid-solid surface. For T_s step changed to 1.1, we run the five different test pressures mentioned above for 200k time steps each. Each of these runs shows an average temperature (averaging both across the x-y plane and over 500 time consecutive steps) increase with time, leading to a steady state temperature profile with positive temperature gradient between the thermostated layers on top and bottom walls. Figure IV.11 shows a

sample temperature profile at top wall pressure of $0.12\frac{\varepsilon}{\sigma^3}$. Notice, that, in contrast to the constant volume temperature profile in Figure IV.9, Figure IV.11 has no region of very low density above the liquid and therefore no region at the top where the density fluctuates wildly. Notice also that Figure IV.11's curves have pronounced negative temperature gradients not seen in IV.9, because IV.9's liquid is not in intimate contact with a thermostated upper wall, as is Figure IV.11.

For the solid temperature and number of time steps used, we find a stable vapor bubble nucleus only appears for top wall pressures of $0.12\frac{\varepsilon}{\sigma^3}$ or $0.20\frac{\varepsilon}{\sigma^3}$. Figure IV.12 plots a 3D iso-density profile to visualize a vapor bubble nucleus found for a wall pressure of $0.12\frac{\varepsilon}{\sigma^3}$ at a time of 110K time steps. The figure only shows full dimensions in x and y directions but not full height in z direction.

Again, due to limited space here, we cannot show the long time sequence of bubble nucleation and growth. In Figure IV.13, we show the early growth of a vapor bubble in part of the fluid region, i.e., the full extent of the fluid in the x and y directions and the system height is larger than what the figure shows. The dark black region marks the boundary of the vapor region due to its lower local density (<=$0.15A^{-3}$; this local density is also calculated from a 500 time step average). Notice that, a single whole bubble is scattered around 4 corners, but actually it doesn't due to the application of periodic boundary condition. After initially low local fluid density fluctuations on the surface of the bottom wall, one of patches with low local density successfully grows into a stable vapor bubble there, and then keeps growing due to heat transfer from the bottom solid wall to liquid. We again compare the corresponding temperature profile (Figure IV.11) with the temperature profile from the constant volume MD experiment showed in Figure IV.9 that only generated small fluid density fluctuations, but no stable bubbles over the course of our simulation. In Figure IV.11, the average temperatures (again both spacially averaged in the x-y plane and time averaged over 500 time steps; figure only shows fluid phases) at different heights now show fluctuations for heights less than 15σ. These fluctuations are due to the appearance of a stable vapor bubble and the fact that x-y averages at heights below the height of the bubble cut through both liquid and vapor

phases. Notice that the temperatures in fluid phase do increase noticeably with the time and the temperature gradient is maintained between two solid walls, i.e. there is a nearly steady heat transfer from the bottom solid through the fluid region to the top wall, which, among other things, sustains the vapor bubble's growth during this growth phase. We shall follow the bubble's later evolution in Section IV.4.6.

IV.4.4 Measurement of Vapor Bubble Volume, Contact Angle and CL Radius

Once having obtained a stable vapor bubble on the solid surface, one of our main interests is the motion and instantaneous position of the contact line. One discerns the CL by looking at the instantaneous configuration of the particles near the phase boundary and trying to fit a separating curve between the phases. Naturally, there needs to be a sufficient number of particles at this boundary to well-define this curve and for the resulting contact angle to be meaningful. Our MD simulations thus far use 40560 argon atoms in the system, of which a small fraction defines the said interface. Clearly more particles will lead to a more well-defined interface.

In order to extract CL information, we plot 2D density distribution profiles in r-z plane by taking azimuthal averages of the local density about the center of the bubble base on the bottom solid wall. We implement that as follows: first we check the 3D local density profile and mark the solid surface region covered by vapor bubble as S_c. Then we calculate the center of bubble base by $R = \frac{\int d_i R_i}{\int d_i}$, where d_i is the local density on S_c and R_i are the coordinates (x and y) corresponding to d_i. Finally we take azimuthal averages of the local density about R over the height of around 20σ and the radius of around 16σ. Due to the fluctuations in the instantaneous positions of the individual argon atoms, we also need to average in time, and we choose to take such averages over 500 consecutive time steps. In order to smooth the density-derived bubble shape profiles, we take n points along the vapor-liquid interface in the r-z plane and employ Lengendre polynomial to create a least square fit of these n points. This results in a smooth, axisymmetric bubble shape in the r-z plane. Legendre polynomials occur in the solution of Laplace's equation where the boundary conditions have axial symmetry (no dependence on the azimuthal angle), and they are appropriate for this non-linear curve fitting procedure. The first Legendre polynomial is the spherical shape, which one expects to find ideally at the

bubble's earliest growth stages, when its shape is determined by surface tension alone. Instead of taking a linear combination of infinitely many Legendre polynomials, we take only a few of them (here we use 3). That is, we approximate the fitting function with a finite linear combination of a subset of the "basis" as:

$$y(\cos(\theta)) \approx a_0 \cdot 1 + a_1 \cdot \cos(\theta) + a_2 \cdot \frac{1}{2}(3\cos^2\theta - 1) \tag{IV.21}$$

where y is the fitting function and $\cos(\theta) = \frac{r}{\sqrt{r^2 + z^2}}$

Then, as is standard procedure, we take the partial derivatives of the sum of squared errors with respect to each of the constants in $y(\cos(\theta))$ and set them to zero to get the linear equations for these constants:

$$\begin{aligned}
&x_i = \cos(\theta_i) \\
&n \cdot a_0 + \sum_{i=1}^{n} x_i \cdot a_1 + \sum_{i=1}^{n} \frac{1}{2}(3x_i^2 - 1) \cdot a_2 = \sum_{i=1}^{n} y_i \\
&\sum_{i=1}^{n} x_i \cdot a_0 + \sum_{i=1}^{n} x_i^2 \cdot a_1 + \sum_{i=1}^{n} \frac{1}{2}x_i(3x_i^2 - 1) \cdot a_2 = \sum_{i=1}^{n} x_i y_i \\
&\sum_{i=1}^{n} \frac{1}{2}(3x_i^2 - 1) \cdot a_0 + \sum_{i=1}^{n} \frac{1}{2}x_i(3x_i^2 - 1) \cdot a_1 + \sum_{i=1}^{n} [\frac{1}{2}(3x_i^2 - 1)]^2 \cdot a_2 = \sum_{i=1}^{n} \frac{1}{2}(3x_i^2 - 1) y_i
\end{aligned} \tag{IV.22}$$

a_0, a_1, a_2 can be solved to obtain the fitting function.

Given the bubble's shape, one can easily calculate the volume of the bubble by analytically or numerically integrating the fitting function as an axisymmetric 3D shape. The contact angle is the derivative of the fitting function with respect to θ at θ=π/2 and the radius of the CL is the value of fitting function at θ=π/2.

IV.4.5 The Effect of the Random Number Generator's (RNG) Seeds on Vapor Bubble Growth

MD simulations need to prescribe the initial velocities of the constituent atoms or molecules. These speeds are a function of the temperature of the system and the mass of the particles, but they satisfy the Maxwell-Boltzmann distribution at thermal equilibrium. We employ the Box-Muller method[87] to generate 3N random velocity components (N is the number of particles) that satisfy the Maxwell-Boltzmann distribution. Suppose U_1 and U_2 are independent random numbers that are uniformly distributed in the interval [0, 1]. Let

$$Z_0 = \sqrt{-2\ln U_1}\cos(2\pi U_2) \text{ and } Z_1 = \sqrt{-2\ln U_1}\sin(2\pi U_2) \quad \text{(IV.23)}$$

Then Z_0 and Z_1 turn out to be independent random variables with a normal distribution of standard deviation 1. After removing velocity drift, i.e. the streaming velocity mentioned in section IV.1.6, we can rescale the velocities so as to have the average kinetic energy for the given temperature and particle mass by multiplying their original values by a factor of $\sqrt{\frac{\frac{3}{2}Nk_bT}{\sum_i \frac{1}{2}mv_i^2}}$. A random number generator (RNG) will generate independent random numbers that are uniformly distributed in [0, 1] but an initial number (called the seed) has to be an input into the RNG. Clearly when the seed changes its value, the whole sequence of random numbers that follows will also change. This will change the amount of time needed to achieve thermal equilibrium.

In this subsection, we repeat the constant pressure MD experiments with exactly the same parameters and boundary conditions applied above, but just vary the RNG seeds. First, even with different RNG seeds, our simulations indeed show nearly identical average temperature increases with time and, after initial low-density fluctuations, they show that one of nuclei grows into a stable vapor bubble, just as in the constant pressure MD experiment in IV.4.3. Naturally, the position of the stable vapor bubble varies depending on the seeds we choose. Second, Figure IV.14 compares the growth of the volume of the stable vapor bubble with time for different seeds. Reassuringly, these growths do not show any significant differences and in all cases, somewhat surprisingly, the volumes of vapor bubbles grow almost linearly with time. This contrasts with the $V \sim t^{1.5}$ seen in our continuum models. This different growth behavior may be due to various factors. One possibility is related to the temperature slip that exists at the solid-liquid interface[95] in MD simulations. That is, instead of the local (i.e., in a box large compared with a single particle, but small compared with other characteristic length scales of the problem) temperature in the fluid and in the solid at the fluid-solid interface being continuous, it experiences a sudden jump there. We will quantify the temperature slip issue in section IV.4.6. If the issue were merely one of a jump in the temperature averaged over the entire x-y surface being discontinuous at the solid-fluid surface, then

one would expect only a decreased thermal driving force in the fluid. This would, naturally, slow bubble growth via evaporation at the CL, which should lower the prefactor in the volume vs time curve, but not the exponent. However, the lack of local temperature continuity can affect bubble growth in MD in two more important and more subtle ways. First, since the liquid-vapor interface defines a length scale that is, even here, far smaller than that of the bubble, one would have to consider the "temperature" of the interface as being defined in the sense of a limit of temperatures as one approaches the interface. As such, in contrast to the continuum model, it is unclear whether a temperature so-defined can directly impact the temperature of the solid in contact with the liquid-vapor interface. Second, even if this temperature at the CL in the fluids is well established, the temperature slip at the solid-fluid boundary severely limits its ability to locally cool the solid there and cause the CL to act as a heat sink. Figure IV.15 plots the radius of the CL vs the equivalent radius of the vapor bubble, i.e., $(3V_b/4\pi)^{1/3}$ for three different RNG seeds. Again the seeds show no significant effect on these curves. The radius of CL grows almost linearly with the radius of vapor bubble until $r_b = 16\sigma$, consistent with the assumption made in Section III.3's simple model to explain the continuum results. Figure IV.16 is a plot of the variation of the contact angle with time for three different RNG seeds. Again the seeds have no discernable effect on the contact angle's variation during vapor bubble growth. The bubble's contact angle fluctuates about 130^o.

From the curves in Figures IV.14-IV.16, we can exclude the possibility of a significant effect of the RNG seeds on the behavior of the vapor bubble's growth. In this simulation, the vapor bubble does not deform and there is no CL contraction as found in our continuum model for Bond numbers approaching ~0.1 and higher. Figure IV.17, a plot of the Bond number vs time, shows that the bond number increases as the vapor bubble grows until it reaches a value of 0.1, where, as noted, our continuum model show deformation. In our MD simulation, the vapor bubble continues to grow, mainly by spreading in the x-y plane, rather than by growing upwards. There are two likely causes for this behavior. First, it is possible that the Bond number, i.e., the body force, is still too small to pull the bubble shape upwards, and a larger body force is needed. Alternatively, it is possible that when the bubble reaches the present height, the top of the bubble feels a

lower temperature than the solid-fluid interface. It is possible that that temperature at the top of the bubble is the actual saturation temperature and that the bubble does not continue to grow upwards because the vapor particles are condensing at the z position. We shall deal with this latter possibility in Section IV.4.10.

IV.4.6 Consideration of Temperature Slip at the Liquid-fluid Interface

In our continuum approach to treat nucleate pool boiling, in the absence of mass flow and under small Peclet number assumption, Laplace equation for the heat conduction only describes the quasistatic heat conduction. Furthermore, we assume that the temperature and the thermal flux be continuous at the liquid-solid interface. However, in reality there is no real physics to assume that the temperature is continuous across a liquid-solid interface. In 1941, a discontinuous temperature drop at a liquid-solid interface was discovered by Kapitza[96]. This drop is described by the interfacial thermal resistance, also called the Kapitza resistance, R_K. R_K is not significant for most solid-liquid interfaces, but it can be significant in nano-size materials; it can therefore be significant in our simulation of a nanoscale version of our boiling system, even if it is not significant on the scale of vapor bubble of interest, i.e., of tens of microns to millimeters. R_K is usually expressed in terms of the thermal resistance thickness, L_K, also known as the Kapitza length, which is defined as the width of the bulk medium over which there would be the same temperature drop as that at the interface.

B.H.Kim et al[95] investigated the effects of a thermal oscillation frequency and surface wettability (as we have already seen, this wettability is related to the strength of the fluid-wall interaction) on the L_K by MD simulation. He studied three-dimensional heat conduction between parallel plates separated by a thin layer of liquid argon. The thermal oscillation frequency is approximately predicted by $\varpi \approx \sqrt{K/m}$ in which K is the crystal spring constant and m is the mass of a solid molecule. He found that L_K growth is proportional to K_w^2 (where $K_w=64(4\varepsilon/\sigma^2)$) but L_K varies exponentially with the interaction strength between solid and fluid. In our simulation, spring constant is set to $50\varepsilon/\sigma^2$, much less than the minimum value used (K_w) in Kim's MD simulations, therefore, we eliminate its effect on L_K and will focus on the effect of ε_{sf}. Furthermore, R. Khare etc[97] presented their MD simulations for heat and momentum transfer at solid-

liquid interface. They found that both thermal and velocity slip (an analogous discontinuity in tangential) are strongly influenced by the fluid-wall interactions.

As a result, it may be beneficial for speeding up heat transfer and bubble growth in constant pressure MD experiments, to increase ε_{sf}. As such, below we increase ε_{sf} to 0.5,0.6 and 0.75 under a top wall pressure of $0.12\frac{\varepsilon}{\sigma^3}$ and a bottom solid wall temperature of T=1.1 to check the temperature slip at the interface and to observe if the stable vapor bubble can nucleate and grow under these higher solid-fluid interaction strengths. The (super-) gravity value used here is g =0.0005. Figure IV.18 shows the temperature profile in fluid region for different ε_{sf}. We find that the temperature in the fluid region increases monotonically with the time for all of the pre-steady state cases and this temperature increase is larger at early times and smaller at later times. Due to the existence of the temperature gradient between the bottom solid-fluid interface and the top solid wall, after longer simulation times we expect to obtain a steady state decreasing temperature profile that corresponds to steady state heat transfer. We also see that, with an increase of ε_{sf}, the temperature at the solid-liquid interface at the end of the simulation (after 455k time steps) also increases, i.e, the temperature-slip at the interface is smaller, which is agreement with the calculations from B.H.Kim et al[95]. This is what one would expect, since the more interaction between the phases, the lower temperature slip one would expect. Finally we check the 3D iso-density plots for these different cases to see if a stable vapor bubble appears at the (arbitrarily chosen) wall pressure of $0.12\frac{\varepsilon}{\sigma^3}$. We find that when ε_{sf} = 0.75, no stable vapor bubble exists. This is consistent with expectation because the higher ε_{sf}, the higher the wettability on the solid surface, and thus the lower the probability of nucleation of a nucleus of adequate size on the solid surface. We find, however, when ε_{sf} =0.5 and 0.6, at some time one of low density vapor patches grows successfully into a stable vapor bubble and the vapor bubble can continue to grow with time. Given the balance between temperature slip and bubble nucleation/growth, we shall choose ε_{sf} =0.6 for future simulations in the subsections below. The time evolution of vapor bubble nucleation and growth for ε_{sf} =0.6 for pressure $0.12\frac{\varepsilon}{\sigma^3}$ is shown in Figure

IV.19. It is important to mention here that, as in our discussion above, even as the vapor bubble grows larger and heat continues to transfer from the solid to the fluid region, instead of a bubble that is deforming upwards form its spherical shape as it grows, this simulation exhibits a vapor bubble instead tends to spread out in the x-y plane. This leads to our next discussion about the role of gravity and about the precise value of the saturation temperature alluded to above.

IV.4.7 The role of gravity

On earth, surface tension competes to keep a vapor bubble on the solid surface and while gravity/bouyancy tries to pull it upwards from the surface. When a vapor bubble is tiny, the gravitational force on it is small; thus the vapor bubble does not "feel" the existence of the gravity, and surface tension is dominant in determining its shape. When the bubble is small, if the bubble does not grow extremely rapidly, its Capillary number, the ratio of viscous to surface tension forces, is also small and its shape at this growth stage is a section of a sphere. As the vapor bubble grows larger, the gravitational force increases so that the ratio of gravity to surface tension forces (the Bond number) is no longer small. At this stage the competition between surface tension and gravity forces determines the vapor bubble's shape. Buoyancy that lifts the bubbles strongly affects the escape of the vapor bubble from the heated surface in nucleate pool boiling heat transfer, giving way to fresh liquid to replace it on the surface. If the gravitational force is small and bubbles are generated faster than gravity can pull them from the surface, the bubbles that reside close to the surface can coalesce into a large mass of vapor that is difficult to condense due to its low surface to volume ratio; this vapor can prevent liquid from reaching the surface and retard heat transfer from it. The figures in the last subsection suggest this may be the case in those simulations. Therefore, we shall increase the magnitude of the super-gravity in our MD simulations so as to try to deform and pull the vapor bubble off the solid surface. Increasing gravity can also have another effect. Such an increase increases the pressure acting on the liquid-vapor interface of a newly-formed vapor nucleus from the surrounding fluid. In view of the Young-Laplace equation ($P_l = P_{Top} + \rho_l gh$) in order to prevent these nuclei from rapid collapse, one must either maintain a higher pressure inside the vapor bubble or lower the pressure outside of it.

When we increase the super-gravity force in our MD simulations, we will simultaneously apply a lower top wall pressure so as to encourage the formation of a stable vapor bubble.

As such, we double our original super-gravity value to 0.001 and try top solid wall pressures of $0.12\frac{\varepsilon}{\sigma^3}$, $0.1\frac{\varepsilon}{\sigma^3}$ and $0.08\frac{\varepsilon}{\sigma^3}$ to see if a stable bubble appears. The other parameters remain as before: T_s =1.1,ε_{sf} =0.6. At the wall pressure of $0.1\frac{\varepsilon}{\sigma^3}$ we find that a stable vapor bubble forms and grows with time due to the heat transfer, but it still does not deform upwards despite the larger gravity value. When we triple the original gravity value to 0.0015 and apply the top solid wall pressures of $0.1\frac{\varepsilon}{\sigma^3}$ and $0.08\frac{\varepsilon}{\sigma^3}$ with all other parameters unchanged, a stable vapor bubble again appears and grows under the top wall pressure of $0.08\frac{\varepsilon}{\sigma^3}$. Figure IV.20 shows how this vapor nucleus grows into a stable large vapor bubble. We observe at later simulation times after the height of bubble becomes around 20σ, the bubble's shape simply fluctuates but its volume ceases to increase. This may be due to some loss of heat transfer to maintain its growth or, as suggested above, to condensation at the top of the bubble. We first check the time-dependent temperature profiles in Figure IV.21. Part (a) shows the curves from the step at which we obtain the appropriate pressure and suddenly increase T_s =1.1 through the time step where the vapor bubble achieves a height of around 20σ; the curves in (b) corresponds to times beyond that, where the vapor bubble fluctuates but no longer grows. During the former times, the temperature profile is unsteady, whereas in (b) it seems to have reached steady state. Since the steady profile clearly has a negative gradient, we exclude the possibility of no heat transfer. This leaves the second possibility, that the temperature at the top of vapor bubble is lower than actual fluid saturation temperature' thus condensation at the top of the vapor bubble balances evaporation near its base. We will address this scenario in Sec. IV.4.10.

Another problem in Figure IV.21 is that gravity never deforms the vapor bubble from its truncated nearly spherical shape, possibly because the Bond number, which in the final frame of the figure is 0.3, is still too small. To remedy this, we quadruple the

original gravity value to 0.002, and apply top solid wall pressures of $0.05\frac{\varepsilon}{\sigma^3}$, $0.03\frac{\varepsilon}{\sigma^3}$, $0.02\frac{\varepsilon}{\sigma^3}$ and $0.01\frac{\varepsilon}{\sigma^3}$, with the other parameters unchanged. Unfortunately, under these pressures, we do not observed the appearance of any stable vapor bubbles over the simulation times studied. Because we are not interested in nucleating a vapor bubble under negative pressure, rather than using these very higher super-gravity values during the nucleation process, we instead nucleate the bubble at low gravity and then gradually raise g. Our hope is that this protocol will induce bubble deformation and detachment rather than causing it to condense due to the resulting higher hydrostatic pressure. We thus nucleate a bubble at gravity g=0.0015 under a top wall pressure of $0.05\frac{\varepsilon}{\sigma^3}$. Once the vapor bubble grows to ~20σ in height (at 455k time step), we gradually raise the system gravity from g=0.0015 to g= 0.015 (30 times the original value) in 80k time steps. Figure IV.22 shows the latter time evolution of this vapor bubble after 455k time steps. It clearly shows a single vapor bubble deforming at 505.5k time steps (when the gravity has reached 0.0100) and detaching from the solid surface at 508.5k time steps (when g=0.0105). Notice that the detachment process is very rapid, taking only 3k time steps from the onset of bubble deformation to its detachment due to this very high super-gravity. Compared with the relatively long time interval for vapor bubble nucleation and growth (which took 183k time steps in this run at the lower g value), the deformation and detachment processes are extremely rapid. Note that the latter panels of the figure also show the nucleation and growth of bubble on the top wall, where the pressure is far lower, as the bubble on the lower wall deforms and detaches. In light of our continuum model, it is also noteworthy that the vapor bubble appears leaves some vapor residue when it detaches from the solid surface, but in later panels, this residue appears to condense due to the high hydrostatic pressure ($P_l = P_{Top} + \rho_l gh$) that it feels at the high super-gravity needed to detach the bubble. Figure IV.23 shows that the temperature profile of fluid phases has almost reached steady state by 455k time steps and hardly changes only by virtue of the vapor bubble, with its low particle density rising. When the

vapor bubble detaches from the solid surface, the temperature close to the solid surface increases from 0.87 to 0.9.

Whereas, it is an achievement to have accomplished bubble deformation and detachment, it would be much more realistic to simulate the growth and detachment of a vapor bubble under constant super-gravity conditions. We first try to find deformation and detachment with a smaller variation in g. After the vapor bubble grows to some critical size (say 10σ in equivalent radius) under a system gravity equal to 0.0015, we gradually increase system gravity to various higher values in 80k time step. We consider 4 different cases: a) gravity from 0.0015 to 0.0075 (15 times original gravity; b) gravity from 0.0015 to 0.0065 (13 times original gravity; c) gravity from 0.0015 to 0.005 (10 times original gravity; and d) increase gravity from 0.0015 to 0.004 (8 times original gravity) with all other parameters such as top wall pressure and ε_{sf} unchanged. No deformations are observed in this stage and after that we keep these higher body forces to expect them to deform and detach vapor bubble. Again due to limited space, we cannot show the time evolutions of vapor bubble growth for all these cases. Deformation and detachment of a single vapor bubble is observed under all of these higher super-gravity values except g=0.004. However, the time from initial deformation to vapor bubble detachment decreases as g increases. For example, these processes take 7k steps for target g=0.0075 but takes 15k steps for target g=0.005. The evolution of the temperature profiles in all of these cases is, not surprisingly, quite similar to Figure IV.23, with the system essentially at the steady state by the start of these processes. Figure IV.24 (a) plots the time evolution of the contact line radius for target g=0.0075. In the figure, the red points represent the vapor bubble's growth stage and the blue points represent the vapor bubble's deformation and detachment. We can see that the radius of CL initially expands with growth of the vapor bubble, then it contracts sharply but continuously with the deformation of the vapor bubble until its detachment. The CL motions that we obtained here by MD simulation has a similar trend with the experimental CL motions observed by S. Gong et al[77] and shown in Figure IV.24 (b), especially for $\Delta T=9.9^{o}C$. The Bond number where the bubble began to deform and detach in their experiment (for $\Delta T=9.9^{o}C$ case) was 0.23, which is different from the 0.5 that we obtained in MD (For $T_s-T_{sat}=42^{o}C$, for a solid-liquid interface temperature with the temperature-slip, $\Delta T=12^{o}C$). This is

because we need to apply super-high "gravity" in MD simulation in order to pull the vapor bubble against surface tension. When we check time evolution of bubble volume in Figure IV.25, we find, surprisingly, that, instead of seeing the bubble volume growing with time, we find that the bubble volume in fact decreases. This again is a clear indication that some part of the vapor bubble is condensing, and, as the bubble is further stretched upwards towards cooler temperatures by super-gravity, this condensation increases. This indicates that the temperature to which we controlled the top solid wall is lower than the system's true saturation temperature at the ambient pressure. Even though 0.75 is the literature value, it applies at a pressure of $0.12\frac{\varepsilon}{\sigma^3}$; with appreciable super-gravity values, the pressure in the fluid phase, and therefore the local saturation temperature, vary with z. We shall try to remedy this issue after first examining the effects of solid thickness and bottom solid wall temperature T_s on vapor bubble growth.

IV.4.8 Effect of Solid Thickness on Vapor Bubble Growth

In all of our previous simulations, we employed 4-layers of metal atoms to form the solid wall. We found that the average temperature (averaged over the x-y plane and over 500 time step) is nearly independent of the height of the solid wall; except for very short times (~48k time steps), it is nearly uniformly at the thermostated bottom layer temperature. Actually, the time to reach this uniform temperature increases slightly with increasing wall thickness (48k time steps for a 4-layer solid vs 50k time steps for an 8-layer solid in Figure IV.26). Recall in our continuum model, we argued that the liquid-vapor local interface equilibrium should dramatically cool the local temperature to fluid's saturation temperature at the 3-phase CL, thus generating the large thermal gradient in the solid close to the CL. When one multiplies this temperature gradient in the solid phase by the very high thermal conductivity of the solid, one obtains the very high heat flux observed and the greatly enhance heat conduction through solid towards the CL. It was to examine this *Ansatz* that partially motivated our interested in the CL temperature in MD simulation. The discussion in Sec. IV.4.6 seems to indicate that at the nanoscale, temperature slip at the solid-fluid interface may interfere with the continuity of the liquid-vapor interface temperature with the solid CL temperature and therefore render the nanoscale system not fully comparable with the macroscopic system that is at least 10^3 or

10^4 times as large. Before drawing this conclusion we check the local temperature distribution in the first layer of the fluid phase above the solid and in the top solid layer that is adjacent to the first layer of the fluid phase. For convenience, we call these plots 2D local temperature profiles. We will also check whether these profiles change for a thicker (8 layers of solid atoms) bottom solid wall. The simulation conditions are: ε_{sf} =0.45, g=0.0005, P_{top} =250,T_s =1.1,T_{top} =0.75.

Figure IV.27 shows the 2D local temperature profiles in both the solid and fluid regions for both 4 and 8 layer solid walls and for different simulation times. Pictures above/below the bold black line represent time 400k/ 455k; pictures on the left/right represent 4/8-layer solid wall. "Liquid" means bottom liquid layer; "Solid" means top solid layer. We tried time-averaging over 500 and over 1000 steps, but saw no significant difference.

For either wall thickness, after 50k time steps, the x-y plane average temperature at the top of the solid wall is close to the controlled bottom solid layer temperature, with local regions of even higher temperature, due to fluctuations. Due to the existence of temperature-slip at the solid–fluid interface, the temperature scales in solid and liquid layer are different. For the solid, the dark regions represent temperatures less than or equal to 1.0, while for fluid, the dark regions represent the temperature is less than or equal to 0.5. The bold white line in each picture shows the CL position as determined from the iso-density contour calculation and the white region in the center of the solid layer represents the defect where the bubble is most likely to nucleate. In the first liquid layer, modulo fluctuations, the CL hugs the boundary of the region whose temperature is the lowest, which is consistent with the idea that the local equilibrium of the liquid-vapor interface maintains the CL at or very near to the fluid saturation temperature; for the solid part, most of the CL again hugs the edges of the coolest parts of the solid surface, but the temperatures there tend to lie between 1 and 1.1, i.e. values far higher than the saturation temperature. Again, this is consistent with the pronounced temperature slip present in this nanoscale system, i.e., if the CL on the fluid side of the boundary is at T_{sat}, then, with temperature slip, on the solid side of the boundary, the CL is at a higher temperature that is still the lowest, modulo fluctuations, temperature anywhere along the top solid surface.

As we have seen previously, as the bubble grows with time the CL expands. The thickness of the bottom solid wall does not show much influence on the 2D local temperature profile. However, Figure IV.28 shows that the vapor bubble grows a little bit faster on the 4- than on the 8-layer wall but both grow linearly with time (i.e. V~t; slopes 6.58, 6.24 for 4- and 8- layer walls). If heat were only transferring to the bubble through the solid, one might guess that this slope would vary inversely with the solid thickness, but this is clearly not the case because the heat is transferring through the liquid as well.

IV.4.9 Effect of the Temperature at the Bottom of the Solid Wall on Vapor Bubble Growth

If the temperature on the bottom of solid wall is too low, the temperature on both sides of the solid-liquid interface will also be low, with the fluid value lower due to temperature-slip there. If the temperature on the liquid side of the solid-fluid interface is as low as the temperature that we fix on the top solid wall (say 0.75), then there is no macroscopic driving force or heat transfer through the fluid phase(s). If this temperature is too high, the temperature at the solid-liquid interface will be correspondingly higher, which drives a far higher nucleate rate; thus instead of only nucleating one or few vapor bubble, too many nuclei for us to follow individually can appear on the solid surface, and they can merge before they have undergone significant single bubble growth. In our simulations, we set T_s = 0.9, 1.1,1.2 and 1.3 respectively while keeping all other parameters fixed at: ε_{sf} =0.45, g=0.0005, P_{top} =250,T_s =1.1,T_{top} =0.75. Figure IV.29 shows the vapor bubble growth for these different T_s values; again, all show linear growth (i.e. V~t) with slopes 6.58,8.1,5.61 respectively. As expected, the vapor bubble grows faster when T_s is higher (e.g., T_s=1.2 vs T_s=1.1); however, when T_s=1.3, there are 2 stable bubble appears (one is large, another is small; we calculate the volume of the larger one), while when T_s = 0.9, we observe only temperature fluctuation around 0.75 but no stable bubble in the fluid phase. Therefore, most our simulations use T_s =1.1. Again, if heat were transferring only through the solid to the bubble surface at T_{sat}, one would expect the slope to be proportional to T_s-T_{sat}. For T_s=1.1, slope 6.58 and ΔT 0.35 and for T_s=1.2, slope 8.1 and ΔT 0.45, it is not consistent with that.

IV.4.10 Exploring New Procedure for Vapor Bubble Growth and Detachment with Time-invariant Gravity

There are at least two shortcomings of our study of heterogeneous, heat-transfer-driven vapor bubble nucleation and subsequent: one is that the top of the vapor bubble undergoes some condensation as super-gravity tries to pull it off from the solid surface; this may indeed happen in real boiling situations as well when the vapor bubble is large enough to feel the temperature gradient in the liquid. The other is that these simulations do not allow us to measure and to follow the fate of residue bubbles on the solid surface after vapor bubble departure because the value of the super-gravity that we use to induce detachment induces a high enough pressure at the solid-liquid interface to cause the small residue to immediately condense. To alleviate the first issue, when note that when the bubble growth appears to have halted, we presume this halt is because the temperature at the top of vapor bubble is at or lower than the true fluid saturation temperature at the local pressure and therefore induces condensation there. So, at that point, rather than drastically raising the value of the super-gravity used, we change the temperature at the top solid wall to the temperature at the top of vapor bubble and leave super-gravity unchanged. This should keep the entire fluid region above its saturation temperature at all local fluid pressures present, and we expect the vapor bubble to resume growing. Since we will not be raising the super-gravity in order to allow the bubble to grow further and, as a consequence, increase its Bond number, this should also address the second issue, since the original bubble was able to nucleate at that super-gravity.

In Section IV.4.6, we found that for g=0.0015 we obtain a single stable vapor bubble for top wall pressure of 100 with ε_{sf} =0.6. The vapor bubble grows to a height of ~20σ with a temperature at the bubble apex (see temperature profile in Figure IV.21) of 0.8 at 455k time steps, where its net growth halts. At this point we change the top wall temperature from 0.75 to 0.8 run and plot (in Figure IV.30) simulations for another 180k time steps. The bubble indeed resumes its growth, reaching 30σ in this time. Unfortunately, the bubble's CL grows to an extent comparable to the x-y extent of the simulation box and combines with its image bubbles (at t=635k – see Figure IV.30) before one observes gravitationally-induced pull-off. The Bond number in Figure IV.22 where the bubble began to deform and detach was 0.5. At g=0.0015, this Bond number corresponds to a bubble radius of 18σ. Currently we are trying this simulation in a simulation box large enough to accommodate a bubble of this size without impinging on

the top of the box and where the x-y extent of the simulation box is large enough to avoid the bubble's merging with its image bubbles. We are currently running this simulation.

Figure IV.1 Constant pressure MD simulation domain

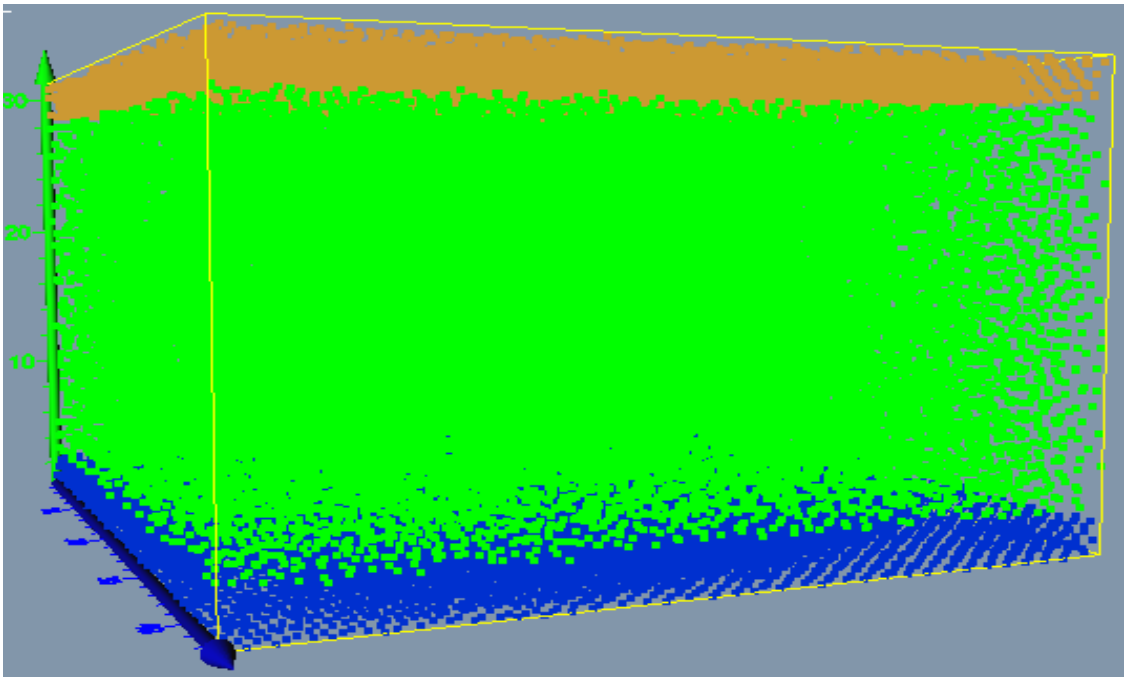

Figure IV.2 Temperature profile in fluid phase (ε_{sf} =0.3)

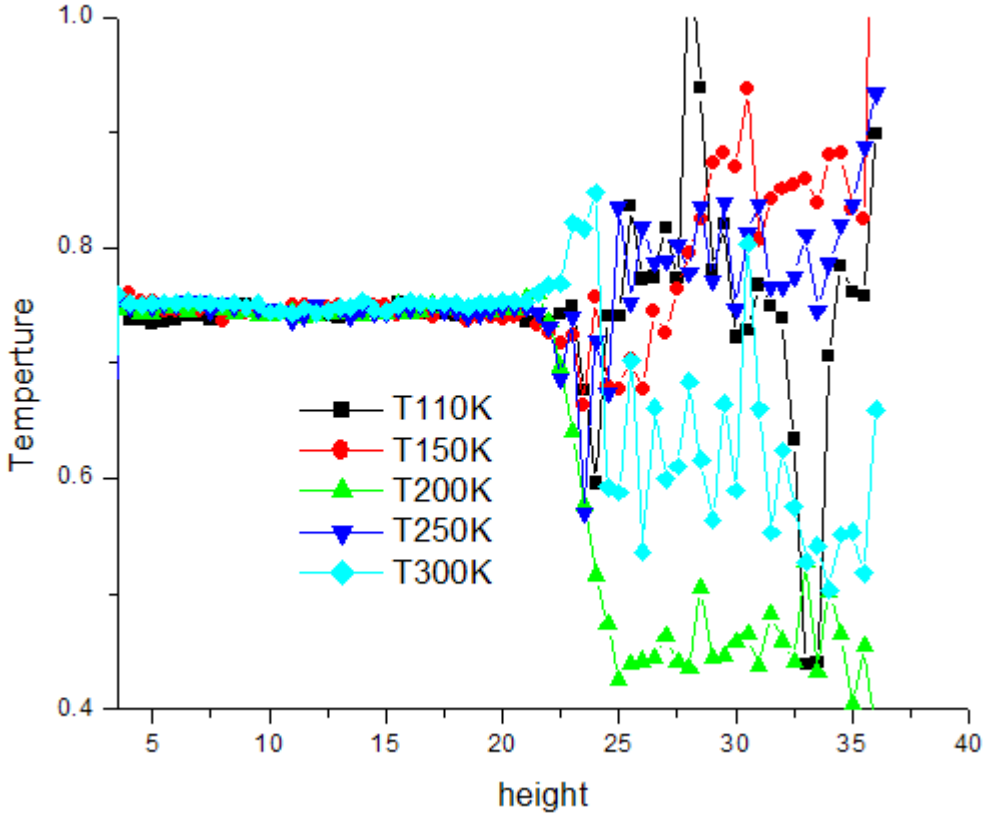

Figure IV.3 Temperature Profile (ε_{sf} = 0.4)

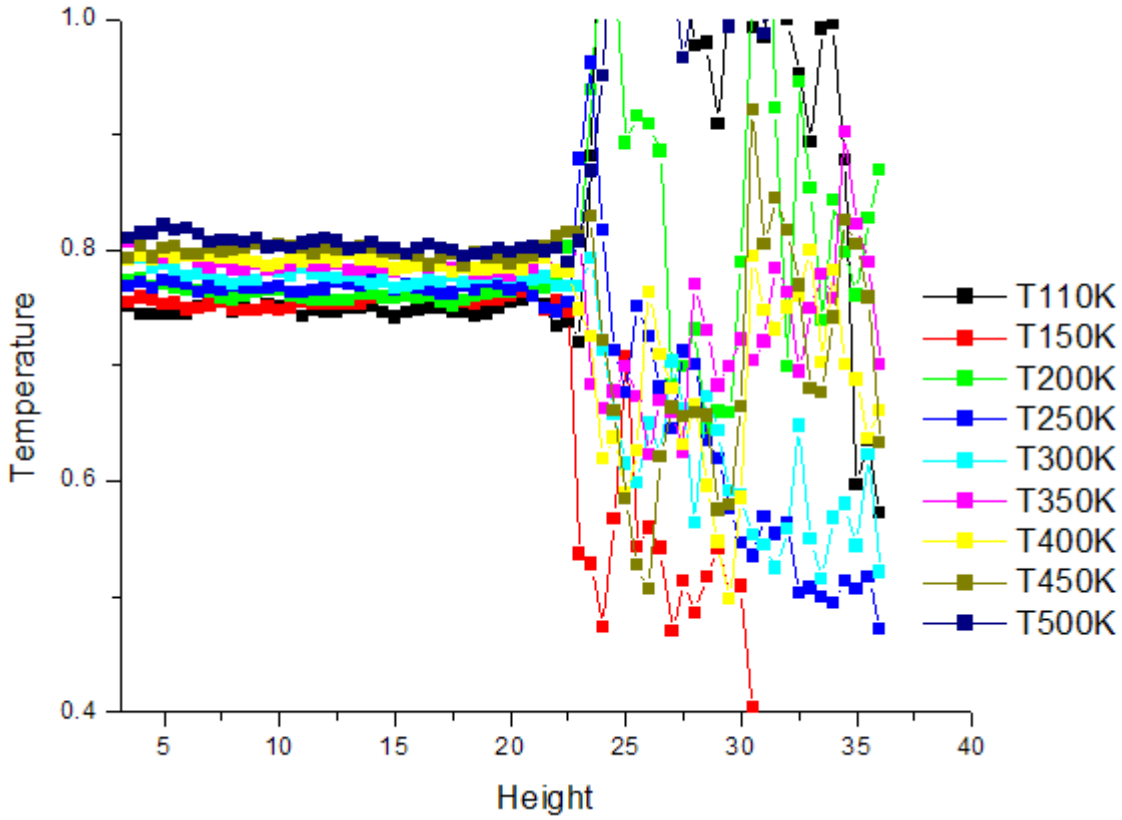

Figure IV.4 Snapshots of vapor bubble (ε_{sf} = 0.4)

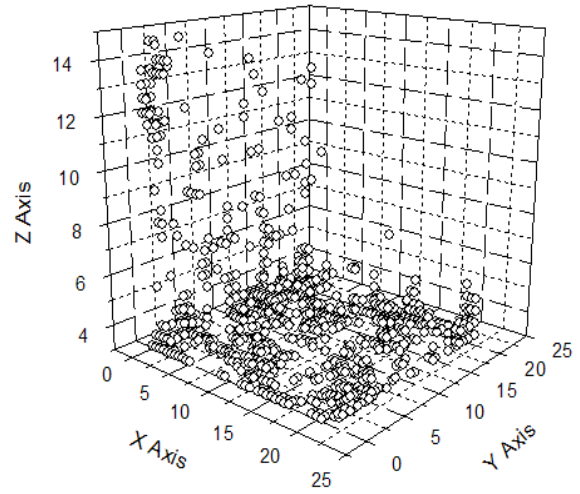

250k time step

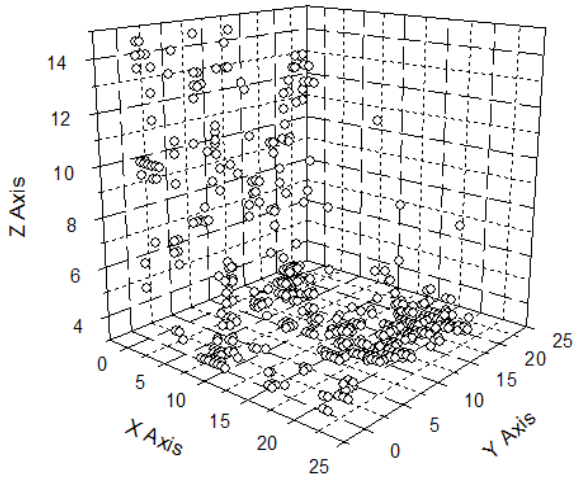

350k time step

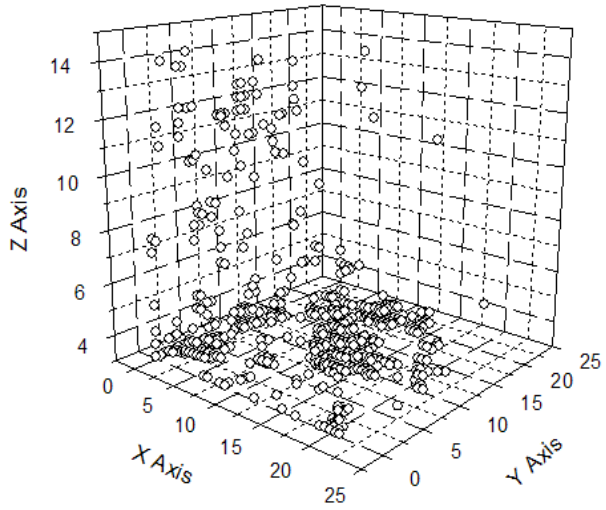

500k time step

Figure IV.5 Temperature profile in fluid phase (ε_{sf} = 0.5)

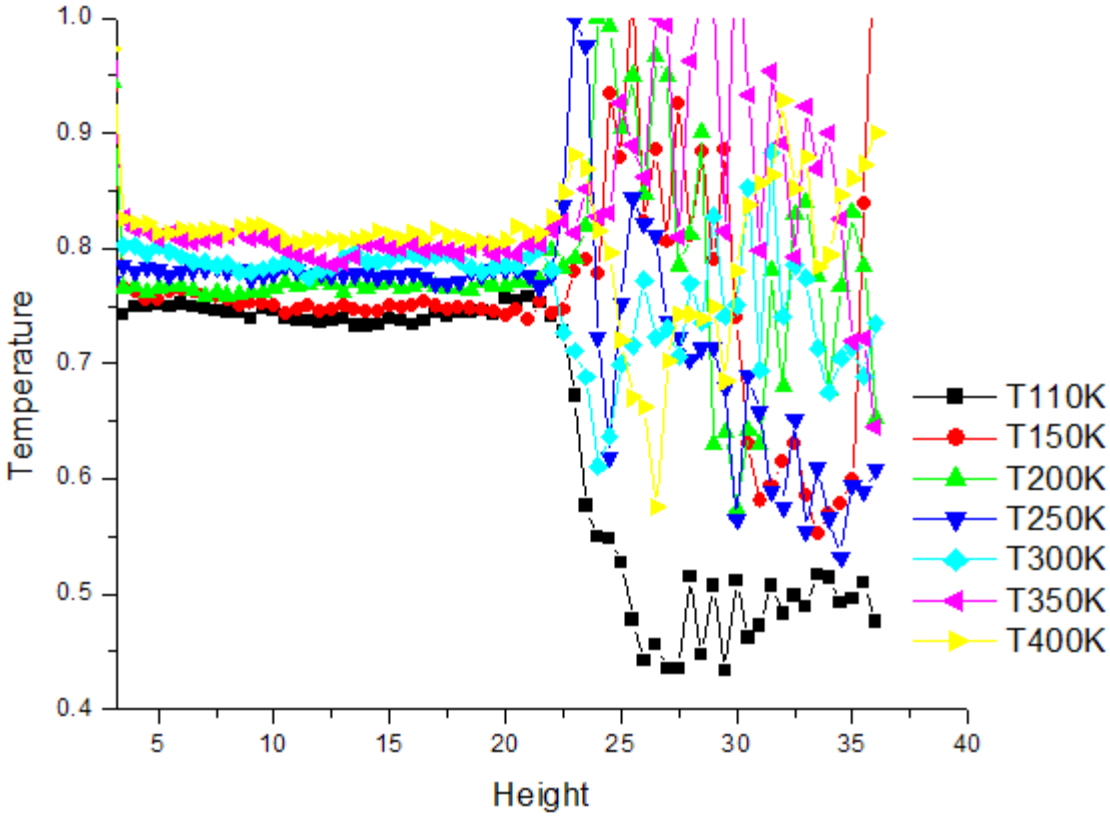

Figure IV.6 Snapshots of vapor bubble (ε_{sf} = 0.5)

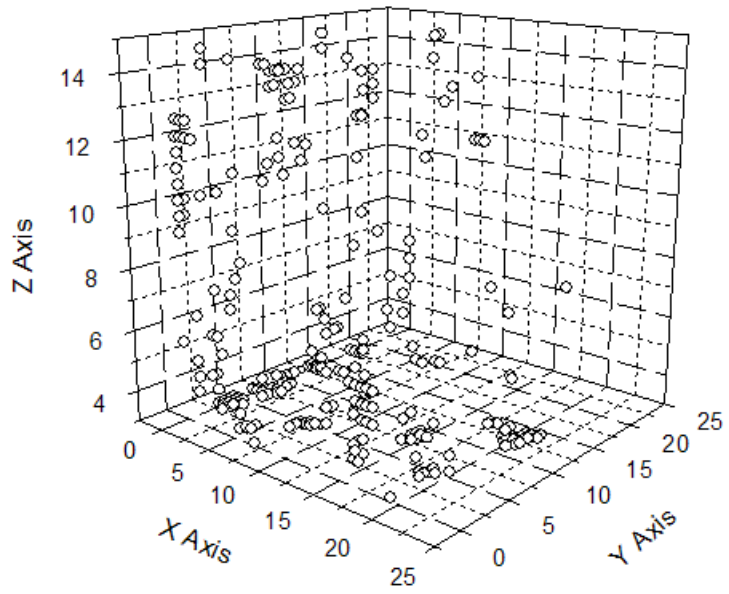

250k

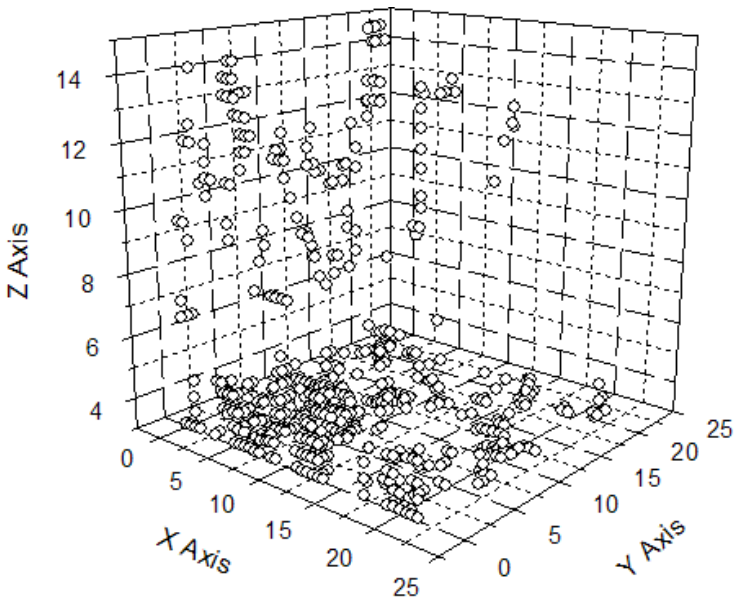

380k time step

Figure IV.7 Temperature profile in fluid phase (ε_{sf} = 0.75)

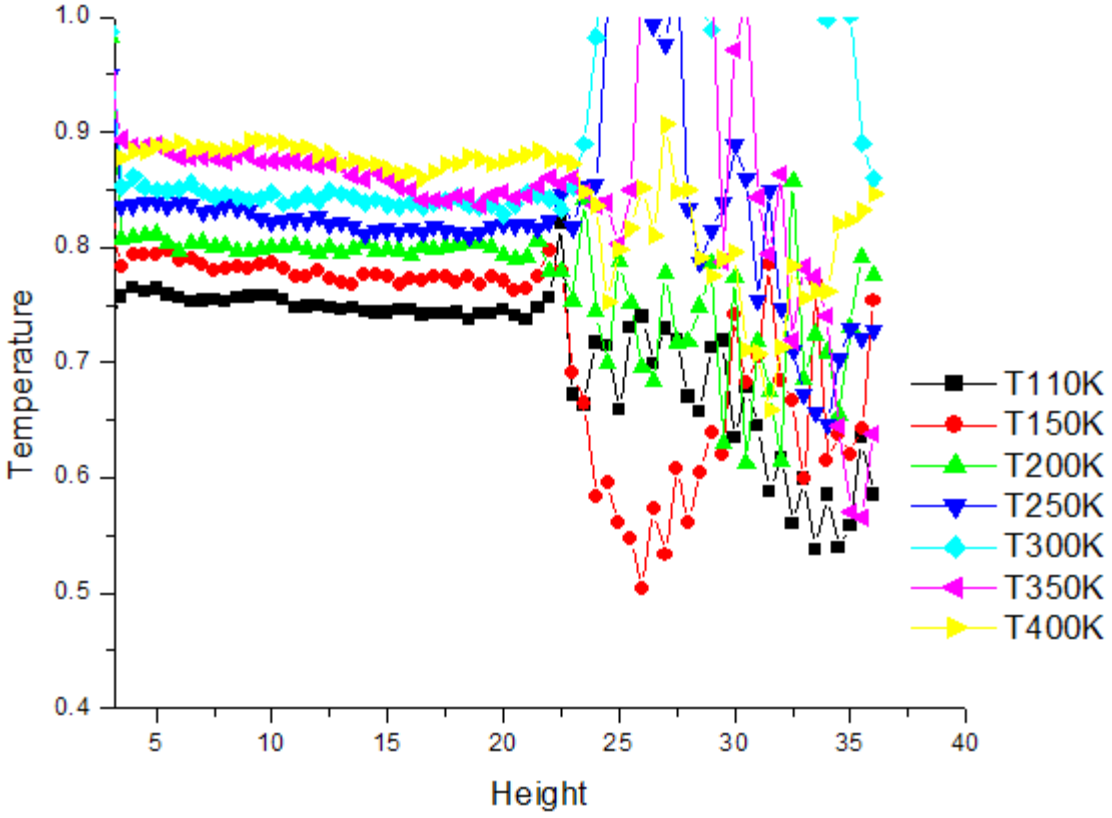

Figure IV.8 Snapshots of vapor bubble (ε_{sf} = 0.75)

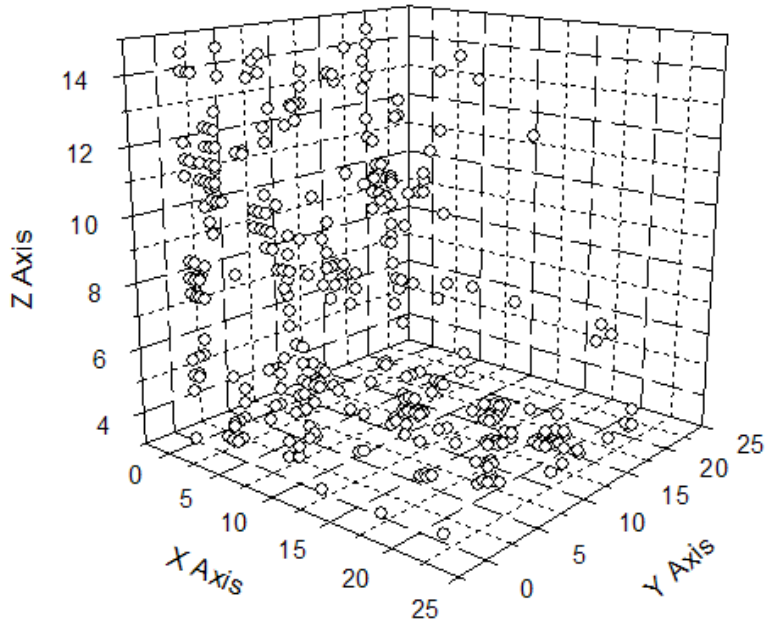

300k timestep

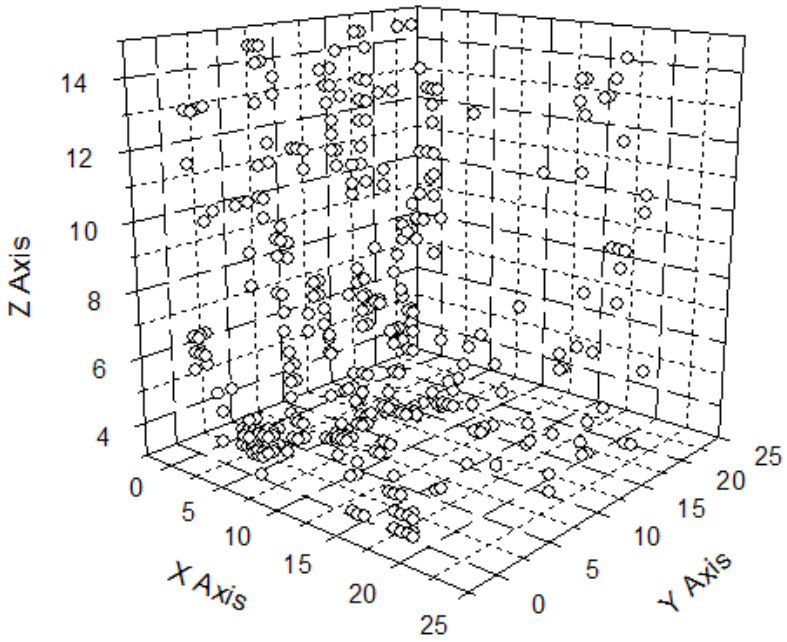

400k time step

Figure IV.9 Temperature profile in fluid phase - constant volume MD
(Large System, ε_{sf} = 0.45)

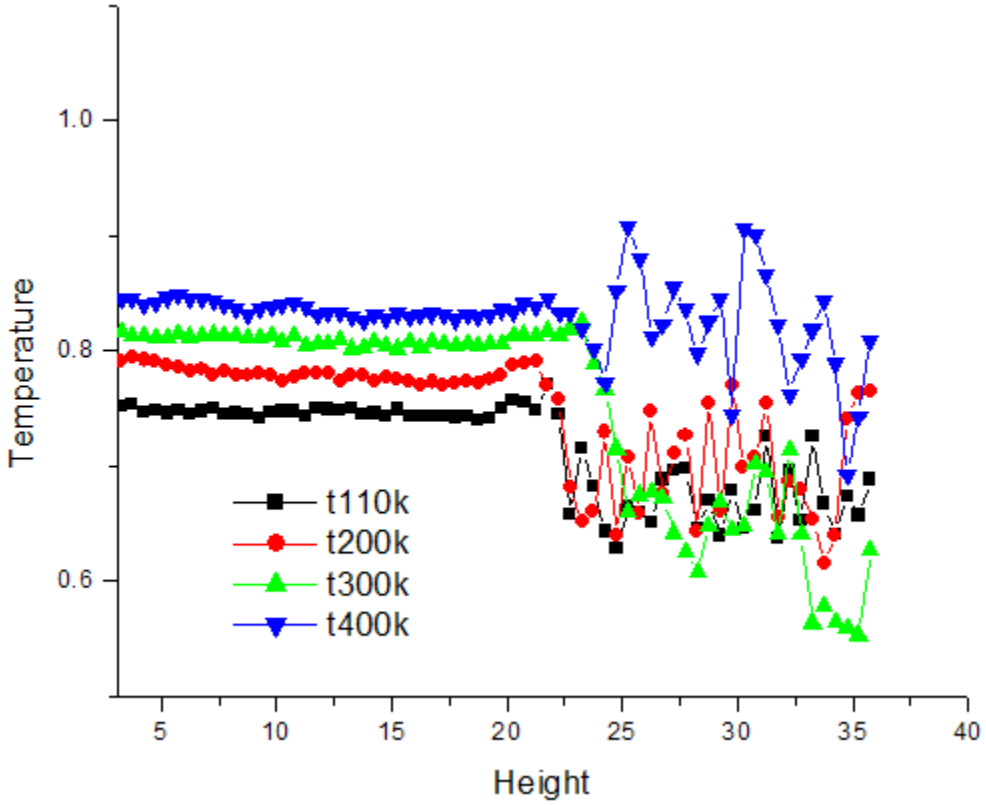

Figure IV.10 Vapor Bubble Nucleation and Growth - Const Volume MD
(Large system, ε_{sf} =0.45)

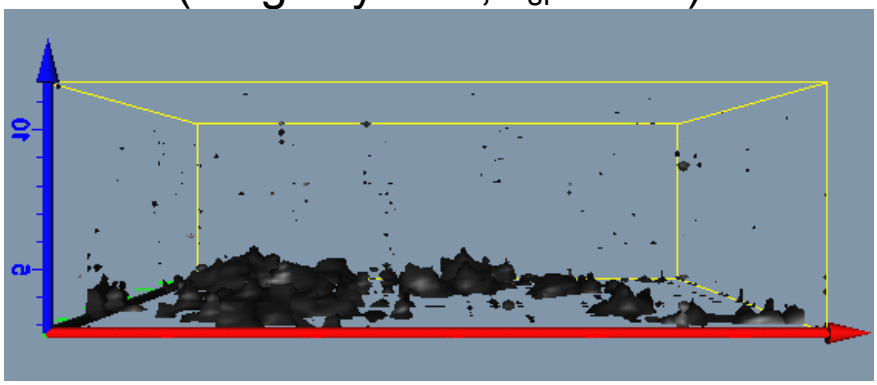

250k time step

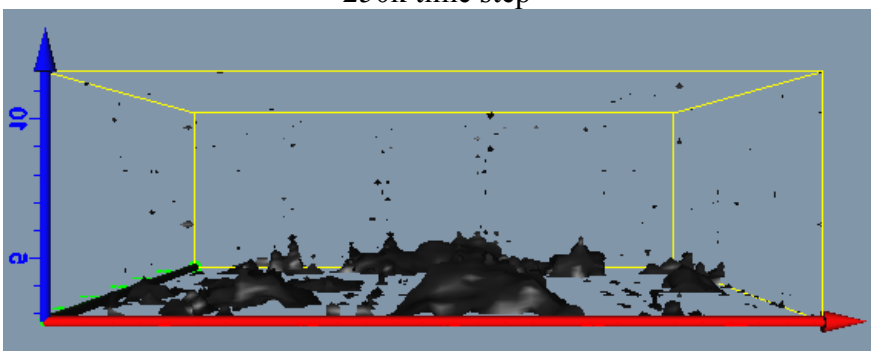

300k time step

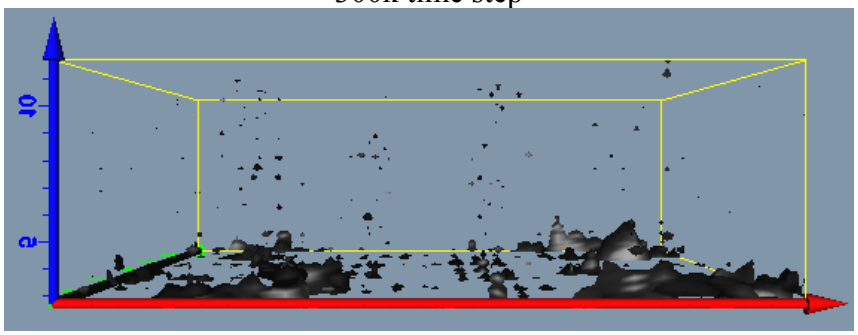

350k time step

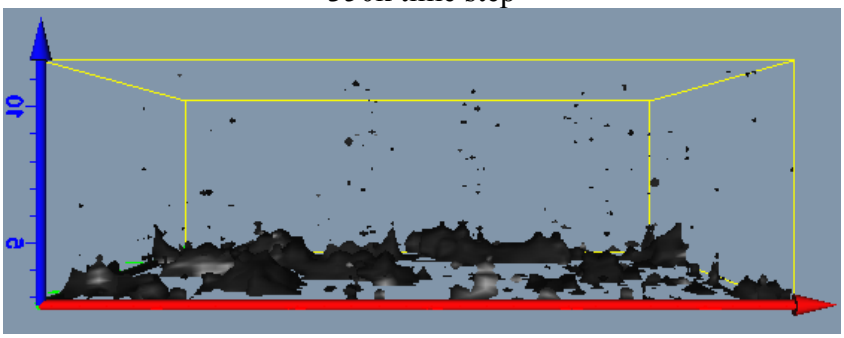

400k time step

Figure IV.11 Temperature Profile in fluid phase ($g=0.0005, \varepsilon_{sf}=0.45, T_S=1.1$)

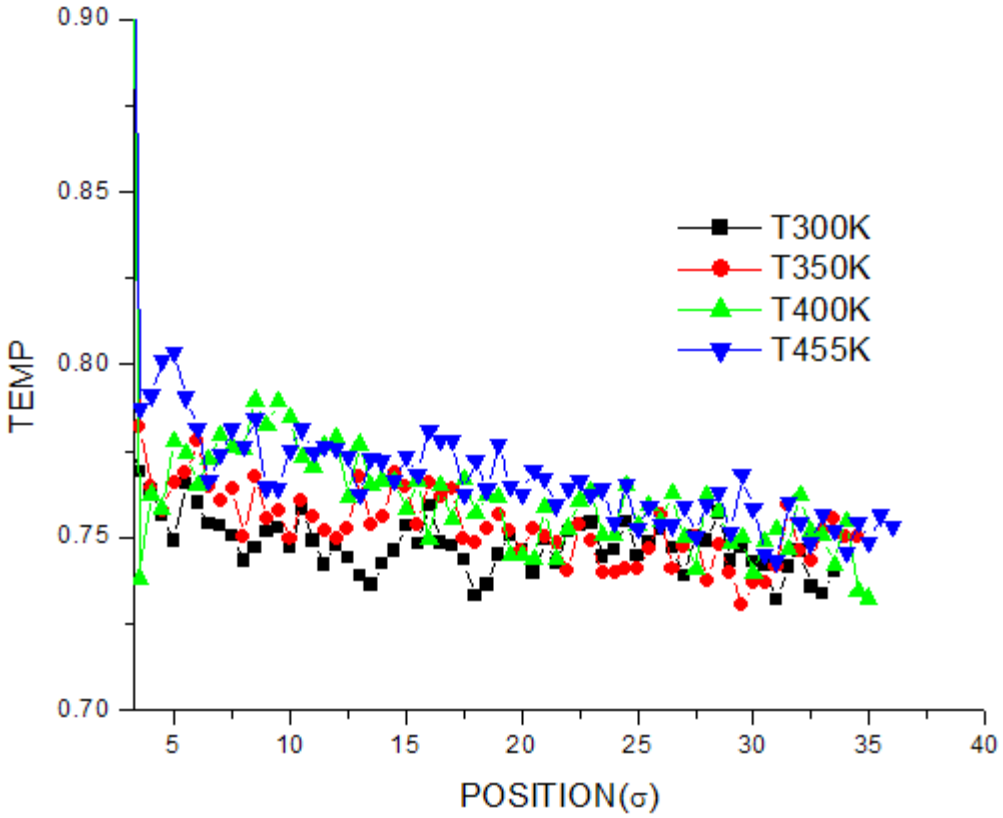

Figure IV.12 Visualization of vapor nuclei - constant pressure MD

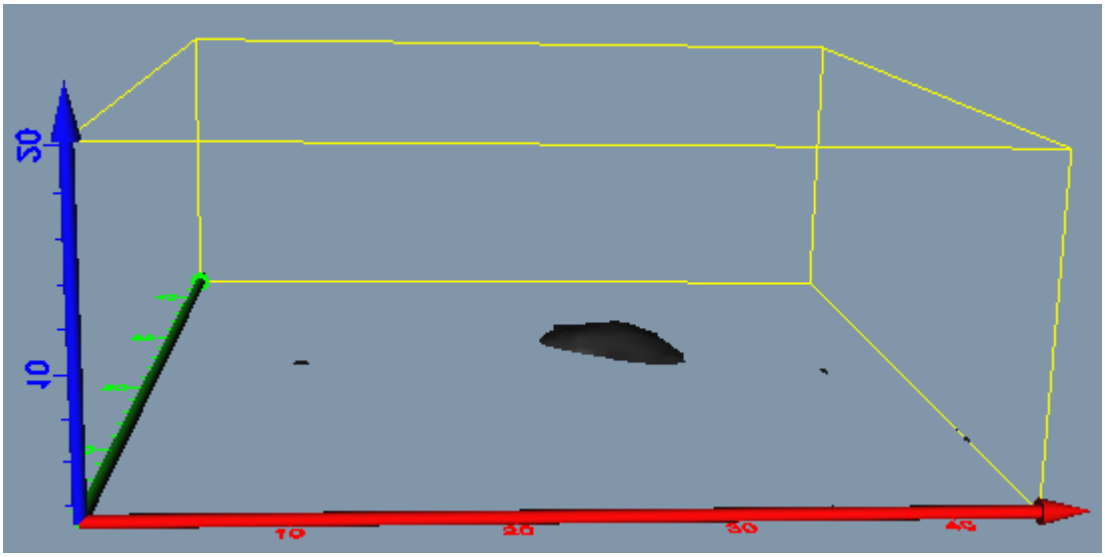

Figure IV.13 Vapor bubble nucleation and growth - constant pressure MD

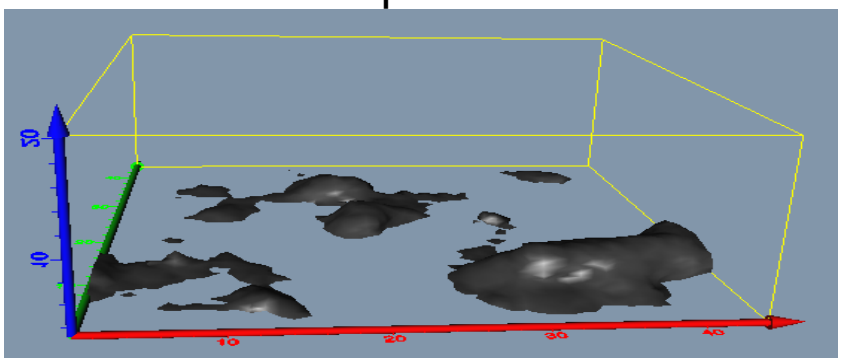

140k time step

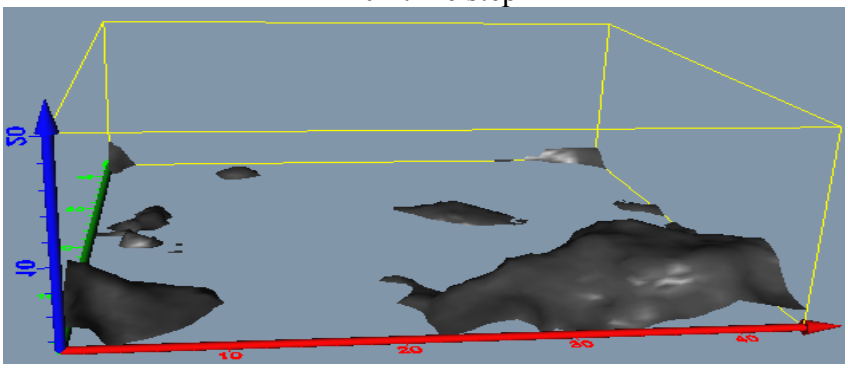

180k time step

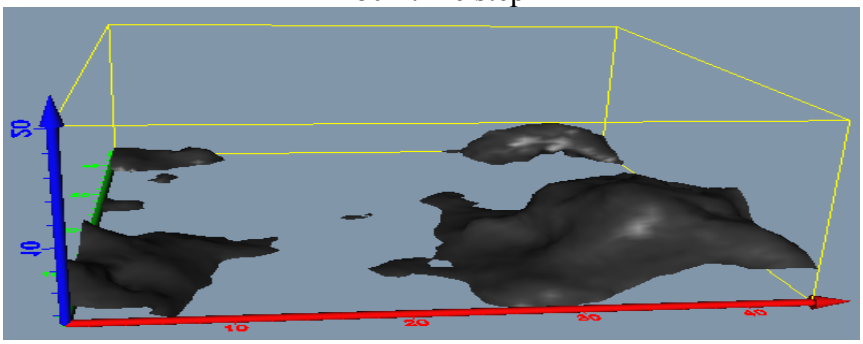

240k time step

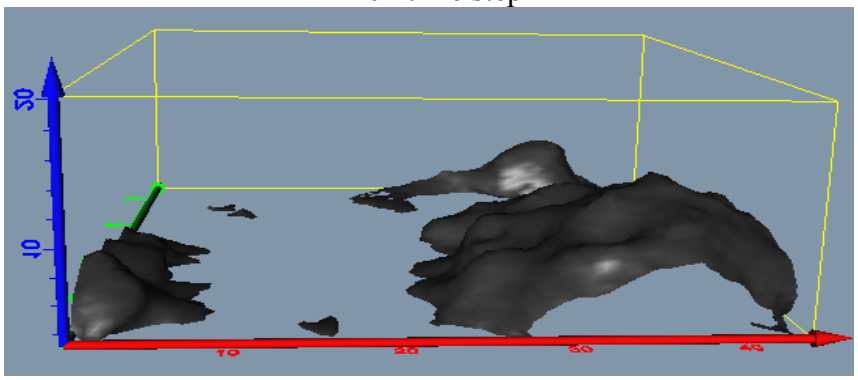

500k time step

Figure IV.14 Volume growth of stable vapor bubble on different seeds of RNG
(T_s=1.1,ε_{sf} =0.45,g=0.0005)

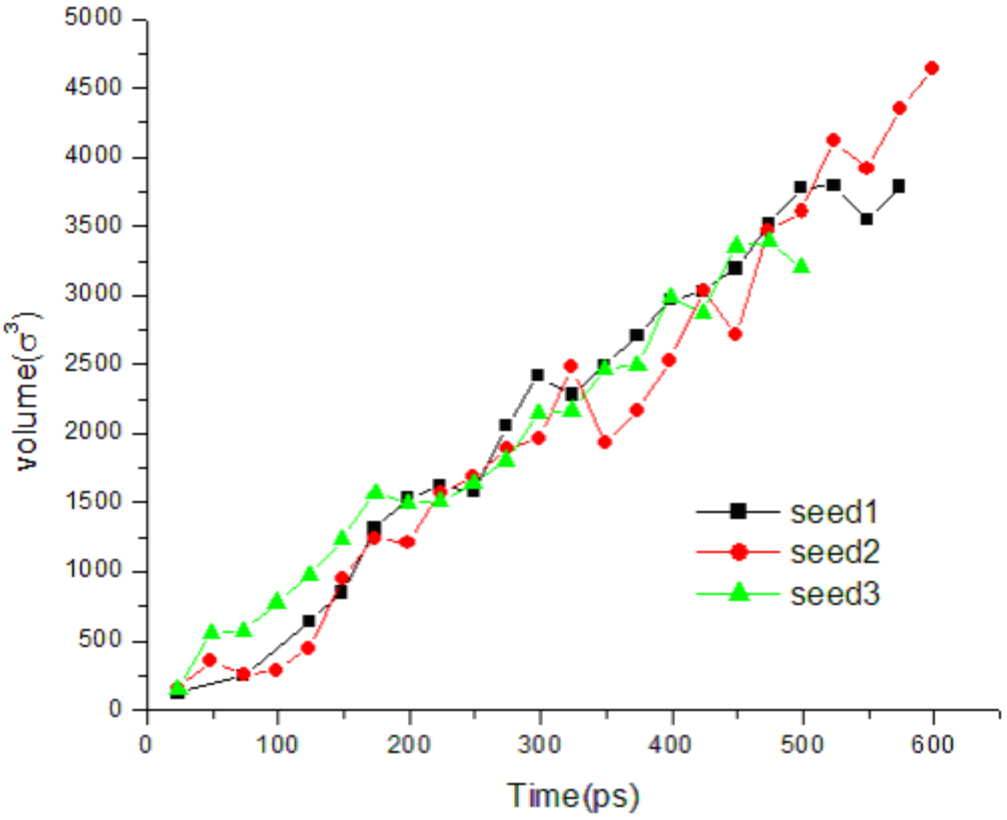

Figure IV.15 Radius of CL Vs Radius of bubble on different seeds of RNG
(T_s=1.1,ε_{sf} =0.45,g=0.0005)

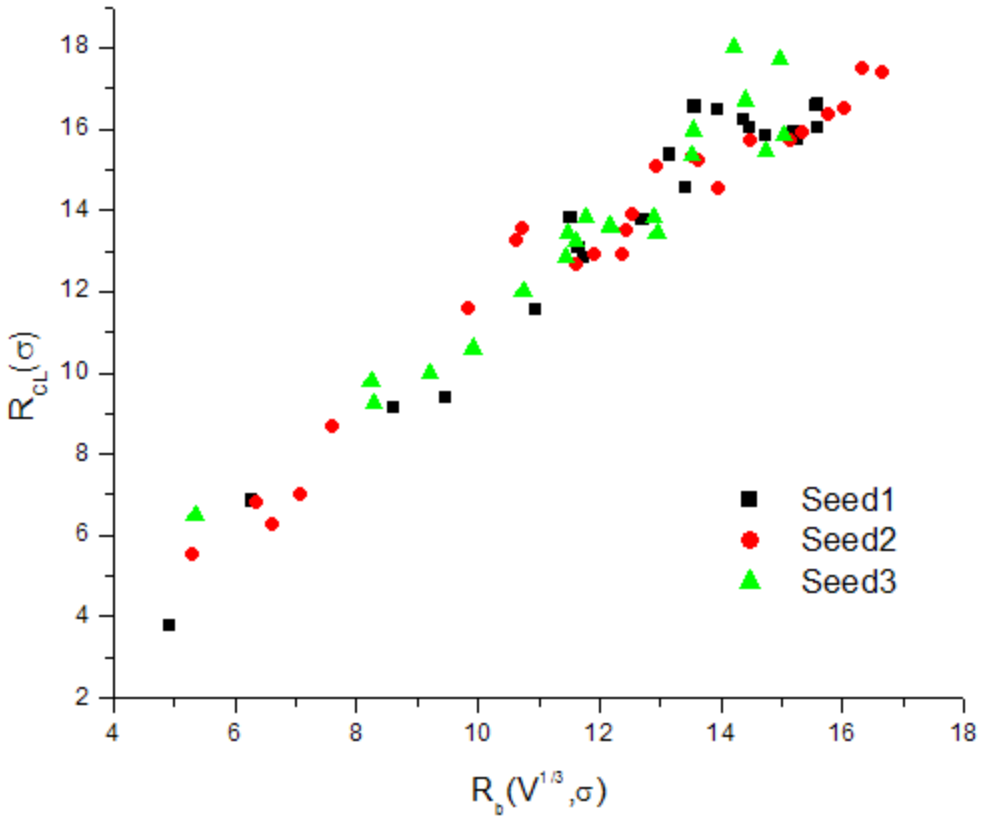

Figure IV.16 Variation of contact angle of bubble on different seeds of RNG
(T_s=1.1,ε_{sf} =0.45,g=0.0005)

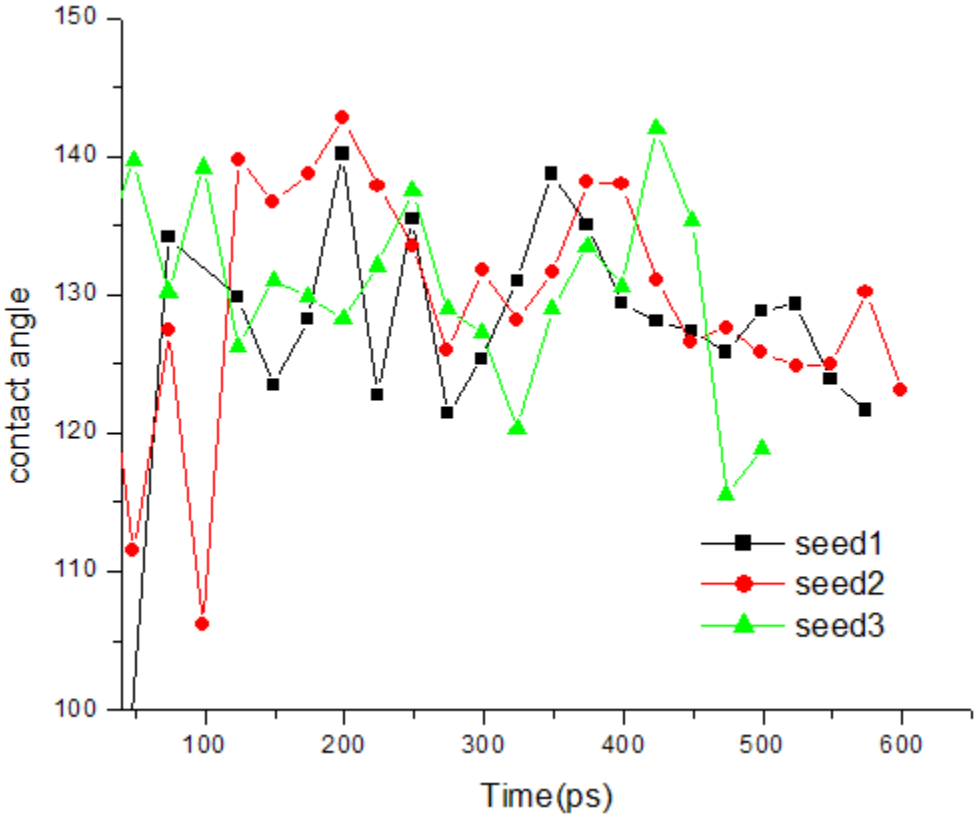

Figure IV.17 Bond number Vs bubble growth time (T_s=1.1,ε_{sf} =0.45,g=0.0005)

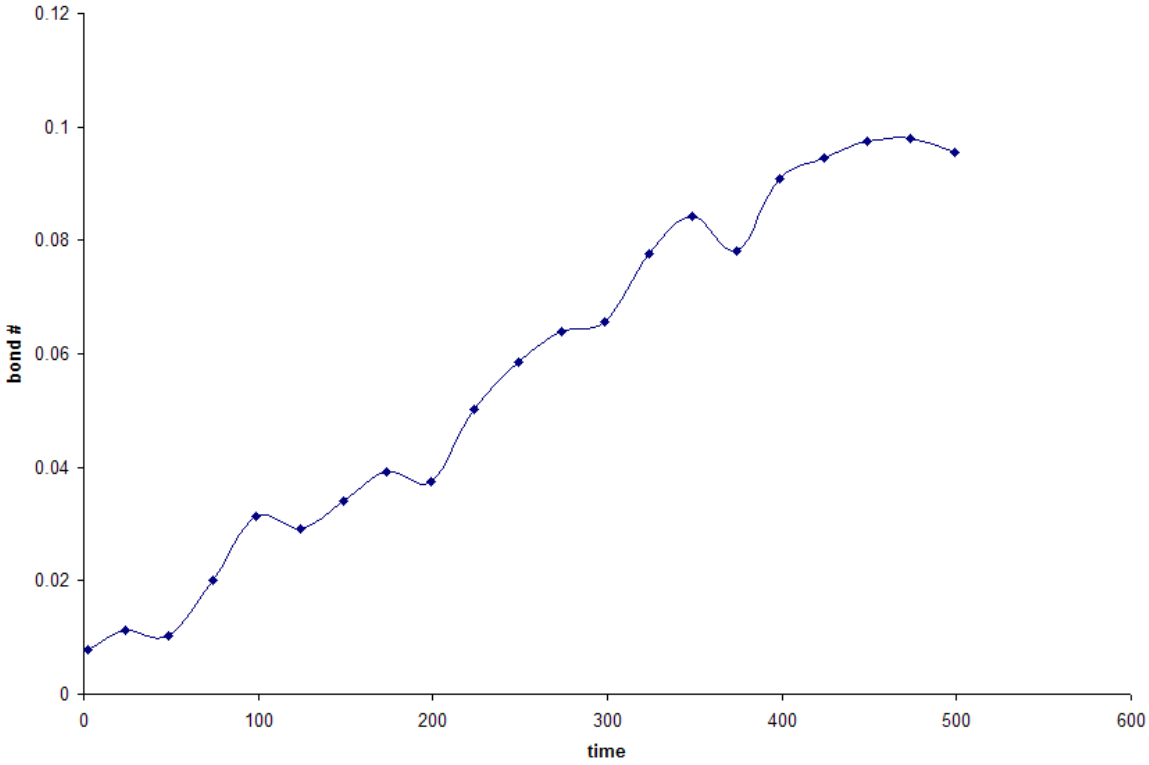

Figure IV.18 Temperature profile with different ε_{sf}

(a) ε_{sf} =0.5

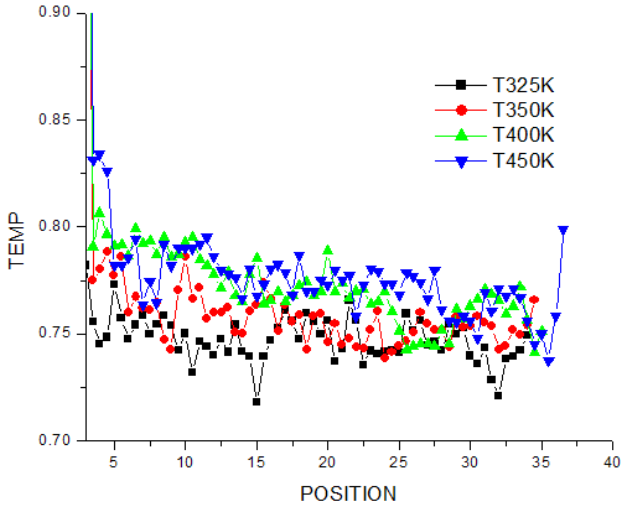

(b) ε_{sf} =0.6

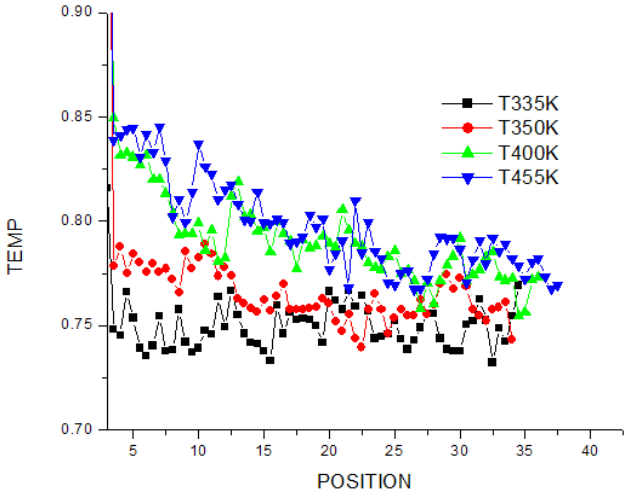

(c) ε_{sf} =0.75

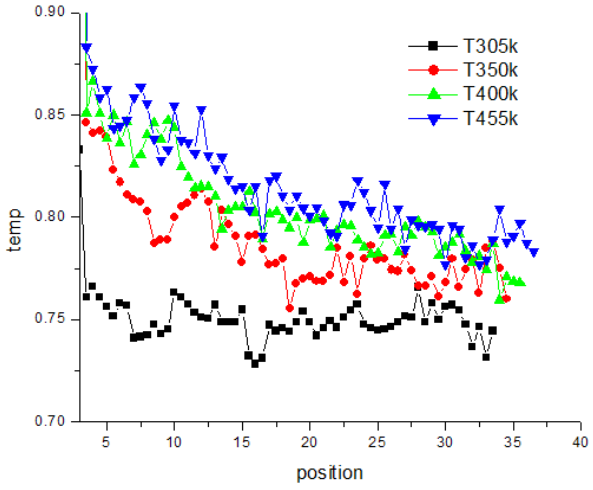

Figure IV.19 Vapor bubble Nucleation and Growth (ε_{sf} =0.6, T_s =1.1, g=0.005)

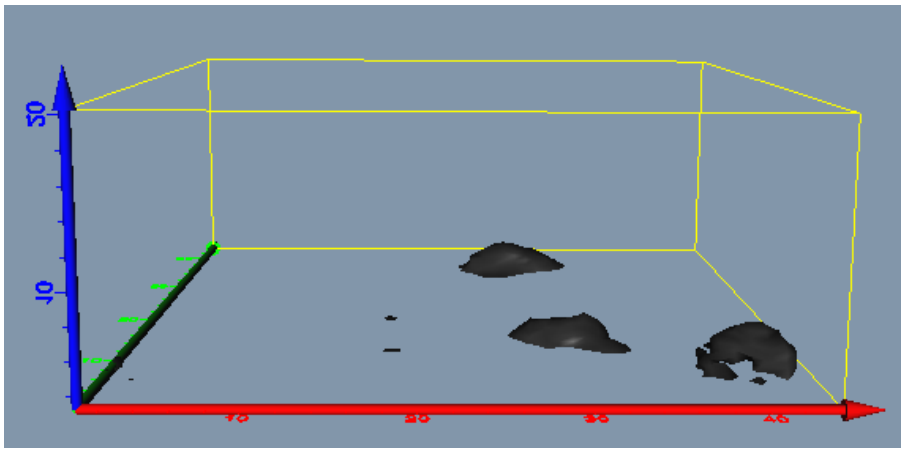

340k time step

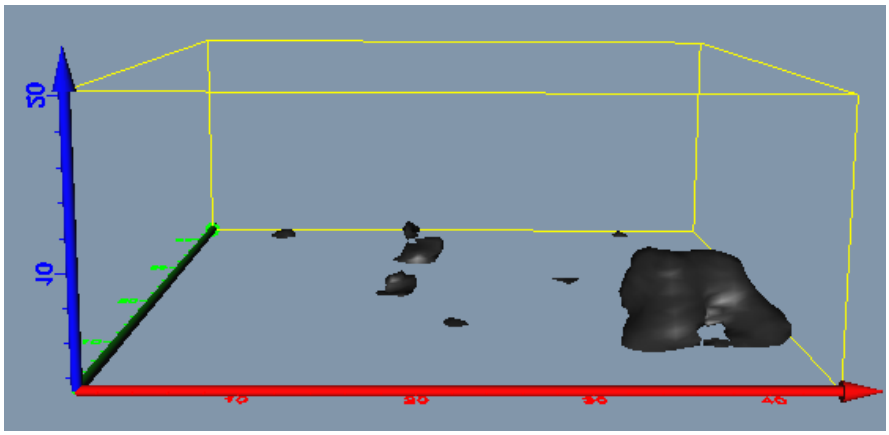

350k time step

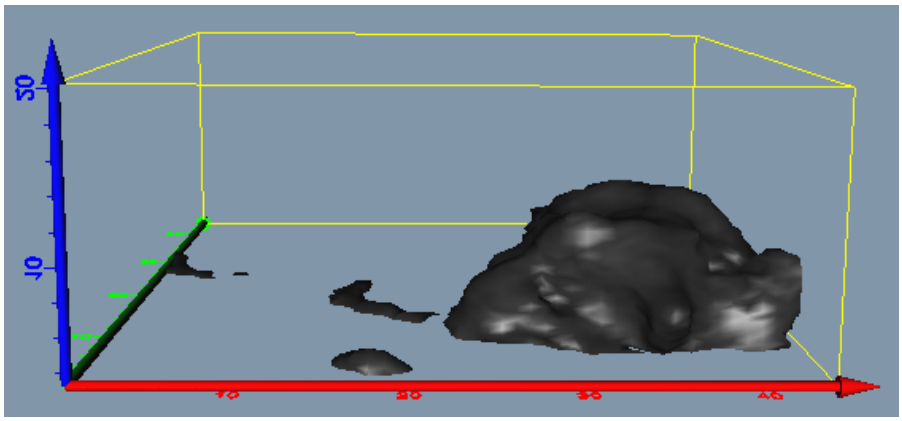

380k time step

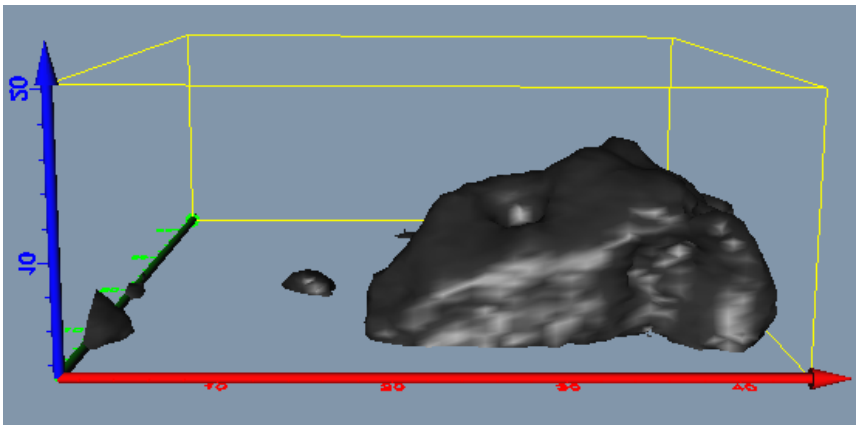

410k time step

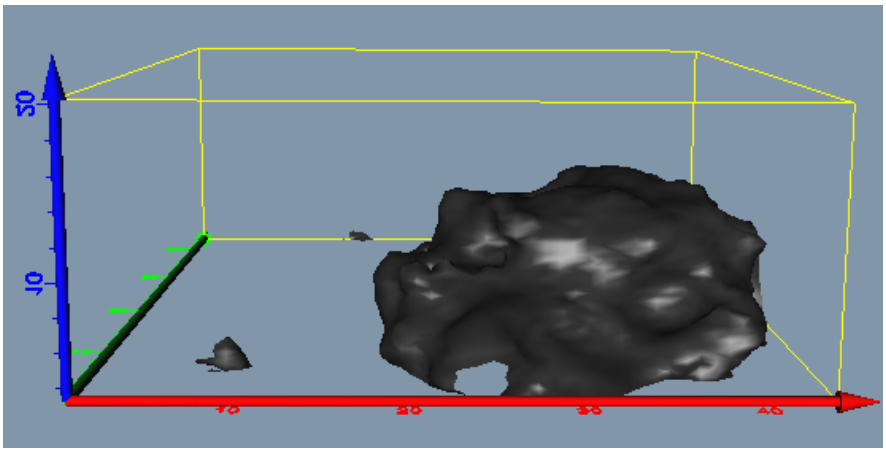

430k time step

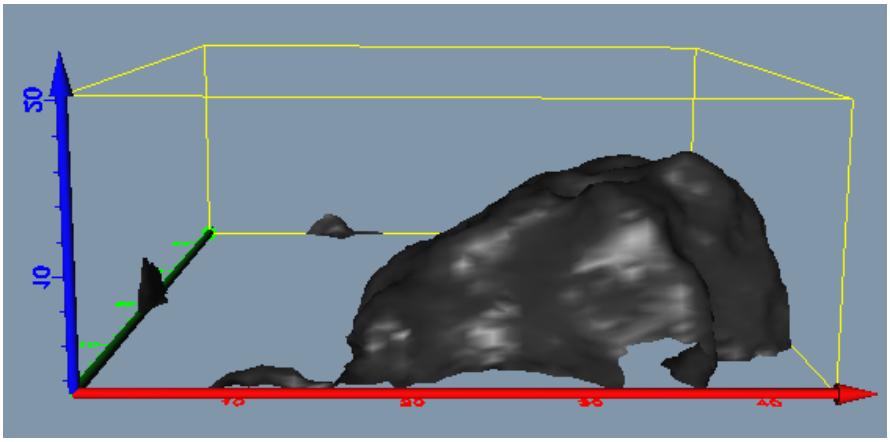

455k time step

Figure IV.20 Vapor bubble nucleation and growth (ε_{sf} =0.6,T_s=1.1, g=0.0015)

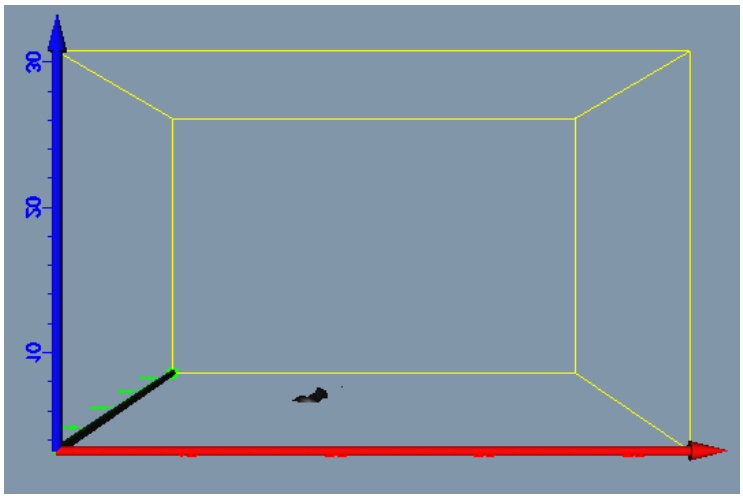

340k time step

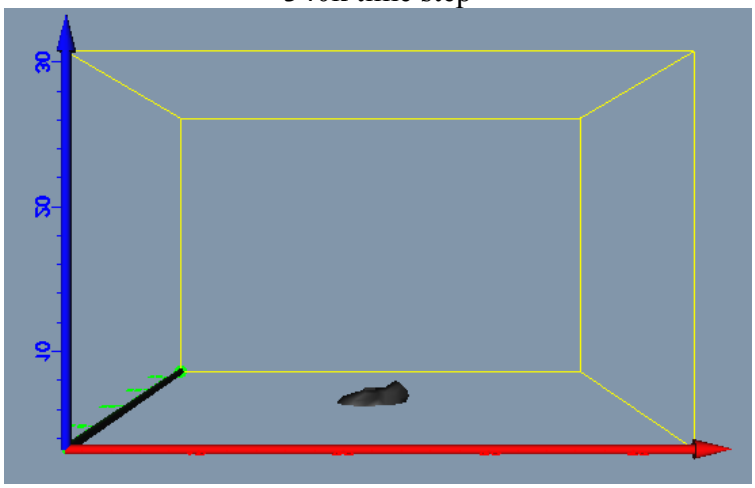

350k time step

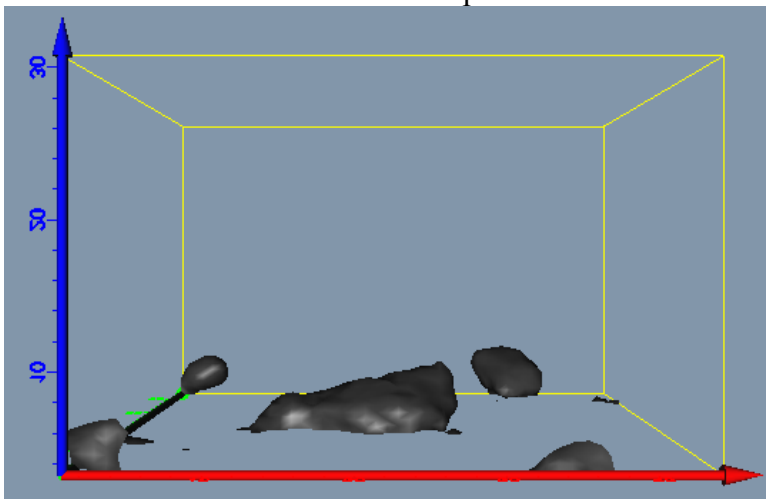

370k time step

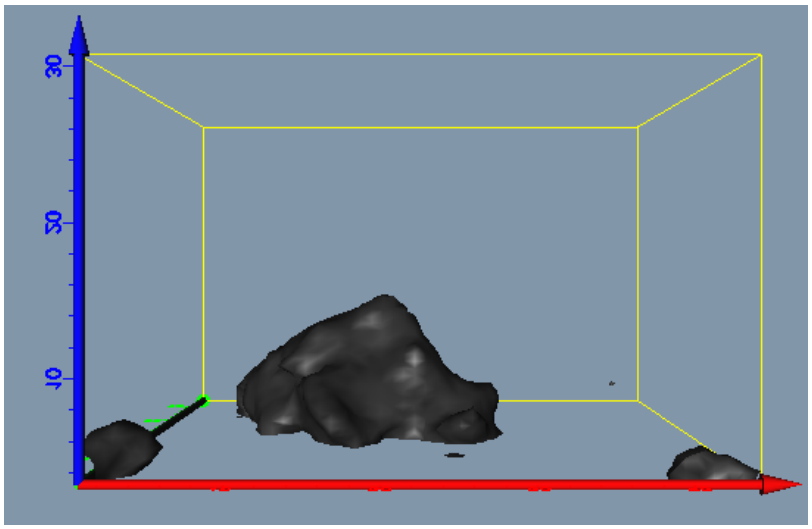

400k time step

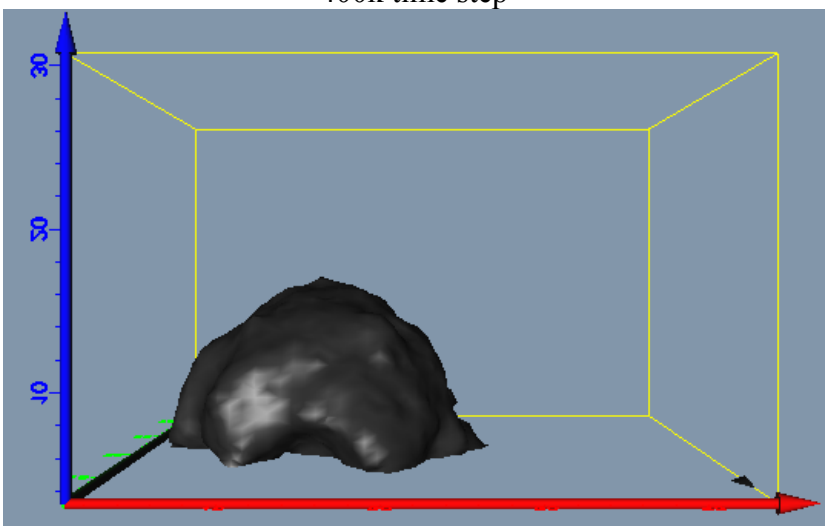

425k time step

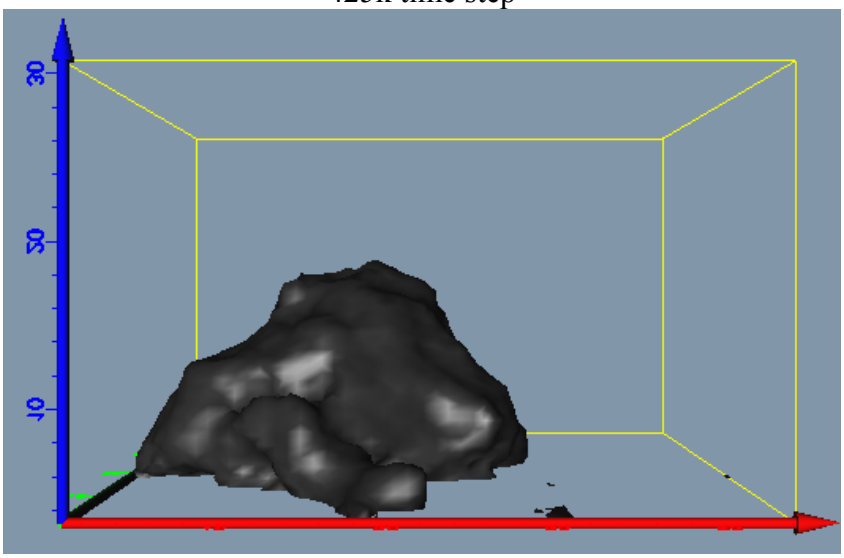

455k time step

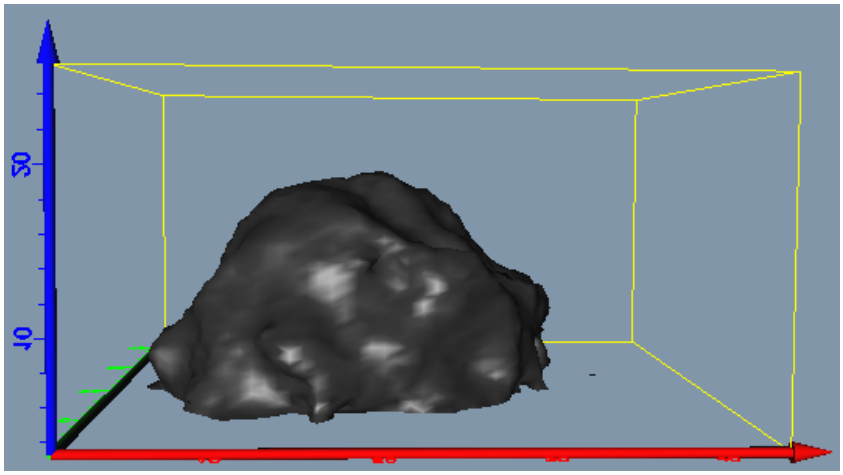

500k time step

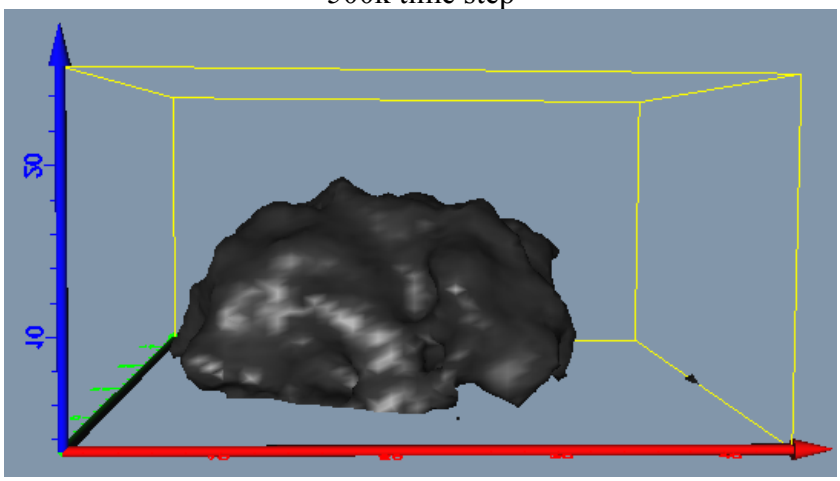

535k time step

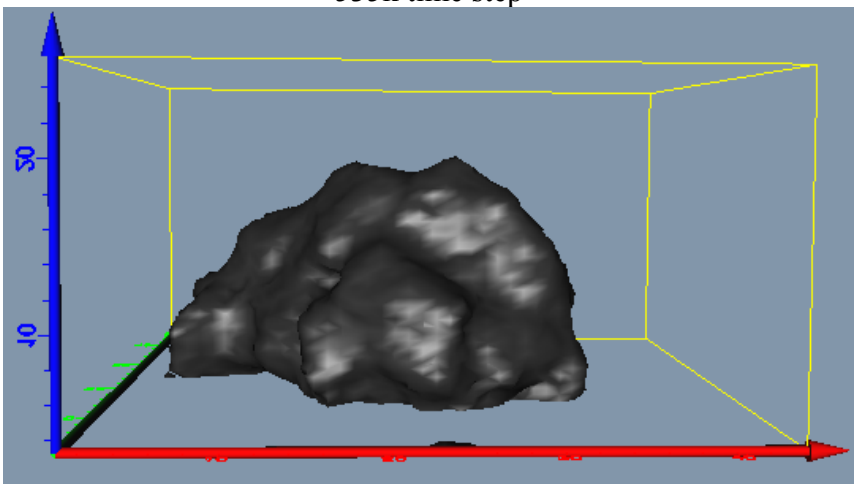

555k time step

Figure IV.21 Temperature Profile in liquid phase (ε_{sf} =0.6,T_s=1.1, g=0.0015)

(a)

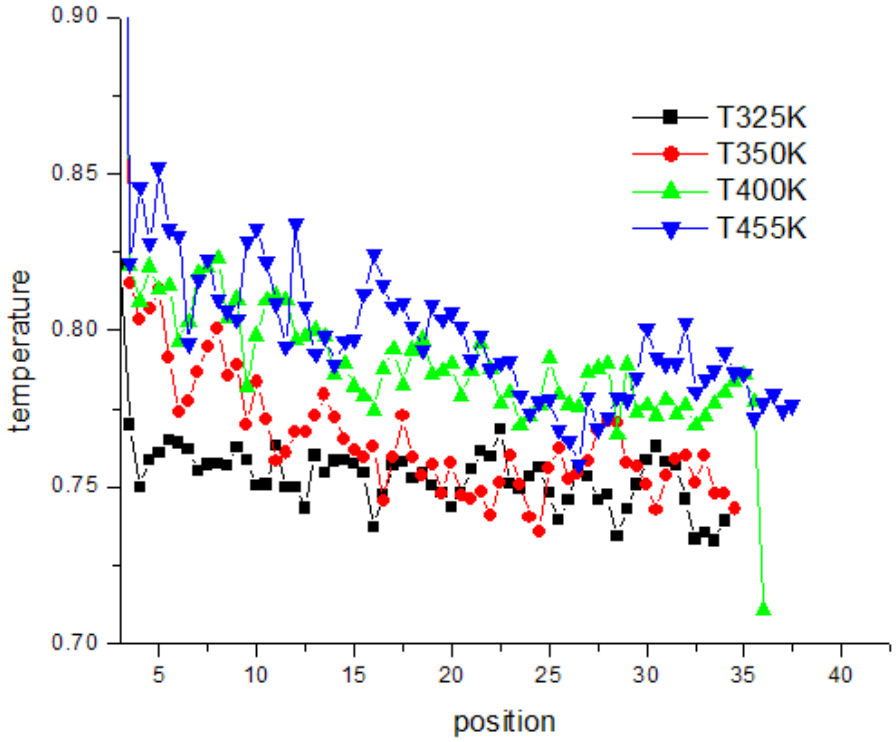

(b)

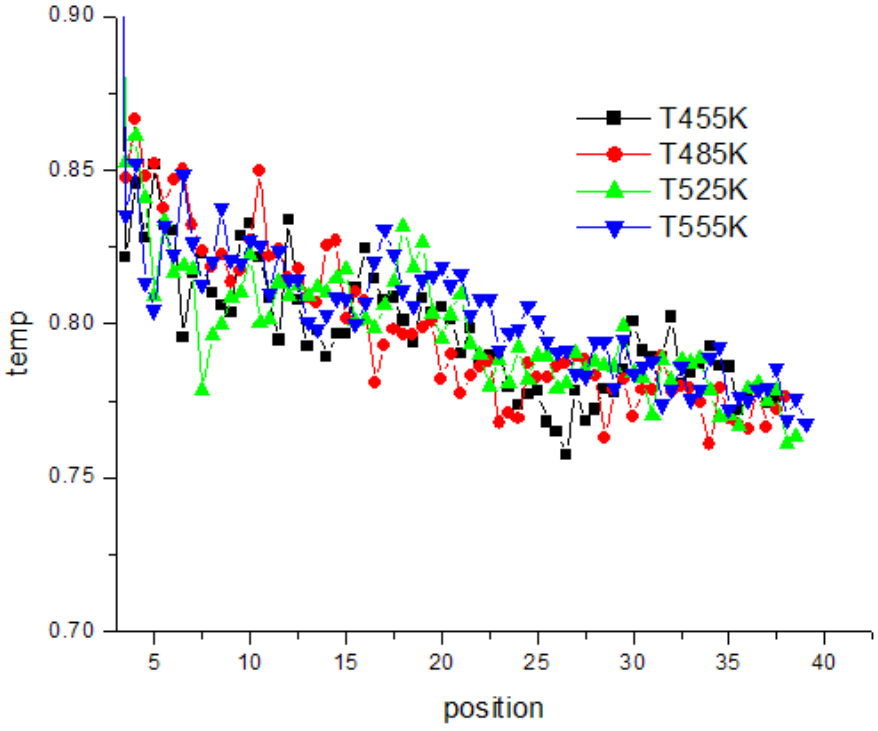

Figure IV.22 Time evolution of vapor bubble growth

(After 455k time step, g change from 0.0015 to 0.015 in 80k time step interval)

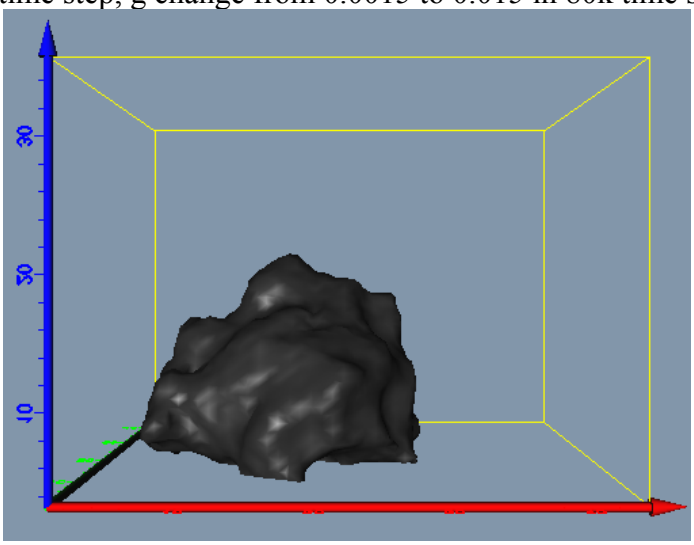

480k time step

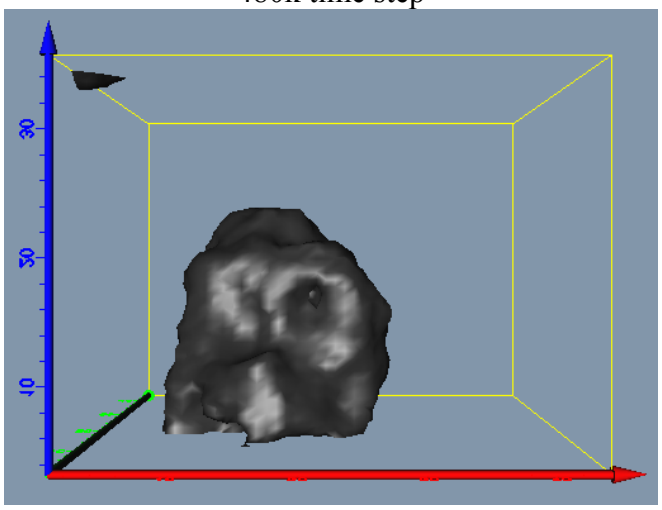

495k time step

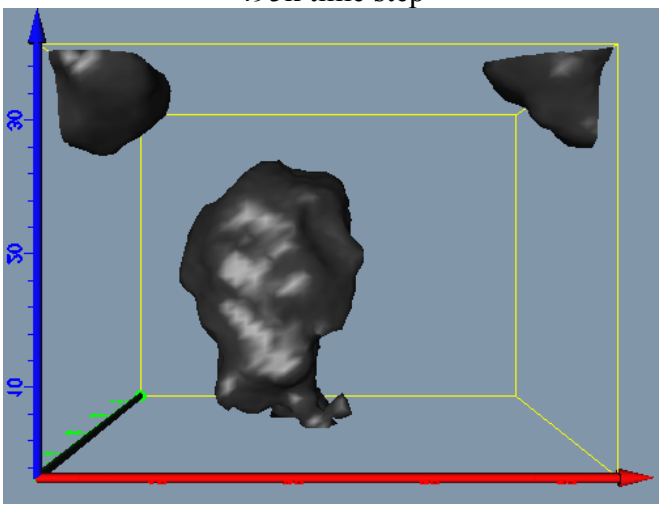

505.5k time step

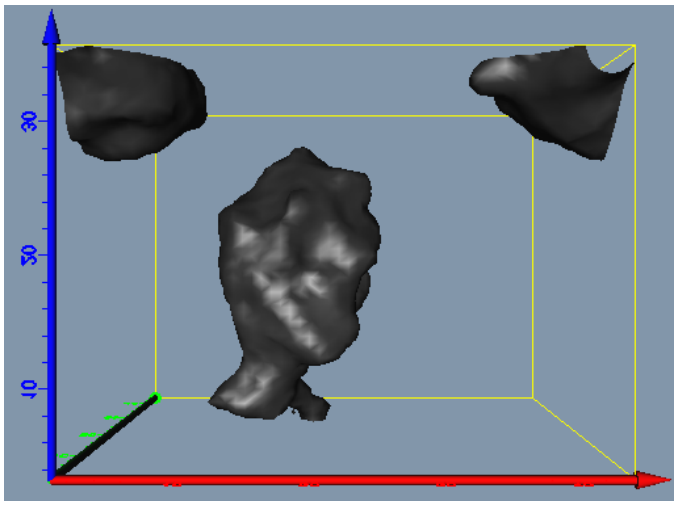

507.5k time step

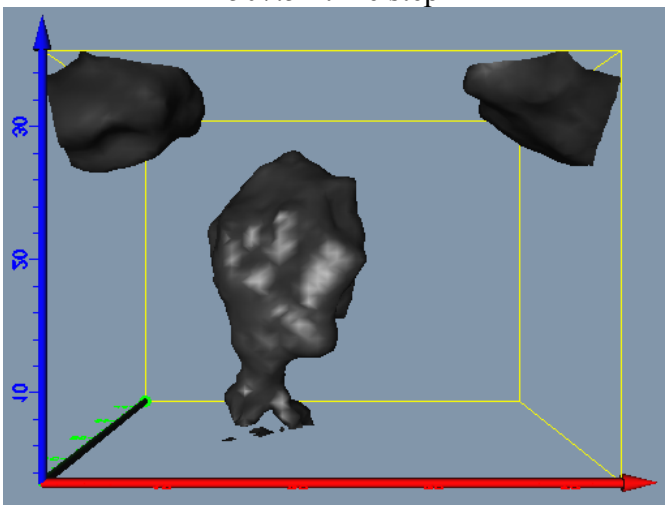

508k time step

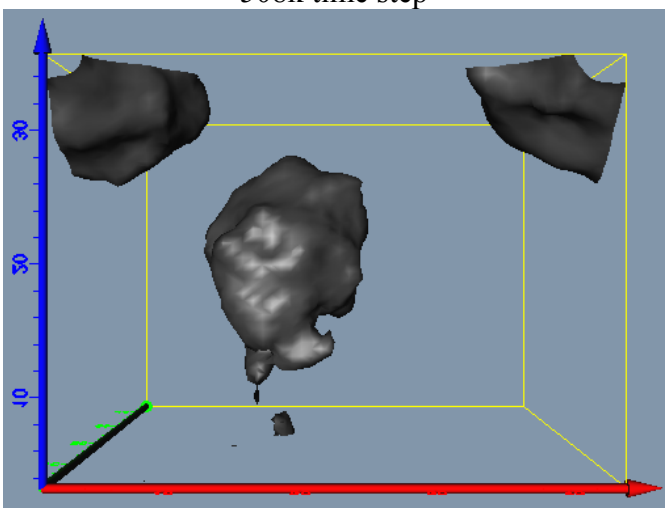

508.5k time step

Figure IV.23 Temperature Profile after gravity adjustment

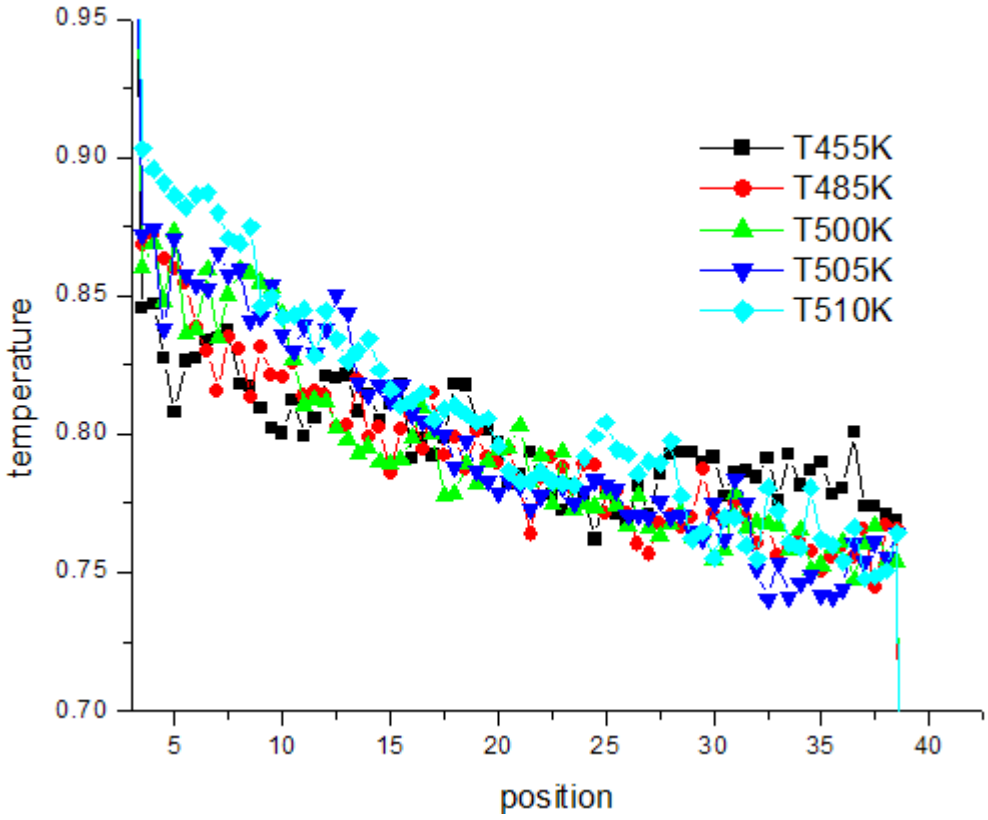

Figure IV.24 Time evolution of CL radius (g=0.0075)

(a) MD simulation

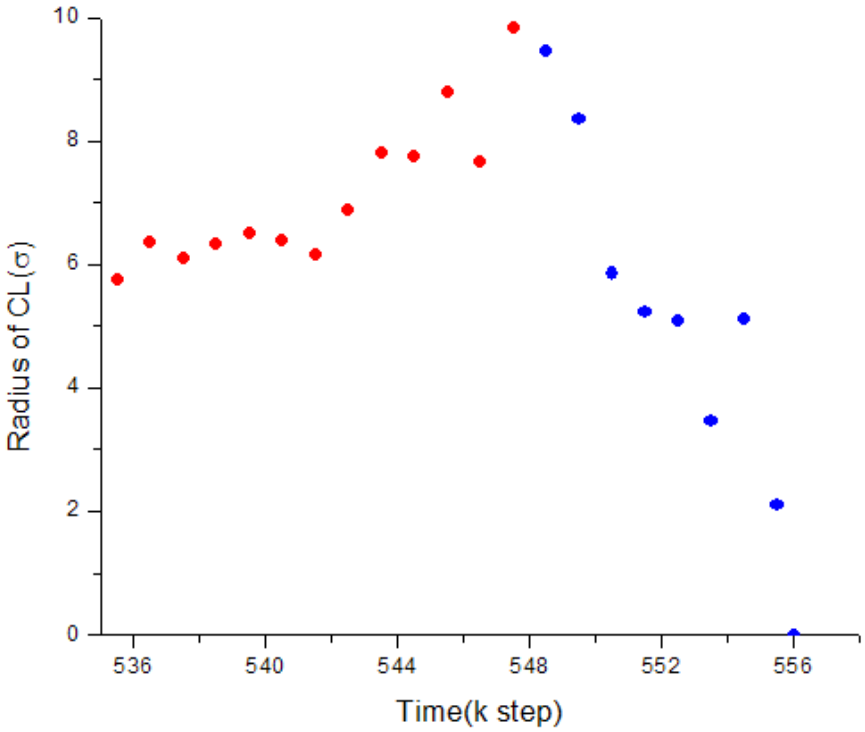

(b) Experimental data from S. Gong and W. Ma

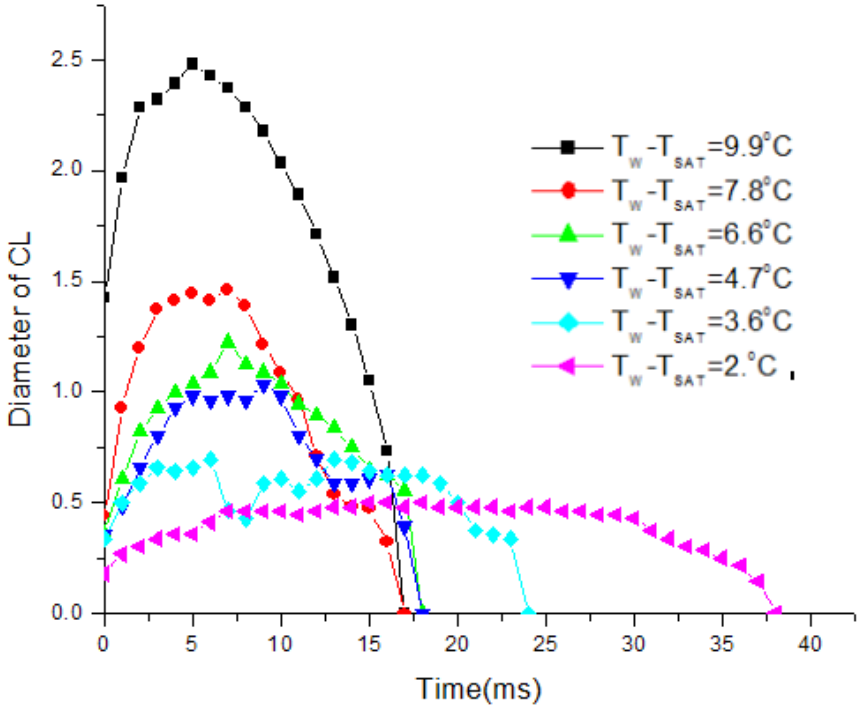

Figure IV.25 Time evolution of bubble volume (g=0.0075)

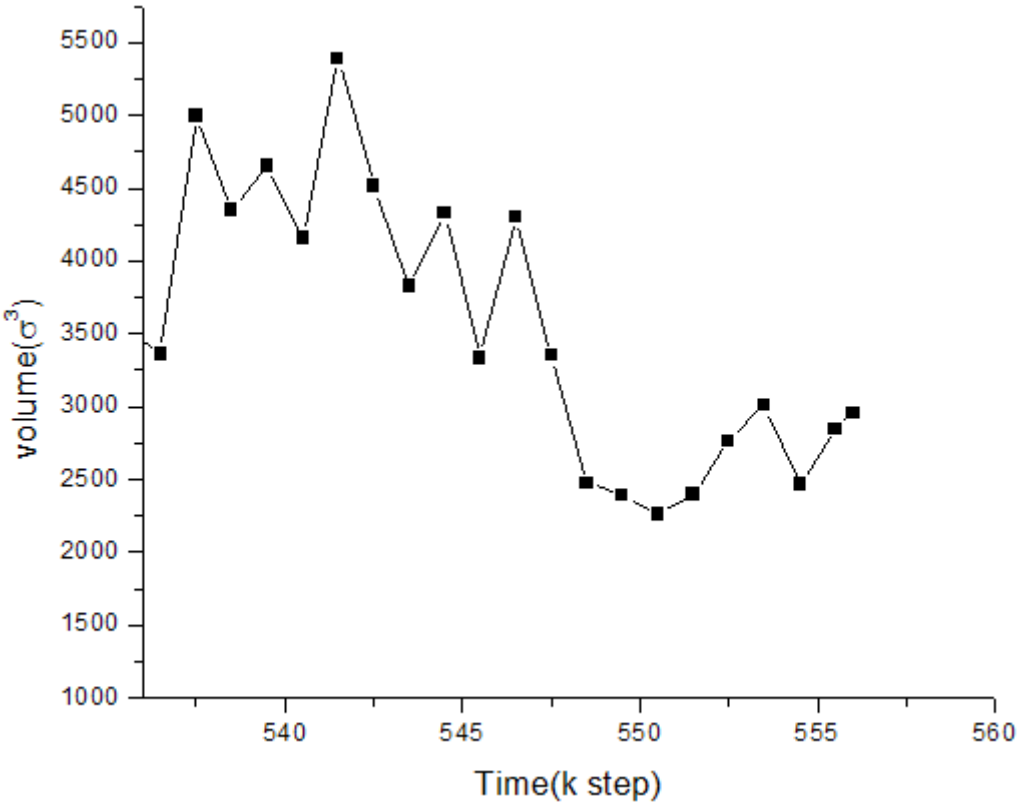

Figure IV.26 Solid Temperature

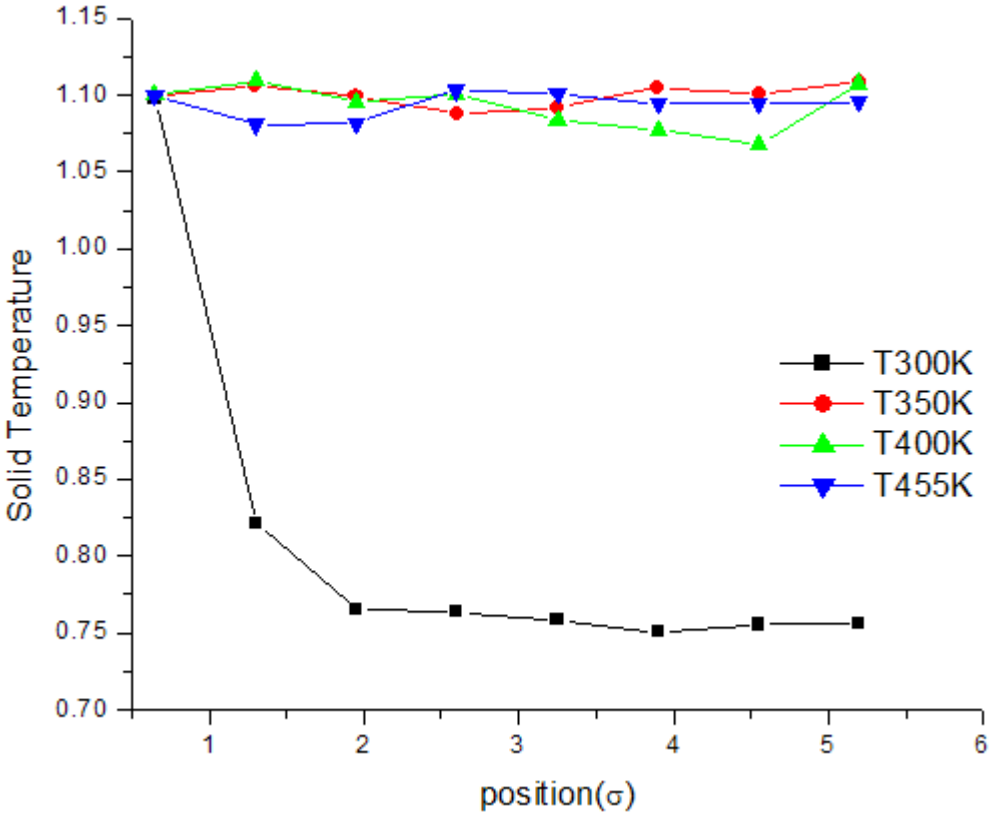

Figure IV.27 2D Local temperature profile on solid-liquid “interface”

(above black line:400k time step; under black line:455k time step)

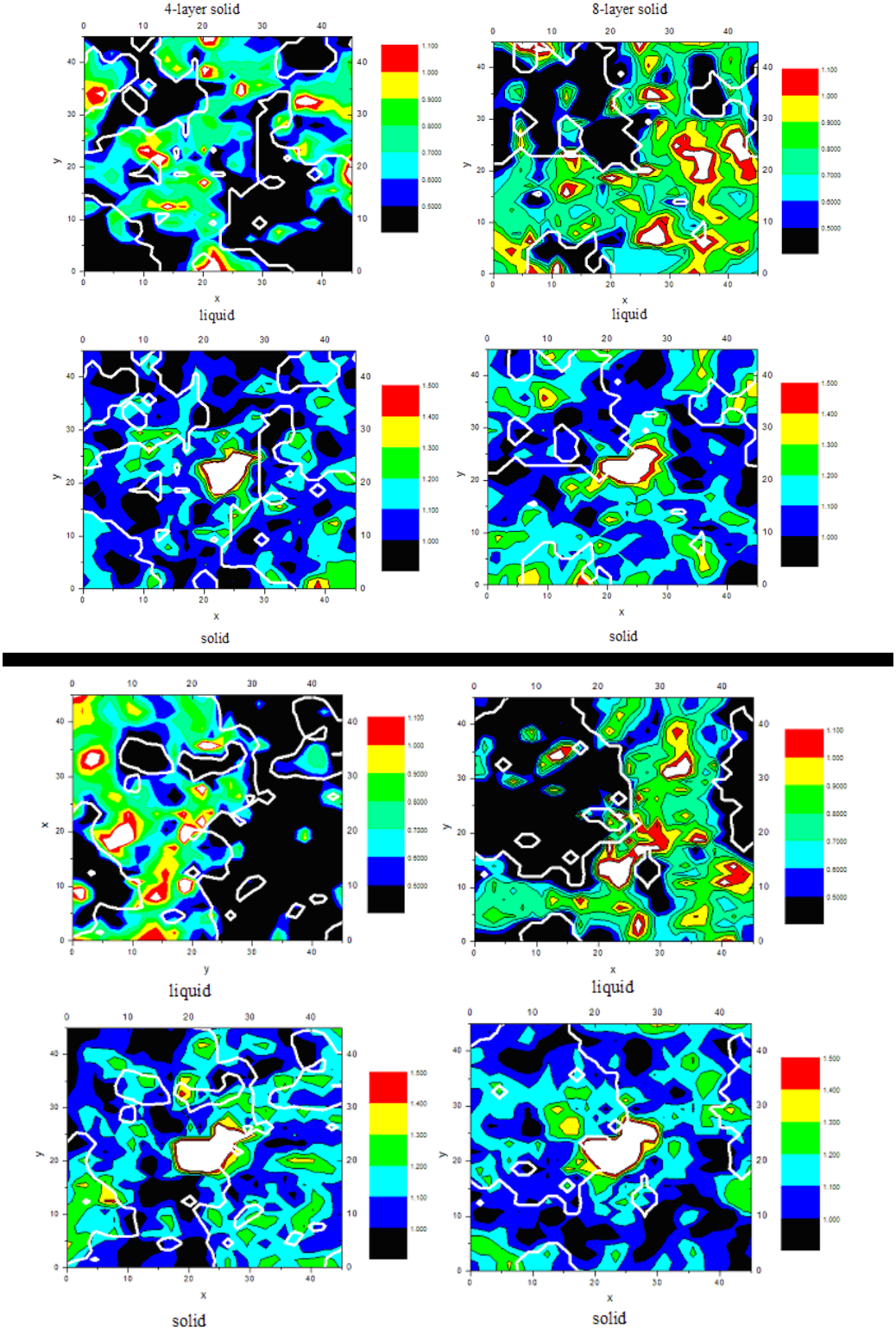

Figure IV.28 Vapor Bubble Growth on walls with different thickness

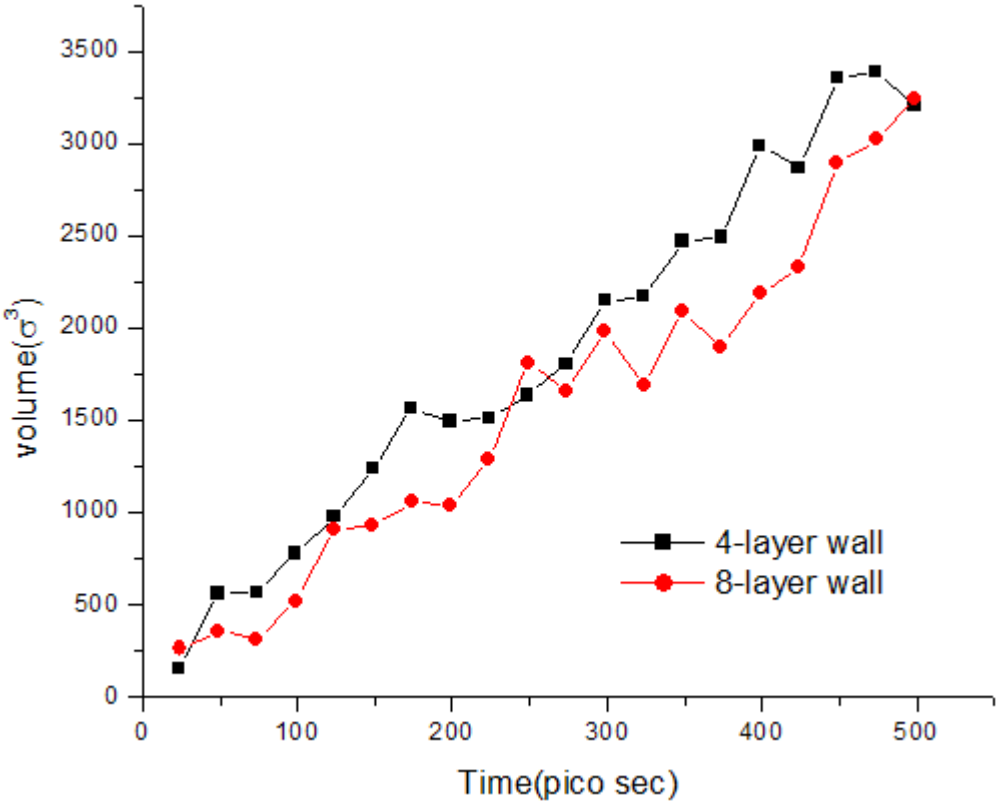

Figure IV.29 Vapor bubble growth with time for different T_s

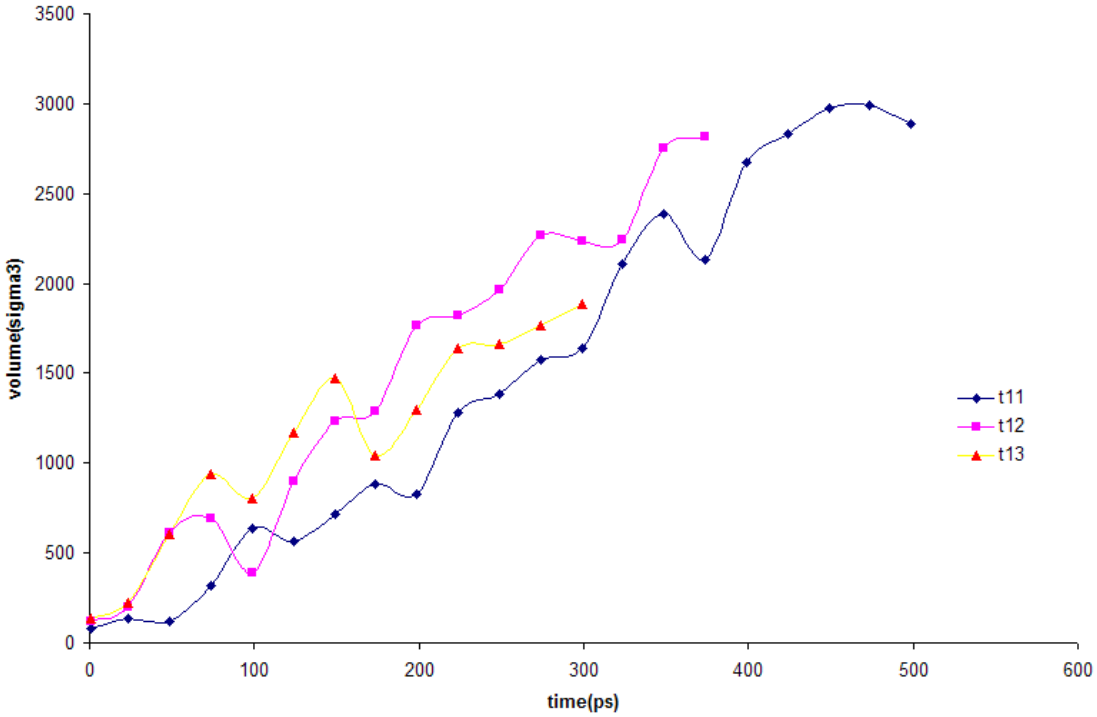

Figure IV.30 Time evolution of vapor bubble growth

(Temperature at the top wall is set to 0.8 after 455k time steps)

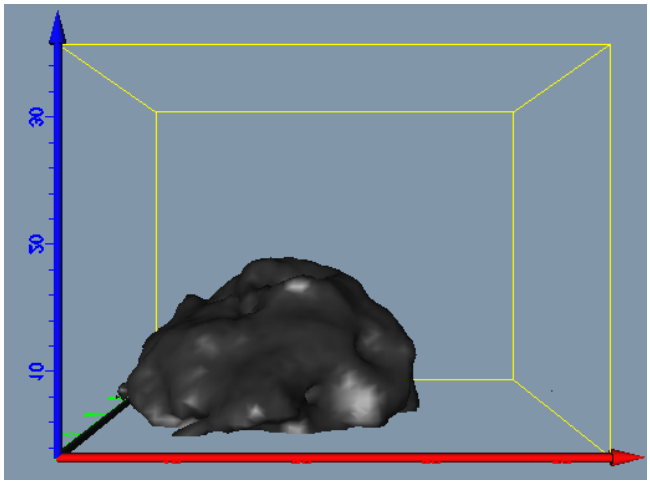

460k time step

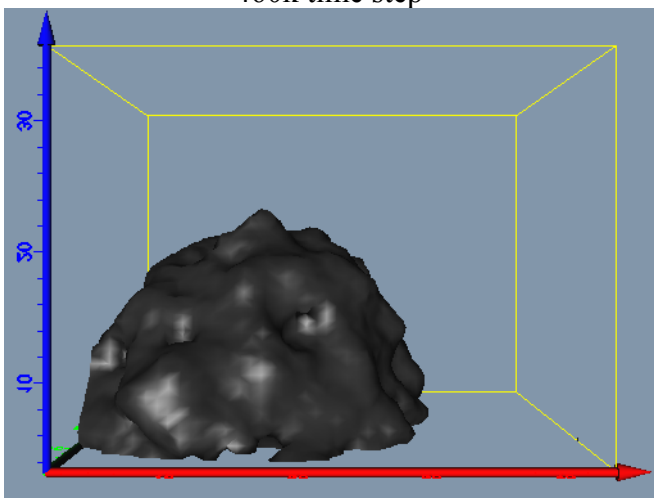

520k time step

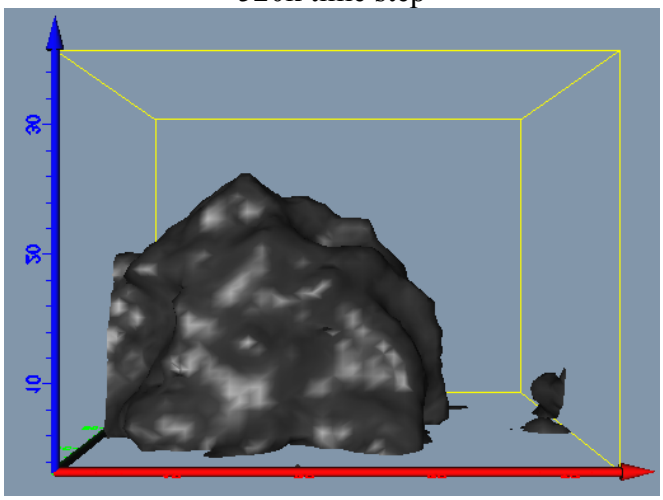

565k time step

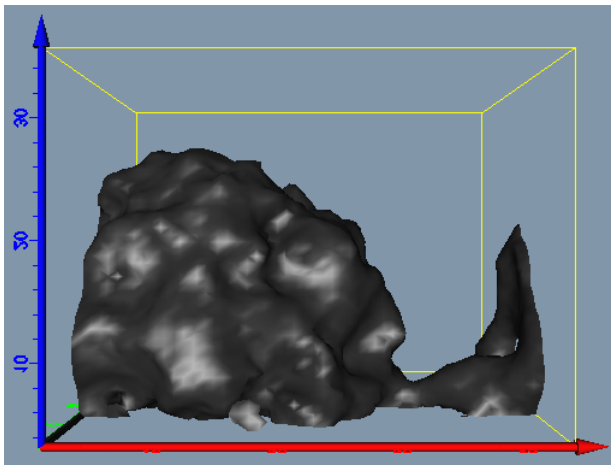

610k time step

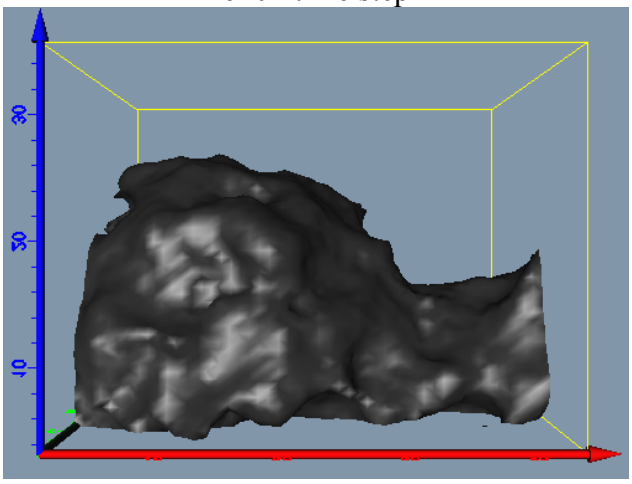

635k time step

CONCLUSIONS

Nucleate boiling has gained considerable attention since the 1930s due to the potential of enormous, stable heat flux that it offers at relatively low thermal driving forces. However, there has been significant difficulty in developing a comprehensive mechanistic understanding for its heat transfer enhancement due to its great complexity of the coupled processes of nucleating bubbles at a heating surface, tracking their growth, and accounting for bubble detachment. In this thesis, we explicitly recognize the importance of the three-phase contact line at the edge of the vapor bubble on the solid heating surface that some competing mechanisms have ignored. We first model the heat transport processes by a quasi-steady heat conduction approach without convection, for the growth and detachment of a single bubble at the interface of solid and liquid layers, each of finite thickness under small Reynolds, Peclet, Capillary and Bond numbers. This continuum model approach requires as an input to find the time dependence of the growth and detachment of a vapor bubble from the solid heating surface and the resulting behavior shows significant dependence on the assumptions made about the contact line motion. For various CL motion assumptions, though, before bubble deformation from its section of a sphere shape (when the bubble is small enough so that its $Bo<<1$), the calculated bubble volume grows as time to the 3/2; In contrast, when $Bo\sim1$ and beyond, the growth of the volume of the bubble Vs time is very sensitive to contact line motion assumptions. Unfortunately, the motion of a three-phase contact line, even in the absence of phase change, is, in general, poorly understood.

We therefore employ molecular dynamics to explore the physical behavior of the contact line as the bubble grows and as gravity starts to play a role in pulling the bubble upwards. The only inputs to the MD calculations are specifications of the molecular interactions. We use 6-12 L-J potentials for all inter-atomic interactions, and very carefully choose the parameters of these potentials so as to be able to access the processes of interest. We simulate a complete nanoscale version of our system, complete with solid and liquid layers. In this thesis, we study not only the heterogeneous birth of a vapor nucleus on the solid-fluid interface at constant pressure by virtue of heat transfer through the solid and its achievement of stability, but also its subsequent growth, deformation and detachment. By considering the effects including that of the wettability of the solid

surface, we find the appropriate interaction parameters between the solid and fluid atoms, which are critical parameters for being able to observe nucleation and heat transfer. By artificially applying a uniform body force that, because of the nanoscale of the system, is orders of magnitude larger than terrestrial gravity, we have successfully nucleated and grown a vapor bubble to a moderate size. By then further increasing this artificial gravity, we find the body force indeed deforms the bubble and causes it to detach from the surface. We also are in the process of trying to accomplish these processes by resetting the temperature at the top of the simulation domain without changing the magnitude of the uniform body force. These simulations obtain time evolution of the contact line motion: the radius of contact line initially expands with growth of the bubble, then it contracts sharply but continuously with deform of bubble until its detachment and of temperature slip at the solid-fluid interface.

Current and future studies on this topic are generating contact line motions under a time-independent uniform body force, to determine if bubble leaves a vapor residue with three-phase contact line on the solid surface when it detaches, and what the fate of that bubble is as a function of system parameters, e.g., wall superheat. We will also use the resulting contact line motion with bubble growth as an input into our continuum model (without convection) to examine bubble deformation and detachment in that context. Clearly, convection will certainly play an important role in some circumstances. As such, a post-doc in our group (Dr. Lin Zheng) has begun using Lattice Boltzmann methods to address this problem, including the motion of the CL, and to quantitatively access the contribution of convective heat transfer. We suspect that such convection may tend to cause small vapor residues (if they appear) after bubble detachment to condense rather than to grow into a new bubble. This trend would oppose conduction through the solid towards the CL that would tend to cause the vapor residue to continue to grow, and we believe that this balance is critical in nucleate boiling. We hope that our work here and the planned work just described will contribute towards advancing the understanding of the mechanism of nucleate boiling heat transfer.

REFERENCES

1. Lienhard J, Witte LC. An historical review of the hydrodynamic theory of boiling. In: Amundson NR, Luss D, editors. Reviews in Chemical Engineering. Dordrecht: Freund Publishing House; 1985.
2. Lienhard J. A heat transfer handbook: Prentice-Hall; 1989.
3. Nukiyama S. The maximum values of the heat Q transmitted from metal to boiling water under atmospheric pressure. Trans. JSME 1934;37:357.
4. Gaertner RF. Photographic study of nucleate pool boiling on a horizontal surface. Transactions of the ASME Journal of heat Transfer 1965;87:17-29.
5. Das PK, Bhat GS, Arakeri VH. Investigations on the propagation of free surface boiling in a vertical superheated liquid column. Int. J. of Heat and Mass Transfer 1987;30:631-638.
6. VDI. Heat Atlas (English Edition). ingenieure VD, editor. Dusseldorf, Germany: VDI Verlag; 1993.
7. Moran KV, Oktag S, Puller L, Kerijilian G. Cooling concepts for IBM electronic packages. IEPS Proceedins 1982:120-140.
8. Marco PD, Grassi W. overview and prospects of boiling heat transfer studies in microgravity. International Symposium in space 97. Tokyo,Japan; 1997.
9. Rohsenow WM. A method of correlating heat-transfer data for surface boiling of liquids. Transactions of the ASME 1952:969-976.
10. Mikic BB, Rohsenow WM. A new correlation of pool-boiling including the effect of heating surface characteristics. Transactions of the ASME Journal of Heat Transfer 1969:245-250.
11. Stephan K, Abdelsalam M. Heat transfer correlations for natural convection boiling. Int. J. of Heat and Mass Transfer 1980;23:78-87.
12. Dhir VK. Mechanistic predictionof nucleate boiling heat transfer-Achievable or a hopeless task? J. Heat Transfer 2006;128:1-12.
13. Dhir VK. Phase change heat transfer – a perspective for the future. 2003.
14. Han CY, Griefith P. The Mechanism of Heat transfer in Nucleate Pool Boiling Int. J. Heat Mass Transfer 1965;8:887-914.
15. Dhir VK. Boiling heat transfer. Annual Reviews of Fluid Mechanics 1998;30:365-401.
16. Cooper MG, Lloyd AJP. Transient local heat flux in nucleate boiling. Proc. 3rd Intl. heat Trans. Conf. 1966;3:193-203.
17. Dhir VK, Qiu DM, Ramanujapu N, Hasan MM. Investigation of nucleate boiling mechanisms under microgravity conditions. 1996 Aug. 12-14, 1996; Cleveland, Ohio.
18. Moore FD, Mesler RB. The measurement of rapid surface temperature fluctuations during nucleate boiling of water. AIChE Journal 1961;7:620-624.
19. Cooper MG, Lloyd AJP. The microlayer in nucleate pool boiling. Int. J. Heat and Mass Transfer 1969;12:895-913.
20. Cooper MG. The microlayer and bubble growth in nucleate pool boiling. Int. J. Heat and Mass Transfer 1969;12:915-933.
21. Jawurek HH. Simultaneous determination of microlayer geometry and bubble growth in nucleate boiling. Int. J. of Heat and Mass Transfer 1969;12:843-848.

22. Koffman LD, Plesset MS. Experimental observations of the microlayer in vapor bubble growth on a heated solid. Transactions of the ASME Journal of Heat Transfer 1983;105:625-632.
23. Olander RR, Watts RG. An analytical expression of microlayer thickness in nucleate boiling. Transactions of the ASME Journal of heat Transfer 1969;91:178-180.
24. Wilson S, Davis S, Bankoff S. The unsteady expansion and contraction of a long two-dimensional vapour bubble between superheated or subcooled parallel plates. Journal of Fluid Mechanics 1999;391:1-27.
25. Landau L, Levich VG. Dragging of a liquid y a moving plate. Acta Physiochimica USSR 1942;17:42-54.
26. Bretherton FP. The motion of long bubbles in tubes. J. Fluid Mechanics 1961;10:166-188.
27. MITROVIC J. On the profile of the liquid wedge underneath a growing vapour bubble and the reversal of the wall heat flux. Int. J. Heat and Mass Transfer 2002;45:409-415.
28. MEI RW, Chen WC, Klausner JF. Vapor bubble growth in heterogeneous boiling I. Formulation. Int. Z Heat Mass Transfer. 1995;38(5):909-919.
29. Mei R, Chen WC, Klausner JF. Vapor bubble growth in heterogeneus boiling-2.growth rate and thermal fileds. Int. J. of Heat and Mass Transfer 1995;38:921-934.
30. Lee RC, Nydhal JE. Numerical calculation of bubble growth in nucleate boiling from inception through departure. Transactions of the ASME Journal of Heat Transfer 1989;111:474-479.
31. Plesset MS, Prosperetti A. The contribution of latent heat transport in subcooled nucleate boiling. Int. J. of Heat and Mass Transfer 1978;21:725-734.
32. Son G, Dhir VK, Ramanujapu N. Dynamics and heat transfer associated with a single bubble during nucleate boiling on a horizontal surface. J. Heat Transfer 1999;121:623-631.
33. Dhir VK. Numerical simulations of pool-boiling heat transfer. AIChE Journal 2001;47:813-834.
34. Scriven LE. On the dynamics of phase growth. Chemical Engineering Science 1959;10:1-13.
35. Juric D, Tryggvasson G. Numerical simulations of phase change in microgravity. 1996. p 33-44.
36. Juric D, Tryggvason G. Computations of boiling flows. Int. J. Multiphase Flow 1998;24:387-410.
37. Tryggvasson G, Jacqmin D. Computations of boiling in microgravity. 1996 Aug. 12-14, 1996; Cleveland, Ohio.
38. Son G, Dhir VK. Numerical simulation of saturated film boiling on a horizontal surface. Journal of Heat Transfer 1997;119:525-533.
39. Son G, Dhir VK. Numerical simulation of film boiling near critical pressures with a level set method. Journal of Heat Transfer 1998;120:183-192.
40. Kenning DBR. Wall temperature patterns in nucleate boiling. Int. J. Heat and Mass Transfer 1991;35:73-86.

41. Kenning DBR, Yan Y. Pool boiling heat transfer on a thin plate: features revealed by liquid crystal thermography. Int. J. Heat and Mass Transfer 1996;39:3118-3137.
42. Bae S, Kim M, Kim J. Improved technique to measure time-and space-resolved heat transfer under single bubbles during saturatd pool boiling of FC-72. Exper. Heat Transfer 1999;12:265-278.
43. Yaddanapuddi N, Kim J. Single bubble heat transfer in saturated pool boiling of FC-72. Multiphase Sci. Technol. 2001;12(3-4):47-63.
44. Demiray F, Kim J. Microscale heat transfer measurements during pool boiling of FC-72: effect of subcooling. International Journal of Heat and Mass Transfer 2004;47:3257-3268.
45. Delgoshaei P, Kim J. Microscale heat transfer measurements during subcooled pool boiling of pentane: effect of bubble dynamics. 2010 August 8-13,; Washington, DC, USA. p 1-9.
46. Sadhal SS. Heat transport to a slowly growing bubble on a solid surface. Q. J. Mech. Appl. Math. 1989;42:479-493.
47. Stephan P, Busse CA. Analysis of the heat transfer coefficent of grooved heat pipe evaporate walls. Int. J. Heat Mass Transfer 1992;35:383-391.
48. Stephan P, Hammer J. A new model for nucleate boiling heat transfer. Warme und Stoffubertragung 1994;30:119-125.
49. Nikolayev V, Beysens, DA, Lagier, G., Hegseth, J. Growth of a dry spot under a vapor bubble at high heat flux and high pressure. Int. J. Heat Mass Transfer 2001;44:3499-3511.
50. Nikolayev V, Beysens DA. 2D BEM modeling of a singular thermal diffusion free boundary problem with phase change. Boundary elements XXIV 2002:501-525.
51. Huang L. Heat transfer to a vapor bubble suspended near or attached to a solid plate. New York: City University of New York; 1996.
52. Koplik J, Banavar JR, Willemsen JF. Molecular dynamics of fluid flow at solid surfaces. Phys. Fluids A 1989;1:789.
53. Thompson PA, Robbins OM. Simulations of contact-line motion: Slip and the dynamic contact angle. Phys.Rev.Lett. 1989;63:766-769.
54. Jin W, Koplik J, Banavar JR. Wetting hysteresis at the molecular scale. Phys. Rev. Lett. 1997;78:1520.
55. Koplik J, Banavar JR. Molecular simulation of dewetting. Phys. Rev. Lett. 2000;84:4401.
56. Pan Y, Poulikakos D, Walther J, Yadigaroglu G. Molecular dynamics simulation of vaporization of an ultra-thin liquid argon layer on a surface. International Journal of Heat and Mass Transfer 2002.
57. Yang TH, Pan C. Molecular dynamics simulation of a thin water layer evaporation and evaporation coefficient. International Journal of Heat and Mass Transfer 2005;48:3516-3526.
58. Wemhoff AP,Carey VP. Molecular dynamics exploration of thin liquid films on solid surfaces. 1. Monatomic fluid films. Microscale Thermophysical Engineering 2005;9:331-349.

59. Wu YW, Pan C. Molecular dynamics simulation of thin film evaporation of Lennard-Jones liquid. Nanoscale and Microscale Thermophysical Engineering 2006;10:157-170.
60. Kimura T, Maruyama S. Molecular dynamics simulation of heterogeneous nucleation of a liquid droplet on a solid surface. Microscale Thermophysical Engineering 2002;6:3-13.
61. Maruyama S, TKaM-CL. Molecular Scale Aspects of Liquid Contact on a Solid Surface. Thermal Science & Engineering 2002;10(6):23-29.
62. Kandlikar SG,Maruyama S, Steinke ME, Kimura T. Moleular dynamics simulation and measurement of contact angle of water droplet on a platinum surface. 2001 November 11-16; New York. p 1-6.
63. Maruyama S, Kimura T. A molecular dynamics simulation of a bubble nucleation on solid surface. 1999 March 15-19; San Diego, California. p 1-7.
64. Bakr AA. The boundary integral equation method in axisymmetric street analysis problems. lecture notes in engineeirng. Brebbia CA, Orzag SA, editors: Springer Verlag; 1986.
65. Morse PM, Feshbach H. Methods of Theoretical Physics, Part I. New York McGraw-Hill; 1953. 666 p.
66. Jakob M. Heat Transfer. New York: Wiley; 1949.
67. Straub J, Zell M, Vogel B. Pool boiling in a reduced gravity field. 1990; Jerusalem, Israel. p 91-113.
68. Clark HB, Strenge PS, Westwater JW. Active sites for nucleate boiling. Chem.Engr.Prog.Symp. 1959;55(29):103-110.
69. Landau LD, Lifshitz EM. Standard nucleation theory. Stat. Phys. 1995:553.
70. Griffith P, Wallis JD. The role of surface conditions in nucleate boiling. Chem.Engr.Prog.Symp. 1960;56(30):49-63.
71. Joanny JF, Robbins MO. Motion of a contact line on a heterogeneous surface. The Journal of Chemical Physics 1990;92(5):3206-3212.
72. Pismen LM. Mesoscopic hydrodynamics of contact line motion. Colloids and Surface 2002;206:11-30.
73. Pomeau Y. Recent progress in the moving contact line problem:a review. C. R. Mecanique 2002;330:207-222.
74. Blake TD. The physics of moving wetting lines. Journal of Colloid and Interface Science 2006;299:1-13.
75. Stralen SJDV, Cole R, Sluyter WM, Sohal MS. Bubble growth rates in nucleate boiling of water at subatmospheric pressures,. Int. J. Heat Mass Transfer 1975;18:655-699.
76. Kowalewski TA, Pakleza J, Trzcinski R,Zachara A. Experimental analysis of vapour bubble growing on a heated surface. archives of thermodynamics 2004;25(3):1-12.
77. Gong SJ, Ma WM. An Experimental Study on Boiling Phenomenon in a liquid layer. 2010; Tampa,FL, USA.
78. Nonn TI. Measurement of bubble growth in a liquid in contact with a heated surface using phase-doppler anemometry. unpublished.
79. Roe RJ, Bacheta VL, Wong PMG. J. Phys. Chem. 1967;71:4190.

80. Padday JF. In: Matijevic E, editor. Surface and colloid science. Volume 1. New York: Wiley; 1969. p 101-149.
81. Shariff F. http://www.scribd.com/doc/3010266/Shape-of-a-Dew-Drop. 2008.
82. Wong H, Rumschitzki D, Maldarelli C. Theory and experiment on the low-Reynolds-number expansion and contraction of a bubble pinned at a submerged tube tip. J. Fluid Mechanics 1998;356:93-124.
83. Wong H, Rumschitzki D, Maldarelli C. Marangoni effects on the motion of an expanding or contracting bubble pinned at a submerged tube tip. J. Fluid Mechanics 1999;379:279-302.
84. Allen MP. Introduction to molecular yynamics simulation. Computational Soft Matter: From Synthetic Polymers to Proteins,Lecture Notes 2004.
85. Verlet. L. Computer experiments on classical fluids. i. thermodynamical properties of Lennard-Jones molecules. Phys. Rev. 1967;159(98-103).
86. Knuth. D. The art of computer programming.: Addison-Wesley, Reading MA,; 1973.
87. Frenkel D, Smit B. Understanding Molecular Simulation : From Algorithms to Applications Academic Press; 2001.
88. Gear CW. Numerical Initial Value Problems in Ordinary Differential Equations. Englewood Cliffs, NJ: Prentice-Hall; 1971.
89. Kinjo T, Matsumoto M. Cavitation processes and negative pressure. Fluid Phase Equilibria 1998;144:343-350.
90. Mecke M, Winkelmann J, Fischer J. Molecular dynamics simulation of the liquid–vapor interface:The Lennard-Jones fluid. J. Chem. Phys. 1997;107(21):9264-9270.
91. Koplik J, Pal S, Banavar JR. Dynamics of nanoscale droplets. Physical Review E 2002;65(021504):1-14.
92. Novak BR. Molecular simulation studies of heterogeneous bubble nucleation: effects of surface chemistry and topology: University of Notre Dame; 2007.
93. Bartell LS, Wu TD. A new procedure for analyzing the nucleation kinetics of freezing in computer simulation. J. Chem. Phys. 2006;125(194503).
94. Upcitll CE, Evans R. The surface tension and density profile of simple liquids. J. Phys. C: Solid State Phys. 1977;10:2791-2799.
95. Kim BH, Beskok A, Cagin T. Molecular dynamics simulations of thermal resistance at the liquid-solid interface. Journal of Chemical Physics 2008;129:174701.
96. Kapitza. PL. Zh. Eksp. Theor. Fiz. J. Phys. USSR 4 1941;11(1):181.
97. Khare R,Keblinski P, Yethiraj A. Molecular dynamics simulations of heat and momentum transfer at a solid–fluid interface: Relationship between thermal and velocity slip. International Journal of Heat and Mass Transfer 2006;49:3401-3407.